

ABSTRACT

VACHHANI, SHANTANU AVINASH. Computer Simulation and Analysis of Nanoparticle Delivery to the Olfactory Bulb for Direct Drug Migration to the Brain. (Under the direction of Dr. Clement Kleinstreuer).

Central Nervous System (CNS) disorders are one of the major causes of fatalities in the world today. The ground zero for all these disorders is the brain; thus, it is essential to transport a considerable concentration of drugs to the brain for any treatment to be effective. Invasive strategies have been used (eg, neurosurgery) to achieve life-saving treatment, but not without major risks. Hence, research into non-invasive strategies (nebulizers, inhalers, etc.) have gained momentum. The main pathway for transport these drugs into the brain requires crossing the Blood-Brain Barrier (BBB) located along the olfactory region of the nasal cavity. An important caveat to this pathway is that the tight junctions of the BBB allow only particles of nano-scale to pass through. Advancements in bio manufacturing have led to the development of multifunctional nanoparticles that can be used to target the brain via the olfactory bulb and then the BBB. The nasal cavity is a highly complex structure with various undulating pathways; hence, *in vivo* studies offer the most realistic picture of the air-particle dynamics inside the nasal cavities. However, human trials for drug delivery targeting the brain are scarce due to the delicate nature of the organs. Computational Fluid-Particle Dynamics (CF-PD) studies offer a manageable, accurate and cost-effective solution to the problem. OpenFOAM was employed to conduct all the fluid-particle dynamics simulations. OpenFOAM is an open-source CFD toolbox, used cost-free by researchers across the fields of engineering and sciences. To establish the credibility of the numerical simulation approach, the present computer models for nanoparticle transport and deposition have been validated. The main objective of this study is to establish a novel and practical methodology to optimize the nanodrug deposition efficiency inside the olfactory region, using a representative

human nasal cavity. The particle release map (PRM) approach was utilized to determine the best injection position for a cannula connected to a nebulizer. For 10nm nanodrugs leaving the cannula at 10m/s, 41% deposited in the olfactory region, while 20% deposited via targeting without the cannula, and <1% at normal breathing condition, i.e., 20lpm.

© Copyright 2019 by Shantanu Avinash Vachhani

All Rights Reserved

Computer Simulation and Analysis of Nanoparticle Delivery to the Olfactory Bulb for Direct
Drug Migration to the brain

by
Shantanu Avinash Vachhani

A thesis submitted to the Graduate Faculty of
North Carolina State University
in partial fulfillment of the
requirements for the degree of
Master of Science

Mechanical Engineering

Raleigh, North Carolina
2019

APPROVED BY:

Dr. Gregory Buckner

Dr. Pramod Subbareddy

Dr. Clement Kleinstreuer
Committee Chair

DEDICATION

To my parents, sister and friends for their unconditional support

BIOGRAPHY

Shantanu Vachhani was born on the 14th of May, 1995 to Mr. Avinash Vachhani and Mrs. Taruna Vachhani in Mumbai, India. After completing his high school education he attained his Bachelors of Engineering degree in the field of Mechanical engineering from Birla Institute of Technology and Science (BITS) Pilani, K.K Birla Goa Campus, Goa, India. Subsequently he moved to Raleigh, North Carolina in 2017 to pursue his graduate degree in Mechanical Engineering at North Carolina State University. He has been conducting research for his master's thesis under the guidance of Dr. Clement Kleinstreuer in the Computational Multi-Physics Lab at NC State and will receiving his master's degree in Fall 2019.

ACKNOWLEDGMENTS

First and foremost I would like to express my deepest gratitude to my academic advisor, Dr. Clement Kleinstreuer for giving me the opportunity to be a part of his research group. His constant guidance and support during this time has been invaluable to my research and has enabled me to grow professionally as a student. Throughout all the roadblocks he was very patient and offered valuable insight and suggestions that helped me overcome these hurdles. I would also like to thank Dr. Gregory Buckner and Dr. Pramod Subbareddy for taking time out of their busy schedules to be a part of my thesis committee. I would also like to thank all the members of the Computational Multi-Physics lab, Sriram, Adithya, Nilay, Sujal and Karthik for creating an environment that fosters discussion and innovation. The NCSU high performance computing services and support were extremely helpful in providing assistance in running my numerical simulations. My friends Chaitee, Shalini, Aamir , Utkarsh and Prasad have been a constant life support system and have made my time here in NCSU extremely enjoyable and comfortable. Last but not the least my family has been there for me during times of need and I would like this opportunity for their unconditional love.

TABLE OF CONTENTS

LIST OF TABLES	viii
LIST OF FIGURES	ix
CHAPTER 1. INTRODUCTION AND RESEARCH OBJECTIVES	1
1.1. Research Motivation	1
1.2. Literature Review.....	2
1.2.1. Introduction.....	2
1.2.2. Nasal Drug Delivery Devices	5
1.2.3. CFD studies.....	10
CHAPTER 2. MATH MODEL DEVELOPMENT AND COMPUTER SIMULATIONS	15
2.1. Introduction.....	15
2.2. Assumptions.....	15
2.3. Airflow Equations.....	16
2.4. Particle Dynamics Equations	19
2.4.1. Drag Force	21
2.4.2. Brownian Force.....	22
2.4.3. Saffman Lift Force.....	22
2.4.4. Gravitational Force	23
2.5. Quantifying Particle Deposition	23
2.6. Quasi-Steady vs Transient particle dynamics	24

CHAPTER 3. NUMERICAL METHOD USING OPENFOAM	26
3.1 Introduction.....	26
3.2. Case Structure	27
3.3. Case Set-up	34
3.4. Boundary Conditions	36
3.5. Numerical Schemes	39
3.6. Solution Control.....	41
CHAPTER 4. MODEL VALIDATIONS	42
4.1. Introduction.....	42
4.2. Geometry and Mesh of the Representative Nasal Cavities.....	43
4.3. Comparison with Calmet et al., 2018.....	48
4.3.1. Airflow Field Results.....	48
4.3.2. Particle Deposition Results.....	54
4.4. Comparison with Ingham (1975).....	57
4.4.1. Geometry and Mesh.....	57
4.4.2. Results and Discussions.....	58
4.5. Comparison with Tian et al., 2019.....	60
4.5.1. Airflow Field Results.....	62
4.5.2. Particle Deposition Results.....	66
CHAPTER 5. PARTICLE RELEASE MAP FOR OLFACTORY DRUG TARGETING	73

5.1 Introduction.....	73
5.2 Methodology.....	74
5.3. Results and Discussion	76
5.3.1. Micron-size Particles	76
5.3.2. Nanoparticles	85
CHAPTER 6. NASAL CANNULA FOR OLFACTORY DRUG TARGETING	95
6.1 Introduction.....	95
6.2. Results and Discussion	97
CHAPTER 7. CONCLUSION AND FUTURE WORK	102
REFERENCES	106

LIST OF TABLES

Table 2. 1. Boundary conditions for Particles.....	24
Table 3. 1 Boundary conditions for Velocity and Pressure.	36
Table 3. 2 Boundary conditions for Turbulent Kinetic Energy and Turbulence Dissipation	37
Table 3. 3. Numerical Schemes used in <code>simpleFoam</code>	40
Table 3. 4. Algebraic solvers used in <code>simpleFoam</code>	41
Table 4. 1. Geometry features of the Nasal Cavity.....	45
Table 4. 2. Unstructured mesh characteristics.	47
Table 4. 3. Comparison of particle deposition efficiencies.	54
Table 4. 4. Surface Area Comparison between G1 and G2	62
Table 5. 1. Legend correlating the color to the specific region.....	75
Table 6. 1. Olfactory deposition efficiencies for Cannula Injection (SOI = 10 m/s).....	101
Table 6. 2. Olfactory deposition efficiencies for Cannula injection (SOI = 3.5 m/s).....	101
Table 7. 1. Olfactory deposition comparison between the injection methods.....	103

LIST OF FIGURES

Figure 1. 1. Blood Brain Barrier (25).	5
Figure 1. 2. Anatomy of the Human Nasal Cavity (29).....	6
Figure 1. 3. Schematics of a nasal spray (32).	7
Figure 1. 4. Schematics of a nebulizer (34).	8
Figure 2 .1. Workflow of Euler- Lagrange simulations.....	20
Figure 3. 1. OpenFOAM case structure.	28
Figure 3. 2. U file for the elbow case.....	29
Figure 3. 3. boundary file in the polyMesh directory.	30
Figure 3. 4. transportProperties file in the constant directory.....	31
Figure 3. 5. controlDict file in the system directory.....	32
Figure 3. 6. fvSchemes file in the system directory.....	32
Figure 3. 7. Workflow for conducting OpenFOAM simulations.....	33
Figure 3. 8. transportProperties file.	34
Figure 3. 9. Snippet of the kinematicCloudProperties file.	35
Figure 4. 1. Geometry of the nasal cavity.....	43
Figure 4. 2. Complete view of the Nasal Cavity Geometry.....	44
Figure 4. 3. Isometric view of the unstructured mesh of the representative nasal cavity.....	46
Figure 4. 4. Mesh slice of the mid-section of the nasal cavity.....	47
Figure 4. 5. Mesh slice of the nostrils.....	48
Figure 4. 6. Slices 1-1' to 6-6' (left to right) of the nasal geometry.....	50
Figure 4. 7. Velocity contours (Slice 1-1' and 2-2').....	50
Figure 4. 8. Velocity contours (Slice 3-3' to Slice 6-6').	51

Figure 4. 9. Wall Shear Stress contour of the nasal cavity for 20 lpm.	51
Figure 4. 10. Turbulent kinetic energy contour of the nasal cavity for 20 lpm.	52
Figure 4. 11. Particle Deposition Pattern for 2, 10 and 20 μm particles.....	55
Figure 4. 12. Sectional Deposition for 20 μm particles.....	56
Figure 4. 13. Sectional Deposition for 10 μm particles.....	56
Figure 4. 14. Cylindrical geometry.....	57
Figure 4. 15. O grid meshing of the cylinder geometry.....	58
Figure 4. 16. Deposition efficiency comparison for a flowrate of 1pm.....	59
Figure 4. 17. Deposition efficiency comparison for a flowrate of 5pm.....	60
Figure 4. 18. Geometry G1.	61
Figure 4. 19. Geometry G2.	61
Figure 4. 20. Velocity contours along the nasal cavity for 5 lpm flowrate.....	63
Figure 4. 21. Velocity contours along the nasal cavity for 10 lpm flowrate.....	64
Figure 4. 22. Velocity streamlines across the nasal cavity.	65
Figure 4. 23. Velocity streamlines in the olfactory region.	65
Figure 4. 24. Recirculation regions in the nostrils.....	66
Figure 4. 25. Dean vortices in the nasopharynx.....	66
Figure 4. 26. Deposition pattern for 10 lpm flowrate and 1nm diameter particle.	67
Figure 4. 27. TDE comparison for 5 lpm and 7 lpm flowrates.....	68
Figure 4. 28. NOP Independent study for Total Deposition (10 lpm).....	69
Figure 4. 29. ODE comparison for 5 lpm and 7 lpm flowrates.	70
Figure 4. 30. NOP Independent study for Olfactory Deposition (10 lpm).	70
Figure 4. 31. Sectional Deposition of 1.1 nm,10 nm, 50 nm and 100 nm.....	71

Figure 5. 1. Nasal geometry with the specific regions that will be represented in the	75
Figure 5. 2.1. PRM for an impaction parameter of $333.333 \mu\text{m}^2\text{cm}^3\text{s} - 1$	78
Figure 5. 2.2. Deposition efficiency comparison between normal and targeted injection.....	78
Figure 5. 3.1. PRM for an impaction parameter of $1333.333 \mu\text{m}^2\text{cm}^3\text{s} - 1$	79
Figure 5. 3.2. Deposition efficiency comparison between normal and targeted injection.....	79
Figure 5. 4.1. PRM for an impaction parameter of $2083.333 \mu\text{m}^2\text{cm}^3\text{s} - 1$	80
Figure 5. 4.2. Deposition efficiency comparison between normal and targeted injection.....	80
Figure 5. 5.1. PRM for an impaction parameter of $8333.3333 \mu\text{m}^2\text{cm}^3\text{s} - 1$	81
Figure 5. 5.2. Deposition efficiency comparison between normal and targeted injection.....	81
Figure 5. 6.1. PRM for an impaction parameter of $33333.3333 \mu\text{m}^2\text{cm}^3\text{s} - 1$	82
Figure 5. 6.2. Deposition efficiency comparison between normal and targeted injection.....	82
Figure 5. 7. Deposition Pattern due to normal injection	83
Figure 5. 8. Deposition Pattern due to targeted injection	83
Figure 5. 9. Deposition Pattern due to targeted injection.	84
Figure 5. 10. Deposition Pattern due to targeted injection	85
Figure 5. 11.1. PRM of 1 nm particles for the flowrate of 5 lpm.	86
Figure 5. 11.2. Deposition efficiency comparison between normal and targeted injection.....	86
Figure 5. 12.1. PRM of 10 nm particles for the flowrate of 5 lpm.	87
Figure 5. 12.2. Deposition efficiency comparison between normal and targeted injection.....	87
Figure 5. 13.1. PRM of 100 nm particles for the flowrate of 5 lpm.	88
Figure 5. 13.2. Deposition efficiency comparison between normal and targeted injection.....	88
Figure 5. 14.1. PRM of 1 nm particles for the flowrate of 20 lpm.	90
Figure 5. 14.2. Deposition efficiency comparison between normal and targeted injection.....	90

Figure 5. 15.1. PRM of 10 nm particles for the flowrate of 20 lpm.	91
Figure 5. 15.2. Deposition efficiency comparison between normal and targeted injection.....	91
Figure 5. 16.1. PRM of 100 nm particles for the flowrate of 20 lpm.	92
Figure 5. 16.2. Deposition efficiency comparison between normal and targeted injection.....	92
Figure 5. 17. Deposition Pattern due to normal injection	93
Figure 5. 18. Deposition Pattern due to targeted injection	93
Figure 5. 19. Olfactory Deposition Efficiency trend due to targeted injection.....	94
Figure 5. 20. Nasal Deposition Efficiency trend due to targeted injection.	94
Figure 6. 1. Streamlines to the olfactory region.....	95
Figure 6. 2. Schematic of aerosol delivery using HFNC with a nebulizer..	96
Figure 6. 3. Position of the injection of particles from the cannula.....	96
Figure 6. 4.1. PRM of 2 μ m particles for the flowrate of 20 lpm	98
Figure 6. 4.2. Deposition pattern as a result of cannula injection.....	98
Figure 6. 5.1. PRM of 10 nm particles for the flowrate of 20 lpm	99
Figure 6. 5.2. Deposition pattern as a result of cannula injection.....	99
Figure 6. 6.1. PRM of 50 nm particles for the flowrate of 20 lpm	100
Figure 6. 6.2. Deposition pattern as a result of cannula injection.....	100

CHAPTER 1. INTRODUCTION AND RESEARCH OBJECTIVES

1.1. Research Motivation

Brain tumors as well as Central Nervous System (CNS) disorders (Alzheimer's, Parkinson's, Multiple Sclerosis etc.) are major causes of fatalities in the world today. Malignant brain tumors have a survival prognosis of less than 15 months (1) despite the progress that has been made. The most common brain cancer accounts for 80 % of all the malignant tumors (2). According to the Parkinson's Prevalence Project, nearly 1 million American's over the age of 45 will be diagnosed with Parkinson's by 2020 and this number is expected to increase to 1.24 million by 2030. Alzheimer's disease, according to the Alzheimer Association Report (2017), affects nearly 5.5 million people and is the 6th leading cause of death in the USA. These statistics clearly underline the gravity of the situation. Therefore treatment of these diseases has garnered a lot of attention, and considerable efforts have been put into the treatment of these ailments.

The ground zero for all these disorders is the brain; hence, it is essential to transport drugs to the brain for any treatment to be effective. The brain is an extremely fragile organ that is comprised of billions of nerve cells (neurons) that require regular supply of nutrients for proper functioning of the central nervous system. Due to the fragile nature of the brain, it is protected by the Blood Brain Barrier (BBB). This highly selective semipermeable membrane protects the brain from the circulating blood. The high selectivity is due to the presence of tight junctions between the adjacent endothelial cells that allow only very small compounds to pass through (3, 4). Furthermore, the cerebral endothelial cells show a considerably less pinocytotic activity than the systemic endothelium (5). Pinocytotic activity results in the transportation of substances across an epithelium by material-uptake on one face of a coated vesicle that can then be transported from the opposite face. Clearly, the reduction in the pinocytotic activity further limits the drug

transportation across the BBB. The blood cerebrospinal fluid barrier (BCSFB) forms the second layer that restricts the movement of drugs. This layer is located at the choroid plexus and separates the blood and the cerebrospinal fluid. However this layer is slightly more permeable than the BBB. The BBB surface area (120 sq ft) is roughly 5000 times the area of the BCSFB (6). Hence, BBB layer is the dominant obstacle for the delivery of drugs to the brain. These membranes are there to inhibit the passage of pathogens, antibodies, toxins etc. to the brain. In doing so they also restrict the transport of therapeutic drugs in to the brain. In summary, drug delivery to the brain is difficult to achieve at high enough efficiencies to counteract the toxins that are the root to the various CNS disorders (7).

1.2. Literature Review

1.2.1. Introduction

To overcome the limitations associated with brain drug targeting, different strategies have been or are in the process of being developed (4, 8, 9). These strategies can be broadly categorized into invasive and non-invasive strategies. Invasive strategies understandably are not preferred because of the complicated and delicate structure of the brain. Khan et al., 2017(8) described the various conventional invasive strategies that have been employed for brain drug targeting. One novel way to do this is using ultrasound waves to transiently open the BBB to facilitate drug migration to the brain. It involves exerting pressure on the BBB by using microbubbles that are injected in accordance with the acoustic energy principle. This results in the loosening of the junctions between the endothelial cells; thus, increasing the permeability of BBB towards the administered drugs. This methodology can increase the penetration of the BBB by as much as 340 % for glioblastoma treatment (10). A more direct way of drug targeting is intracerebral and intraventricular injection. This is done through the scalp where the drug is infused into the brain

parenchyma. In addition to being dangerous, this methodology is rendered largely ineffective due to the decreasing diffusive property inside the brain (11). With the progress in polymer technology, use of microchips and polymeric wafers (12, 13) has gained a lot of popularity in relation to brain drug targeting. These polymer wafers are based on polyanhydride and are placed in the tumor specific area from where controlled doses of the drug are released. Lin and Kleinberg, 2008(14) reviewed the pharmacokinetics of carmustine wafers as well as the efficacy of it in preclinical and clinical studies. The preclinical study compared the effect of drug delivery via the polymer wafer with systemic administered drugs in terms of the tumor growth delays. The former showed a 16.3 day delay as compared to a 9.3-11.2 day delay showing the potential of polymer wafers for treatment. A chemotherapeutic agent called temozolomide (TMZ) is utilized to treat gliosarcoma. Scott et al.,2011(15) conducted an *in vivo* rodent study that utilized a biocompatible microcapsule device to deliver TMZ to the tumor-infected area and showed the effectiveness of these devices. The microcapsule was implanted at day 0 and the median survival time was between 31-50 days, while for orally administered drugs it was 25 days. Microchips are another novel technology that has shown promising signs to achieve higher drug deposition efficiency in the olfactory region. Microchips can be microelectromechanical systems (MEMS), a device that provides programmable release of the drug at a specific target site (16). Drug is filled in a reservoir and the release of the drug is achieved by dissolving the reservoir cover through applying voltage between the anode and the cathode of the microchip. Since this a new technology and microfabrication of the device is expensive, not many *in vivo* studies have been conducted to implement this technology. According to one study (17) doses of 1,3-bis(2-chloroethyl)-1-nitrosourea (BCNU) (a brain cancer chemotherapeutic) through a microchip inserted into the brain were administered. The

BCNU chip showed comparable efficacy to the BCNU polymerized wafer and further research should pave way for an encouraging future of microchip technology.

As explained earlier, the Blood Brain Barrier (BBB) is a major obstacle for transporting the drugs into the brain stem. The BBB allows only an extremely selective set of particles to pass through it and hence it is essential to look into the physio-chemical characteristics of the drugs for an effective drug targeting system for brain tumors and other CNS disorders. There are two principle mechanisms by which molecules traverse through the barriers, ie, Active Transport and Passive Diffusion. The passive diffusion route involves drugs accumulating near the BBB and subsequently passing through it by means of diffusion. This route does not require any external energy input. Alternatively, certain transport proteins at the brain endothelial surface can help certain molecules bypass the BBB. This phenomenon is a form of active transport which can be further classified into carrier-mediated transport and receptor-based transport. It involves active efflux transporters (like P-glycoprotein (P-gp)) pumping out substrates in-between the brain and blood (18). The tight junctions of the BBB (Figure 1.1) restrict the molecular weight of bypassing molecules via passive diffusion and active transport to 500 Da and 600 Da, respectively (19). Clearly, the size of the drug plays a pivotal role in efficiency and effectiveness of drug delivery into the brain. Consequently Nanoparticles (particles with size ranging between 1-100nm) fit into the tight window that is required for passing through the BBB. Several studies (20-22) have shown that the lower the size of the particles, the higher is the deposition efficiency. Shape also plays a role in nanoparticle transport. Specifically nanorods have shown to have a higher adhesive property to the brain epithelium than the spherical nanoparticles (23, 24).

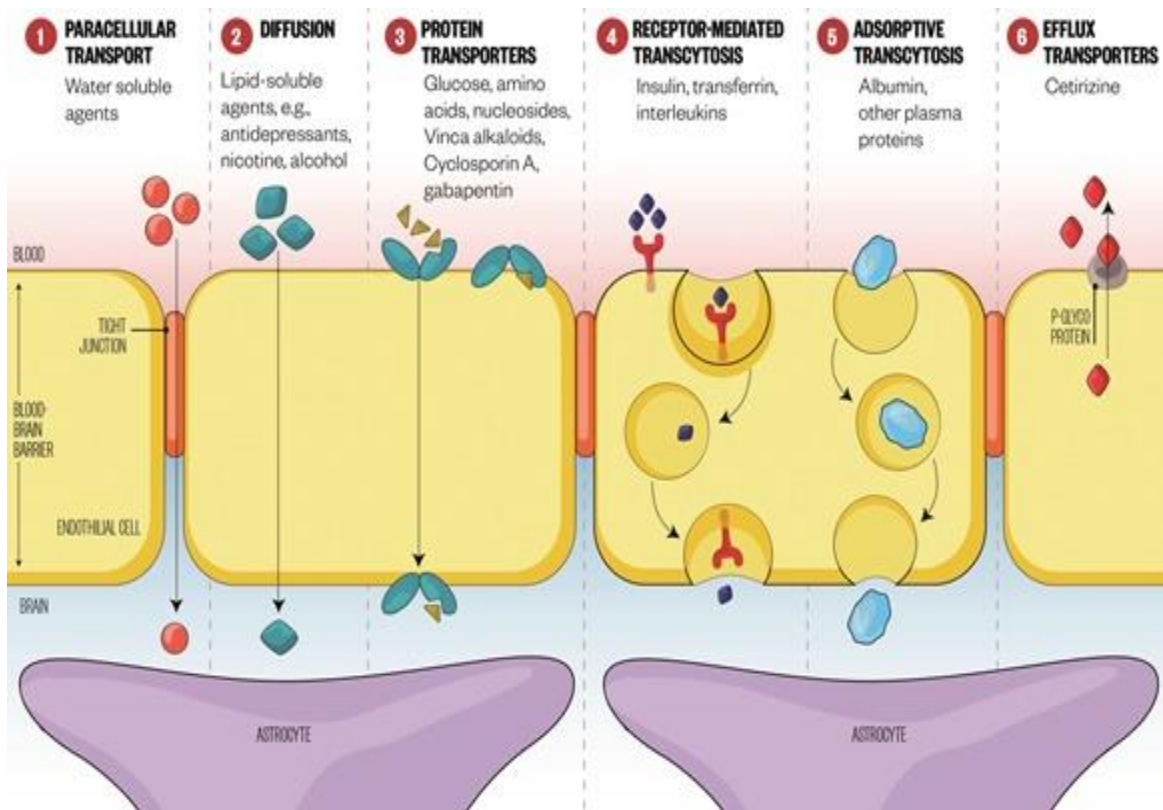


Figure 1. 1. Blood Brain Barrier (25).

1.2.2. Nasal Drug Delivery Devices

Drug delivery using the nasal route is a promising option and has been conventionally used in the form of nebulizers, nasal dry powder inhalers, spray pumps, nasal pressurized metered-dose inhalers, etc. Although the nose provides an accessible route to the olfactory region, there are certain challenge to nasal direct drug delivery (26-28).

Figure 1.2 shows the anatomy of the human nasal cavity. The nasal cavity is lined up with nasal mucosa which forms a part of the immune system. These barriers provide protection against any infectious and allergenic pathogens. The structure of the human nasal cavity starts with the nostril in the region known as the vestibule. This is followed by the respiratory section through which air travels, encountering contain bumps (also known as conchae or turbinate bones).

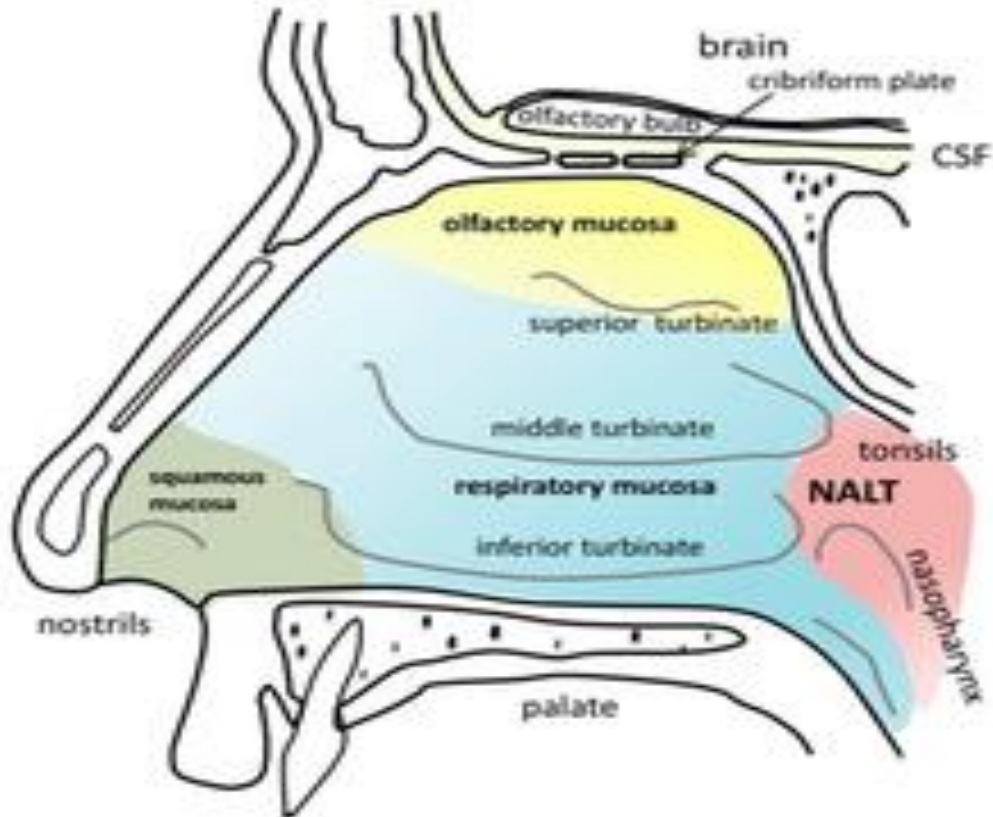


Figure 1. 2. Anatomy of the Human Nasal Cavity (29).

Underlying these bumps lie the meatuses which connect to the paranasal sinuses. Above the respiratory region lies the area of interest known as the olfactory region. The olfactory region contains the olfactory receptors that are responsible for the smelling sensation. It is evident that drug delivery and deposition onto a specific targeted site are not only dependent on the physiological characteristics of the nasal cavity but also on the nasal drug delivery system employed in conjunction with the physical characteristics of the therapeutics. The drug delivery devices rely on liquid and powder formulations with the liquid formulations being the most popular ones. Liquid formulations are largely preferred because the humidifying effect of these aqueous solutions seeks to oppose dryness and crusting (30). However, the disadvantage associated with droplets is that often preservatives like benzalkonium chloride, a skin irritant, (31) are required.

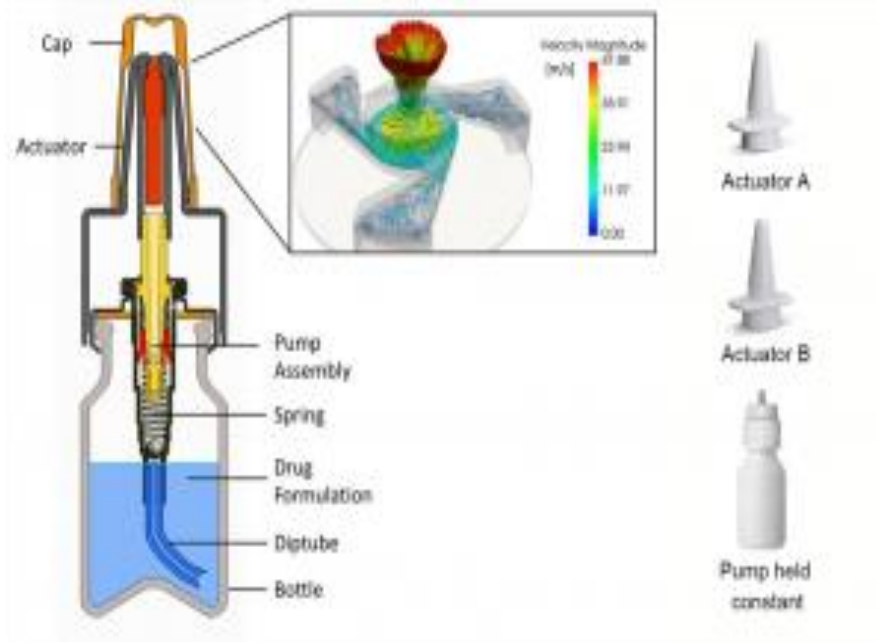


Figure 1. 3. Schematics of a nasal spray device (32).

Metered-dose spray pumps have dominated the nasal drug delivery market since their inception. Figure 1.3 shows the schematics of a standard nasal spray. Standard spray pumps are associated with dose volumes between 25 and 200 μl . The components of a metered-dose pump spray are a container, the pump with a valve and an actuator. The dose spray characteristics like particle size are dependent on the orifice of the actuator, pump properties and the force exerted. Another device used for delivering nasal drugs is a nasal pressurized metered-dose inhaler (pMDI). A compressed gas is suddenly expanded resulting in a high speed release of the drug particles. However these are also associated with something called the “cold Freon” effect, characterized by discomfort and dryness. Its name stems from the fact that conventionally the propellant used in these inhalers have been ozone depleting chlorofurocarbons (CFC). However, recently hydrofluroalkanes (HFA) have gained popularity as a propellant due to the negative environmental impact of the former. The HFA based inhalers produce a relatively slower particle velocity (15 m/s) than CFC based inhalers (52

m/s) (33) decreasing the irritation caused by the ‘cold Freon’ effect. Until now, these pMDIs have not been used for nose-to-brain applications. A recent study is focused on developing a nitrogen-based inhaler but further *in vitro* and *in vivo* studies are required for practical implementation.

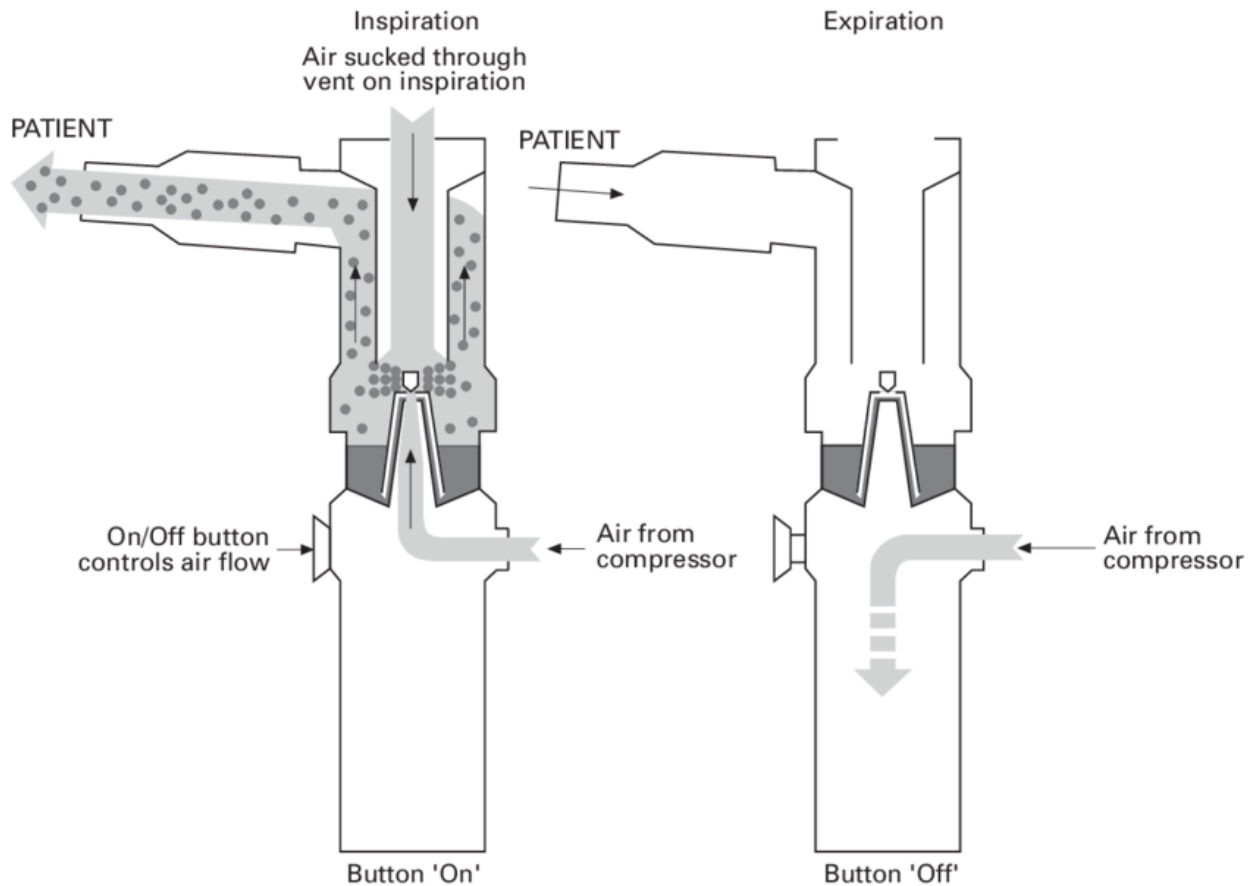


Figure 1. 4. Schematics of a nebulizer (34).

Compressed air nebulizers (35) are also popular for nasal drug delivery. Figure 1.4 shows the schematics of a nebulizer. These devices use either oxygen, compressed air, ultrasonic or mechanical power to break up medical formulations into small aerosol droplets at comparatively low speeds. The popular types of these devices in the market are jet nebulizers, ultrasonic and vibrating-mesh nebulizers - distinguished by the droplet creation mechanism (36). With nebulizers, droplets with diameters between 0.5 μm and 5 μm can be produced (37-41), well within

the respirable range. These nebulizers can also be used in conjunction with a high flow nasal cannula (HFNC). The HFNC efficiency has been analyzed (42, 43) for the purposes of ventilation and drug-delivery to lung sites. An *in vitro* study showed the maximum lung deposition efficiency of 32 % using this approach (44). The impact of gas flow and humidity using the nasal cannula in adults was studied by Alcoforado et al., 2019 (45). All the aforementioned studies have been concentrated on pulmonary drug delivery. Studies of direct nanodrug delivery to the olfactory bulb, using the cannula as an administering device, has not been published as the goal so far was to reach specific sites in the lung. For example, Longest et al., 2019 (46) reviewed the various nebulization technologies for delivering aerosols to the lungs and suggested secondary devices and technologies to increase the delivery efficiency of particles in the lungs. These claims are substantiated by the use of computational fluid dynamic simulations. Spence et al., 2019 (47) developed a new combination device with separate mesh nebulizers for generating humidity and delivering the medical aerosol. The device consists of a small volume mixing region where the aerosols are mixed with ventilation gas flow followed by a heating channel which produces small size droplets that are optimum for highly efficient nose-to-lung administration. Major utilization of these devices have been to target the sinuses and not the olfactory region. In addition to these liquid formulations, there are some powder formulations that are popular. These powder formulations are more stable than the liquid counterparts thereby eliminating the use of preservatives. These formulations are available in the market in three forms namely powder sprayers, powder inhalers and insufflators. Powder sprayers create a plume of spray particles due to the pressure created by the compressible compartment. Several studies (48-51) have been performed for testing the effectiveness of these devices in the market. On the other hand, nasal powder inhalers uses the subject's breath to inhale the particles. Insufflators unlike these two have a more complicated mechanism. It consists of a

mouthpiece and a connected nosepiece. The subject exhales in to the mouthpiece, closing the velum which enables the airflow to carry the particles into the nosepiece.

1.2.3. CFD studies

Previous studies on nasal deposition of inhaled nanoparticles include *in vivo* experiments in healthy volunteers (52, 53) and *in vitro* experiments in nasal replica casts based on cadavers or imaging of live subjects (53, 54). As explained earlier, the olfactory region serves as a promising path for nanodrugs to reach the brain via translocation along the nerve cells into the brain (55, 56). However, due to the complex structure of the nasal cavity, only a minuscule amount reaches the olfactory region naturally. *In vivo* studies offer the most realistic picture of the fluid-particle dynamics inside the nasal cavity; but, human trials are difficult to get approved owing to the delicacy of the targeted organ. Alternatively, Computational Fluid Dynamics (CFD) studies allow us to overcome this problem. CFD studies enable us to conduct “computer experiments” to predict nanoparticle trajectories and the effect of the airflow for realistic inhalation conditions. Once, a relatively high degree of confidence in the simulation accuracy is achieved and administering the drug is deemed safe and effective, *in vivo* studies in humans can be performed. Hence, it is essential to accurately model the interplay between airflow and particle dynamics. Historically micron particles have been studied for drug delivery due to the ability of nasal delivery devices (eg, nebulizers) to generate these micron-size droplets. Various CFD studies involved simulating the airflow and micron-size particle deposition inside a representative human nasal cavity model. Wang et al., 2009 (57) studied the influence of flowrate and the particle diameter on the deposition patterns for both micron and submicron sized particles. The results showed that micron deposition is dependent on the inertial parameter and Stokes number while deposition efficiency for nanoparticles is diffusion dominant. Reports from rat models are extrapolated to humans for *in*

vivo studies and then with CFD studies for particle deposition comparisons. Shang et al., 2015 (58) conducted such a study to establish a relationship between the depositions in rat and human nasal cavity. The results highlighted the anatomical differences between the geometries. As a consequence of this study, scaling factors were established for low, medium and high inertial particles. The aforementioned studies have considered only the nasal cavity as the computational domain. However, a more realistic picture of the flow and the deposition can be obtained by considering the breathing zone outside the nostril as well. Shang et al., 2015 (59) studied the effect of the breathing zone on the airflow patterns and consequently the particle deposition efficiencies. They found that the existence of the breathing zone creates additional small vortices in the nostrils and in the mid-section of the nasal cavities. This change in velocity contours significantly lowers the particle deposition efficiencies for particle sizes ranging from 7.8 -20 μm . The maximum decrease in particle deposition efficiency observed was 37.7 % for 12 μm particles. Hence the new nasal cavity model along with the breathing zone offers a better picture of the actual fluid-particle dynamics inside the nasal cavity. When it comes to nasal deposition patterns, subject variability is an important topic. Nasal geometries are different for different people and hence a study is required to establish a relationship between the particle deposition efficiencies and the geometrical parameters. Calmet et al., 2018 (60) used three different nasal geometries to study the effect of the different anatomical structures on deposition efficiencies. An interesting consequence of this study is that total deposition efficiency curves for all the subjects collapsed into a single function for a new Stokes-Reynolds number combination (*ie*, $Stk^{1.23} Re^{1.28}$). However, local deposition did not follow such a trend, as only one of the subject geometries observed particle deposition in the olfactory region.

One of the earliest CFD studies using a representative human nasal cavity model regarding nanoparticle deposition in the olfactory region was performed by Shi et al., 2006 (61). They treated airflow as laminar and incompressible while modeling nanoparticles as an Eulerian phase. Their simulations showed that for normal breathing rate and a nanoparticle diameter of 1 nm, the olfactory deposition efficiency is about 0.5 % while the total deposition efficiency is about 75 %. A similar study was conducted by Garcia and Kimbell, 2009 (62) using the CFD technique (63, 64) for a rat, considering nanoparticles with diameters ranging from 1 to 100 nm. They showed that the total deposition efficiencies decrease with increasing diameter. This was in agreement to previous studies (65-67) . Interestingly the highest olfactory deposition efficiency was approximately between 6-9 % for 3-4 nm particles. This can be attributed to the fact that the olfactory region occupies a greater percentage (about 5 times) of the area of the nasal cavity in case of rats as compared to humans. Tian et al. (2017) conducted a numerical study for a human nasal cavity (68) where the maximum olfactory deposition was 3.5% for nanoparticles of diameter of 1.5 nm. They also did a comparison between the deposition fractions between the rat and human nasal cavities (69). The study concluded that the major factors affecting the nasal and olfactory nanoparticle depositions are particle diffusivity and the breathing airflow rate. As a consequence they also developed certain correlations for olfactory and total nasal deposition efficiencies. Another outcome of the study was that the olfactory deposition of nanoparticles in both rats and humans is extremely low (< 3.5% and 8.1 %, respectively) due to the geometric and hence flow features of the nasal cavities. As an extension of their work on rats, Garcia et al., 2015 (70) compared the nanoparticle deposition inside the nasal cavities of humans for varying inhalation rates (15 to 30 L/min) and varying nanoparticle diameters (<100 nm). They concluded that the maximum olfactory deposition of the nanoparticles was around 1% for 1-2 nm particles.

The aforementioned studies involve steady-state simulations to have a qualitative and quantitative relationship between the particle dynamics and the fluid flow. However, for real life applications (inhalers, nebulizers, etc.) transient studies have to be done to accurately simulate the inhalation phenomena while using these devices. Particle deposition in transient studies are highly sensitive to the number of particles, injection timing and the position of the injection. Unlike the steady-state simulations, transient CFD simulations are considerably time consuming due to stability considerations. As mentioned earlier, one of the first transient studies conducted to compare the deposition patterns for steady and transient flow was by Shi et al., 2006 (61). Nanoparticles were treated as an Eulerian phase and the normal transient breathing profile was modeled using a modified sine-function, divided into an acceleration and a deceleration phase. The differences between particle transport in the accelerating and decelerating phase as well as the steady-state simulation are due to the “kinematic particle accumulation effect”. The decelerating phase generates a higher deposition efficiency while the accelerating phase results in the least. In addition to that a matching steady-state inhalation profile was determined that resulted in the same total deposition and to a certain degree the same sectional deposition that the transient breathing profile generated. Again, the maximum olfactory deposition efficiency observed was around 0.5 %. A similar study of micro-particles was done by Bahmanzadeh et al., 2016 (71). They observed that the steady flow analysis over-predicted the cyclic flow analysis by relative errors in the range of 10-60 %. It also concluded that although steady flow simulations are computationally more efficient, they do not accurately compare to transient simulations. Apart from the normal cyclic inspiratory flow, other breathing profiles have also been analyzed. Jiang et al., 2010 (72) simulated nanoparticle transport and deposition in a representative rat nasal cavity for restful breathing, moderate sniffing, and strong sniffing conditions. They noted that the total and olfactory deposition

during cyclic flows is lower than for steady flows. Furthermore the quasi – steady state assumption for transient flows is highly dependent on particle size, flowrate and breathing frequency. These factors can be combined to form the particle Strouhal number (Str_p). A similar sniffing study for micron-sized particles was performed by Calmet et al., 2018 (73). The sniffing profile was divided into three phases; namely acceleration, plateau and deceleration. The study provided a detailed regional deposition pattern from the nostril to third generation of the airways. An interesting result of this study is that olfactory deposition efficiency of 2.7% was observed for 10 μ m particle size. If correct, this is an important result for olfactory drug targeting.

CHAPTER 2. MATH MODEL DEVELOPMENT AND COMPUTER SIMULATIONS

2.1. Introduction

To conduct an accurate and realistic study of particle deposition in the olfactory region, it is essential to have the know-how of the underlying mathematical models to simulate the deposition mechanisms. This chapter provides the necessary equations and computer simulation approach in detail. The applicable conservation laws are difficult to implement, owing to the system's high degree of complexity. Hence, to conduct successful Computational Fluid-Particle Dynamics (CF-PD) simulations, certain assumptions have to be made which are listed in Section 2.2. After considering these assumptions, the resulting mathematical equations become simpler to solve. These equations are described in Section 2.3 along with the various particle transport forces which determine the trajectories of the particles. Chapter 3 then provides a brief introduction to the structure and working of OpenFOAM.

2.2. Assumptions

- The air inside the nasal cavity is taken to be an **incompressible** medium, indicating that there are no changes in the density of the air throughout the simulation. As the average human inhalation flow rate is between 15-20 lpm at approximately constant relative humidity, this is a reasonable assumption.
- All fluid dynamics processes are under **isothermal** conditions. Although there is always a certain temperature difference between the body and the incoming air, this study is only concerned with the interplay of the flow-particle characteristics.
- Two-phase particle fluid simulations are characterized by fluid-particle interactions (one-way coupling), vice-versa (two-way coupling) and particle-particle interactions (four-way

coupling). However because this study assumes that the fluid as a dilute suspension with volume fractions usually less than 10^{-3} , only **one –way coupling** is considered.

- For the purposes of this study, the monodisperse droplets (or solid particles) are spherical in shape. In this study, both nano- and micron- size particles are considered.
- Physiologically, the nasal cavity is lined with a mucus layer. The mucus layer is not stationary and incorporation of this behavior into the simulation could be done by solving another complex boundary condition equation. Consequently the particle transport and deposition changes. However this is a very basic study and the effect of mucus layer will be considered in future works.
- In the case of droplets in the air, due to the heat transfer inside the nasal cavity resulting in either evaporation or condensation, depending on the temperature difference. However since the study assumes isothermal conditions, these phenomena are not taken into account.

2.3. Airflow Equations

For simulating particle deposition in the human olfactory bulb, it is essential to model the fluid flow equations correctly. Since the values of the velocities in the fluid domain determine the forces and consequently the trajectories of the particles, any mistake in modelling these equations would result in inaccurate particle paths and deposition efficiencies. The airflow inside the nasal cavity is characterized by the Navier-Stokes Equations (Eq. 2.1 and Eq. 2.2). For model validation purposes, various (slow, medium and high) breathing rates are used. For medium to high breathing rates, the flow lies in the transitional regime, requiring to incorporate certain turbulence equations. Turbulence is modelled via Reynolds-Averaged Navier-Stokes (RANS) equations, and the Reynolds stresses via the Boussinesq hypothesis (1877) along with eddy viscosity models. Eddy viscosity is represented by the Shear Stress Transport k-omega (SST k- ω) model as it captures the

transitional regime with reasonable accuracy. Hence, unlike the laminar regime, the transitional regime is characterized by the flow transport equations in conjunction with the SST k- ω models.

The Navier Stokes Equations

Continuity

$$\nabla \cdot \mathbf{u} = 0 \quad (2.1)$$

Momentum

$$\begin{aligned} \frac{\partial}{\partial t}(u_x) + (\mathbf{u} \cdot \nabla)u_x &= -\frac{1}{\rho} \frac{\partial p}{\partial x} + \frac{\partial}{\partial x} \left[\nu \left(\frac{\partial u_x}{\partial x} + \frac{\partial u_x}{\partial y} + \frac{\partial u_x}{\partial z} \right) \right] + g_x \\ \frac{\partial}{\partial t}(u_y) + (\mathbf{u} \cdot \nabla)u_y &= -\frac{1}{\rho} \frac{\partial p}{\partial y} + \frac{\partial}{\partial y} \left[\nu \left(\frac{\partial u_y}{\partial x} + \frac{\partial u_y}{\partial y} + \frac{\partial u_y}{\partial z} \right) \right] + g_y \\ \frac{\partial}{\partial t}(u_z) + (\mathbf{u} \cdot \nabla)u_z &= -\frac{1}{\rho} \frac{\partial p}{\partial z} + \frac{\partial}{\partial z} \left[\nu \left(\frac{\partial u_z}{\partial x} + \frac{\partial u_z}{\partial y} + \frac{\partial u_z}{\partial z} \right) \right] + g_z \end{aligned} \quad (2.2)$$

\mathbf{u} denotes the velocity vector with u_x , u_y and u_z as components of velocity along the x, y and z directions. The pressure is denoted by p . The density and kinematic viscosity of the carrier fluid are given by ρ and ν , respectively. The gravity force is represented as $g_x \hat{\mathbf{i}} + g_y \hat{\mathbf{j}} + g_z \hat{\mathbf{k}}$.

As mentioned earlier, for transitional regime is modelled via the RANS equations which are given below.

$$\frac{\partial \bar{u}_i}{\partial x_i} = 0 \quad (2.3)$$

$$\frac{\partial(\rho \bar{u}_j)}{\partial t} + \bar{u}_i \frac{\partial}{\partial x_i} (\rho \bar{u}_j) = -\frac{\partial p}{\partial x_j} + \mu \frac{\partial}{\partial x_i} \left(\frac{\partial \bar{u}_j}{\partial x_i} - \overline{\mathbf{u}'_j \mathbf{u}'_i} \right) \quad (2.4)$$

The velocity vector is represented by u_j , where 'j' denotes the index. When the velocities in the 3-D Navier Stokes equations are split into its two components, namely the average component and

the fluctuating component (Eq. 2.5), it results in the formation of the RANS equations.

$$\mathbf{u}_j = \overline{\mathbf{u}}_j + \mathbf{u}'_j \quad (2.5)$$

Where,

$\overline{\mathbf{u}}_j$ = Average component of the velocity.

\mathbf{u}'_j = Fluctuating component of the velocity.

When dealing with the RANS equations, it is extremely difficult to quantify the fluctuating component of the velocities because of their nature of randomness. Hence the shear transport term ($\overline{\mathbf{u}'_j \mathbf{u}'_i}$) is modelled as shown in eq. This model formulation is based on the Boussinesq hypothesis (1877).

$$\overline{\mathbf{u}'_j \mathbf{u}'_i} = \nu_T \left(\frac{\partial \overline{\mathbf{u}}_j}{\partial x_i} + \frac{\partial \overline{\mathbf{u}}_i}{\partial x_j} \right) \quad (2.6)$$

As a result of the aforementioned modelling, RANS equations are no longer dependant on the fluctuating component of the velocity and hence solving the RANS equations is easier. To turn the RANS equations into a closed system of non-linear differential equations and make them solvable, it is necessary to obtain math models for ν_T (known as the eddy or turbulent viscosity). In the current study, a SST-k- ω turbulence model is used to solve for the turbulent viscosity. This model approximates the turbulent viscosity as a function of the ratio of turbulent kinetic energy (k) and specific dissipation rate ω . This model is briefly explained below.

$$\frac{\partial(\rho k)}{\partial t} + \frac{\partial}{\partial x_j} (\rho u_j k) = \widetilde{P}_k - \widetilde{D}_k + \frac{\partial}{\partial x_j} \left(\left(\mu + \frac{\mu_t}{\sigma_k} \right) \frac{\partial k}{\partial x_j} \right) \quad (2.7)$$

where \widetilde{P}_k and \widetilde{D}_k are the terms for production and destruction of turbulence kinetic energy, respectively; μ_t is the turbulent viscosity and σ_k is the turbulent Prandtl number for k.

$$\frac{\partial(\rho \omega)}{\partial t} + \frac{\partial}{\partial x_j} (\rho u_j \omega) = \alpha \frac{P_k}{\nu_t} - D_\omega + c d_\omega + \frac{\partial}{\partial x_j} \left(\left(\mu + \frac{\mu_t}{\sigma_\omega} \right) \frac{\partial \omega}{\partial x_j} \right) \quad (2.8)$$

where ω is specific dissipation rate, ν_t is the turbulent eddy viscosity, and cd_ω is the cross diffusion term.

$$\frac{\partial(\rho\gamma)}{\partial t} + \frac{\partial}{\partial x_j}(\rho u_j \gamma) = P_{\gamma 1} - E_{\gamma 1} + P_{\gamma 2} - E_{\gamma 2} + \frac{\partial}{\partial x_j} \left(\left(\mu + \frac{\mu_t}{\sigma_\gamma} \right) \frac{\partial \gamma}{\partial x_j} \right) \quad (2.9)$$

where $P_{\gamma 1}$ and $E_{\gamma 1}$ are transition source terms, $P_{\gamma 2}$ and $E_{\gamma 2}$ are destruction source terms and γ is the intermittency coefficient. But since for calculating $P_{\gamma 1}$ we require critical Reynolds number $\tilde{Re}_{\theta c}$, a transported scalar $\tilde{Re}_{\theta t}$ is used in the transport equation to calculate $\tilde{Re}_{\theta c}$

$$\frac{\partial(\rho \tilde{Re}_{\theta t})}{\partial t} + \frac{\partial}{\partial x_j}(\rho u_j \tilde{Re}_{\theta t}) = P_{\theta t} + \frac{\partial}{\partial x_j} \left(\sigma_{\theta t} (\mu + \mu_t) \frac{\partial \tilde{Re}_{\theta t}}{\partial x_j} \right) \quad (2.10)$$

2.4. Particle Dynamics Equations

An Euler-Lagrange approach was used to solve for the fluid-particle dynamics. Euler (in this case being the carrier fluid) refers to the fluid phase, being treated as a continuum, while the Lagrangian phase is being treated as a discrete phase (the drug particles). The Lagrangian phase is tracked individually along the particle path, where the particles are grouped together to form an “element” with the aggregation of such similar elements creating a control volume. The finite volume methodology utilizes the control volume approach to solve for the scalar, vector and tensor fields associated with the carrier fluid. The particle transport equation for particles under consideration (micron and nano-sized particles) takes the form of Newton’s second law of motion. The workflow of equations solved in the Euler-Lagrangian approach in a particular time step is shown in Figure 2.1. The trajectories of the particles are calculated by time-marching the Ordinary Partial Differential Equations (ODEs) represented by Eq. (2.11).

$$m_p \frac{\partial(\mathbf{v}_p)}{\partial t} = \sum \mathbf{F}_p \quad (2.11)$$

Here the \mathbf{v}_p and m_p denote the velocity and the mass of the particle, respectively; while $\sum \mathbf{F}_p$

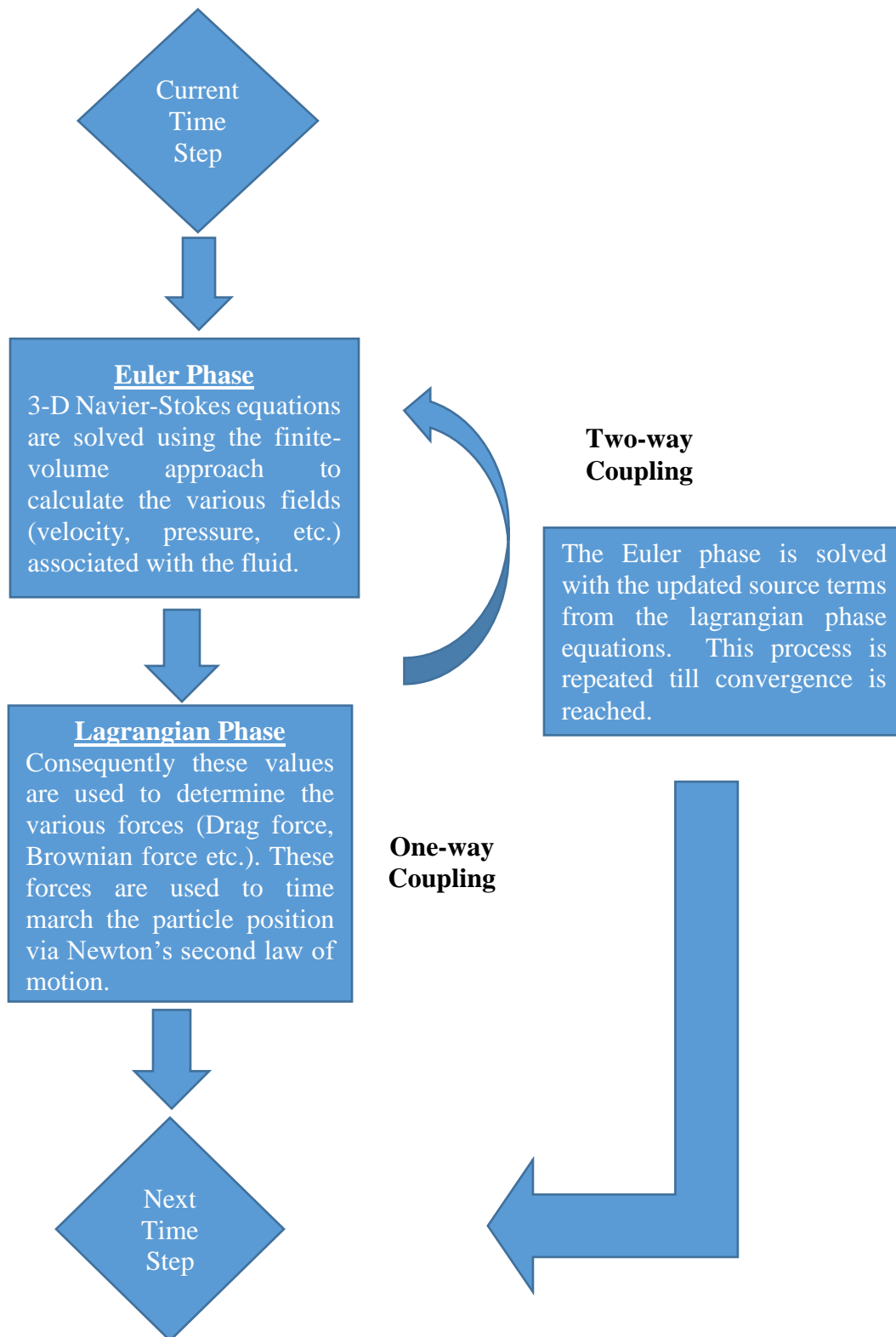


Figure 2. 1. Workflow of Euler-Lagrange simulations.

represents the summation of the various forces acting on the particle. The forces acting on the particle are greatly dependant on the size of the particles. For example, gravity and drag forces dominate the dynamics of micron particles while Brownian and lift forces play a major role in determining the trajectories of nanoparticles.

2.4.1. Drag Force

An important consideration for larger particles (micron size and above) is the drag force. The drag force is exerted on the particle due to its relative motion with respect to the fluid flow. It is dependent on the size and shape of the particle as well as the characteristics of the flow field. It is given by the following expression:

$$F_D = \frac{1}{2} \rho v_{rel}^2 C_D A_p \quad (2.12)$$

Where ρ is the density of the fluid, v_{rel} is the relative velocity of the particle that is given by $v - v_p$ with the subscript p denoting the velocity of the particle. C_D is the drag coefficient that depends on the particle Reynolds number (Eq.2.14) along the with Reynolds number of the carrier phase (74). A_p is the projected area of the particle which is given by Eq. (2.15).

$$C_D = \frac{24}{Re k_1} (1 + 0.1118(Re k_1 k_2)^{0.6567}) + 0.4305 \frac{k_2}{(1 + \frac{3305}{Re k_1 k_2})}$$

$$k_1 = \frac{3}{1 + 2\psi^{-0.5}}$$

$$k_2 = 10^{1.84148(-\log_{10}^{(\psi)})^{0.5745}} \quad (2.13)$$

$$\psi \text{ (sphericity)} = 1 \text{ (for a sphere)}$$

$$Re_p = \frac{\rho_p v_{rel} d_p}{\mu} \quad (2.14)$$

$$A_p = \frac{\pi}{4} d_p^2 \quad (2.15)$$

2.4.2. Brownian Force

For particles in the nano-scale domain, corresponding to the ultra-fine suspensions in this study, the momentum is imparted to the particles by the fluid at random; unlike micron particles where inertia is the major driving force. As a result, the particles move in a random path. As the size of the nanoparticles increases, the influence of the Brownian force decreases. The Brownian force is given by the following equation.

$$F_B = \zeta \sqrt{\frac{\pi S_0}{\Delta t}} \quad (2.16)$$

where ζ is a zero-mean, unit-variance Gaussian random number, Δt is the time-step size of particle integration and S_0 is the spectral intensity function defined as

$$S_0 = \frac{216 \mu k_b T}{\pi^2 d_p^5 \rho_p^2 C_c} \quad (2.17)$$

$$k_b = \frac{R}{N_a} = \frac{8.315 \times 10^3 \frac{J}{kmol \cdot K}}{6.022 \times 10^{26} \frac{molecule}{kmol}} = 1.38 \times 10^{-23} \frac{J}{molecule \cdot K} \quad (2.18)$$

here μ and T is the dynamic viscosity and Temperature of the carrier phase respectively. μ_p and d_p denote the dynamic viscosity and diameter of the particle respectively. k_b (Eq. 2.18) is the Boltzmann constant and C_c is the Cunningham correction factor given by

$$C_c = 1 + \frac{2\lambda}{d_p} \left(1.17 + 0.525 e^{-\left(\frac{0.78 d_p}{2\lambda}\right)} \right) \quad (2.19)$$

λ is the mean-free path of the carrier phase.

2.4.3. Saffman Lift Force

Small particles in a shear field experience a lift force perpendicular to the direction of flow. It is as a result of inertia effects in a viscous flow.

$$F_L = \frac{\pi}{6} d_p^3 \rho C_L ((\vec{v} - \vec{v}_p) \times \text{curl}(\vec{v})) \quad (2.20)$$

where

$$C_L = \frac{3 C_{ld}}{2\pi \sqrt{\frac{\rho |\text{curl}(\vec{v})| d_p^2}{\mu}}} \quad (2.21)$$

$$C_{ld} = 6.46 * 0.0524 \sqrt{0.5 \frac{\rho |\text{curl}(\vec{v})| d_p^2}{\mu}} \quad (2.22)$$

2.4.4. Gravitational Force

Gravitational force is experienced due to the earth's gravitational force. However for convenience Buoyancy forces are grouped with the gravitational forces. Buoyancy force is the upward exerted on the particle submerged in the fluid. These forces directly impact particle deposition due to sedimentation and hence for bigger particles it is essential to take these forces into account. It is given by Eq.2.23. The subscripts p and f represent the particle and carrier phase (fluid) respectively.

$$F_g = m_p g \left(1 - \frac{\rho_f}{\rho_p}\right) \quad (2.23)$$

2.5. Quantifying Particle Deposition

For accurately determining the deposition efficiencies, it is essential to specify the various boundary conditions for the particles. OpenFOAM has three basic options, namely REBOUND, STICK and ESCAPE.

- The particle is said to STICK when it is at the particle-radius distance from the wall.
- REBOUND boundary condition makes the particle rebound from the particular patch (Coefficient of Restitution = 1).
- The ESCAPE boundary condition allows the particle to pass through the particular patch and escape the geometry without sticking or rebounding.

Table 2. 1. Boundary conditions for Particles.

PART	BOUNDARY CONDITIONS
NASALINLET	REBOUND
NASAL	STICK
OUT	ESCAPE

For an Euler-Lagrange approach, Deposition Fraction (DF) is a parameter used to quantify the percentage of deposition.

$$DF_{\text{region}} = \frac{\text{Number of particles deposited in a specific region}}{\text{Number of particles entering the region}} \quad (2.24)$$

2.6. Quasi-Steady vs Transient particle dynamics

As mentioned above, drug deposition is the parameter used to measure the efficacy of drug delivery. As far as practical application is considered, drug delivery is a transient phenomenon. The various transient studies have been explained in Chapter 1. Drug deposition in transient studies is highly sensitive to various parameters like time of injection, duration of injection, etc. However while conducting studies that determine the effect of flowrate and particle injection, it is essential to isolate only these parameters. Furthermore transient studies are more computationally expensive and time consuming than quasi- steady state studies. Hence before conducting a transient simulation that mimics the workings of an actual drug delivery system like an inhaler or a nasal spray, particle deposition in a quasi-steady state flow is measured to determine the optimum particle diameter and flowrate as well as the desired position of injection for maximum olfactory deposition efficiency. In this study, all the simulations performed are under the assumption of quasi-steady state conditions. According to the approach reported in previous studies (61, 75) , a

steady state inhalation value that results in the same deposition as that of a transient case is calculated using the following formula :-

$$Q_{match} = C (Q_{mean} + Q_{max}) \quad (2.22)$$

Where $C \approx 0.5$ for all smooth inhalation forms. This result is an important one because it forms a bridge between the steady and transient inhalation results. It furthermore shows that the steady and transient results are similar in their qualitative distribution while differing in quantitative deposition results. Hence the optimal particle injection position resulting from a quasi-steady state flow assumption would also result in the highest olfactory deposition efficiency when using transient flow with only the exact value being different.

CHAPTER 3. NUMERICAL METHOD USING OPENFOAM

3.1 Introduction

For the purpose of this study, an open source Computational Fluid Dynamics toolbox named OpenFOAM (Open Field Operation and Manipulation) has been used (<https://www.openfoam.com>). In addition to being cost-free, this toolbox has far-reaching applications in engineering and scientific circles. Professionals from industry as well as academia utilize this toolbox to perform all facets of thorough Computational Fluid Dynamics activities, ranging from meshing (`blockMesh` and `snappyHexMesh`) to numerically solving 3-D complex flow systems (electromagnetics, turbulence, heat transfer, chemical reactions, multiphase flow, etc.). Owing to its open source nature, it facilitates the sharing of information and high level mathematical models for the purposes of a collaborative study. OpenFOAM is also highly compatible with various post-processing software (eg, ICEM, ParaView and Tecplot) and therefore results can be analysed without any inconvenience. OpenFOAM is built on the principle of Object Oriented Programming as it is written in C++. Therefore, all the models and computational solvers are built based on classes and objects. Furthermore, all the advantageous features of C++ (inheritance, encapsulation, data abstraction, etc.) are carried over into OpenFOAM, thereby making it quite user-friendly. The code structure is easy to grasp and enables the user to not only customize and extend the functionality of existing solvers but also to develop new ones with great ease. When dealing with numerical computations, running time is an important factor to be taken into consideration as certain computations may require months. Running these simulations in “parallel” has been shown to have reduced running (or computing) time considerably. In this method, the case geometry is decomposed into a number of sections and each processor is responsible for the computation involving a particular section. In other words,

multiple processors are simultaneously carrying out computations and exchanging data as opposed to only one processor solving necessary governing mathematical equations for the whole case geometry. OpenFOAM has built-in provisions for decomposition of cases, running them in parallel as well as reconstructing the decomposed fields for data analysing and post processing. It is essential to gain understanding of the unique case structure of OpenFOAM to make use of its full functionality. This structure is explained in the following section.

3.2. Case Structure

As mentioned earlier, OpenFOAM is a multi-purpose open source toolbox for carrying out computational studies (especially Computational Fluid Dynamics). It has various in built-in solvers with a sample case study associated with the solver. Each case directory in OpenFOAM has three main subdirectories: time directories, constant, and system. The content of these subdirectories varies from solver to solver. For example, the simplest solver in OpenFOAM is `icoFoam` which solves the Navier-Stokes equations for an incompressible, isothermal system.

This case contains three subdirectories: `0`, `constant` and `system` (Figure 3.1). The `0` folder is a time directory that holds the solution (in this case `u` and `p` for velocity and pressure, respectively) during the start of the simulation. Basically the `0` folder is used to specify the initial and the boundary conditions. These conditions can be very basic, such as a fixed value, to complicated ones like specifying a time-varying sinusoidal wave at the boundary via `swak4Foam` (Swiss Army Knife for FOAM). Like the `0` directory, there can be other time directories that stores the values of the fields (`p`, `T`, `u` etc.) at those respective time values. These time directories are used to post-process the simulation results in ParaView. The contents of these time subdirectories differ from solver to solver. For cases that deal with heat transfer, the time directories will have `T` (Temperature) as a field while for turbulence solvers, `k` and `epsilon` may be present as fields.

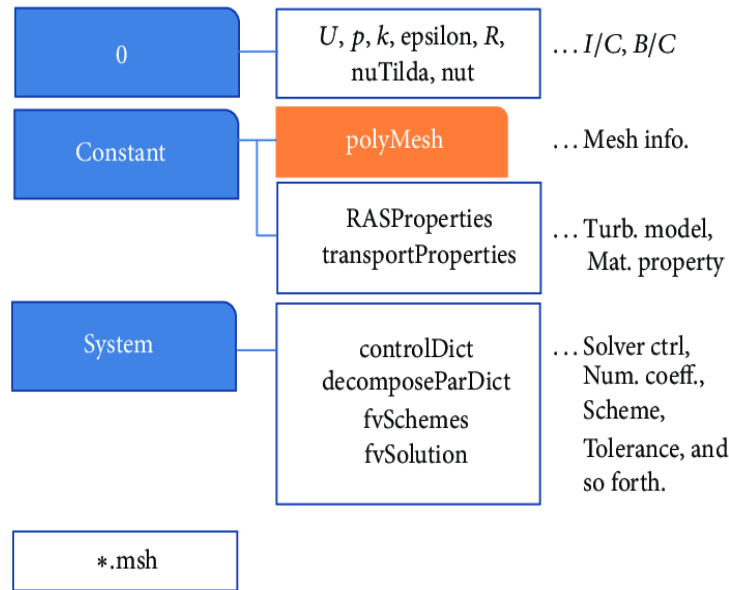


Figure 3. 1. OpenFOAM case structure.

For example, the tutorial case in `icoFoam` is simulating flow inside an elbow. The `0` folder of the elbow case requires the boundary conditions for pressure (p) and velocity (U). Figure 3.2 shows the `U` file for the elbow case. The file consists of the `dimensions` of the field, the `internalField` which has the information of the initial conditions of the velocity and the `boundaryField` through which the boundary conditions are specified. In this case, the velocity magnitude is 0 throughout the internal mesh. Through OpenFOAM this field can be either `uniform` or `nonuniform`; `wall-4`, `velocity-inlet-5` and `pressure-outlet-7` are the names of the patches of the elbow geometry. Here, `noSlip` and `fixedValue` are examples of the Dirichlet boundary condition, while `zeroGradient` is a type of Neumann boundary condition. The `constant` subdirectory has a `polyMesh` folder that contains the details of the mesh, ie, the number of points, boundary faces, neighbouring elements, etc. The directory `constant`, as the name suggests, also has the values of those properties that are not varying with time (eg, density, kinematic viscosity, etc.).

Figure 3.3 shows the `boundary` file in the `polyMesh` directory for the elbow case. It contains

```

/*----- C++ -----*/
| ===== |
| \\ / F i e l d | OpenFOAM: The Open Source CFD Toolbox |
| \\ / O p e r a t i o n | Version: dev |
| \\ / A n d | Web: www.OpenFOAM.org |
| \\ / M a n i p u l a t i o n |
/*-----*/

FoamFile
{
    version      2.0;
    format       ascii;
    class        volVectorField;
    object       U;
}
// ***** //

dimensions      [0 1 -1 0 0 0 0];

internalField   uniform (0 0 0);

boundaryField
{
    wall-4
    {
        type      noSlip;
    }
    velocity-inlet-5
    {
        type      fixedValue;
        value      uniform (1 0 0);
    }
    pressure-outlet-7
    {
        type      zeroGradient;
    }
}
// ***** //

```

Figure 3. 2. U file for the elbow case.

the name of the various patches of the geometry along with the properties of the respective patches. The properties include the `type` of the part of the geometry, `nFaces` which gives the number of surface faces associated with that patch, and `startFace` which represents the number of the starting face cell of that patch. Apart from the `boundary` file, the `polymesh` directory contains other files namely `cellZones`, `faces`, `faceZones`, `neighbour`, `owner`, `points` and `pointZones`. For the purposes of solving the Incompressible Navier-Stokes equations (like the elbow case), the only fluid property required is the Kinematic viscosity. Figure 3.4 shows the `transportProperties` file in the constant dictionary for the elbow case. `nu` represents the kinematic viscosity followed by the dimensions ($\text{Length}^2\text{Time}^{-1}$) and the value.

```

/*----- C++ -----*/
|=====|
| \\ / F i e l d | OpenFOAM: The Open Source CFD Toolbox |
| \\ / O p e r a t i o n | Version: dev |
| \\ / A n d | Web: www.OpenFOAM.org |
| \\ / M a n i p u l a t i o n | |
|-----|
|* OpenFOAM for Windows 18.10 (v1) |
|* Built by CFD Support, www.cfdsupport.com (based on Symscape). |
|-----|
FoamFile
{
    version      2.0;
    format       ascii;
    class        polyBoundaryMesh;
    location     "constant/polyMesh";
    object       boundary;
}
// ***** //

6
(
    wall-4
    {
        type            wall;
        inGroups        1(wall);
        nFaces          100;
        startFace       1300;
    }
    velocity-inlet-5
    {
        type            patch;
        nFaces          8;
        startFace       1400;
    }
    pressure-outlet-7
    {
        type            patch;
        nFaces          8;
        startFace       1412;
    }
}
// ***** //

```

Figure 3. 3. boundary file in the polyMesh directory.

While `icoFoam` is a simple solver, other complex solvers require properties other than the kinematic viscosity. For `nonNewtonianIcoFoam`, the specific Non Newtonian Model (Quemada, Carreau, etc.) along with the value of specific coefficients while for conducting Computational Fluid-Particle Dynamics (CF-PD) simulations various parcel properties like parcel injection rate, number of parcels and parcel diameter are to be specified in the constant directory. The system directory is comprised of three basic files namely `controlDict`, `fvSchemes` and `fvSolutions`. The `controlDict` file is responsible for the Solution Time control of the simulation. The user specifies the start time, end time, write Interval and time step of the simulation amongst other parameters in this file (Fig. 3.5).

```

/*-----*- C++ -*-----*/
| ===== |
| \ \ / F i e l d | OpenFOAM: The Open Source CFD Toolbox | | | |
| \ \ / O p e r a t i o n | Version: dev |
| \ \ / A n d | Web: www.OpenFOAM.org |
| \ \ / M a n i p u l a t i o n | |
| | | | | |
/*-----*- C++ -*-----*/
FoamFile
{
    version      2.0;
    format       ascii;
    class        dictionary;
    location     "constant";
    object       transportProperties;
}
// ***** //

nu              [0 2 -1 0 0 0 0] 0.01;

// ***** //

```

Figure 3. 4. transportProperties file in the constant directory.

CFD involves discretizing non-linear mathematical equations into algebraic equations that are subsequently solved by certain matrix equation solvers. The process of discretization requires a lot of accuracy and stability considerations and the fvSchemes file (Figure 3.6) allows you to choose a finite volume discretization scheme from an extensive list of available options that is most suitable for your particular study. Gradient, Divergence and Laplacian Schemes can be individually changed as per the requirement of the problem. Gradient, Divergence and Laplacian Schemes can be individually changed as per the requirement of the problem.

In conclusion, OpenFOAM provides an extensive as well as flexible framework to conduct CFD simulations. Furthermore, it allows the user to combine existing solvers to make new solvers for the necessary requirements. In addition to its extensive library of physio-chemical models, OpenFOAM also allows to formulate new models that may be pertinent to the application. Hence, for the purpose of this thesis, OpenFOAM was utilized in conducting the CF-PD simulations. Figure 3.7 shows the major steps that were used in conducting the OpenFOAM simulations.

```

/*-----*- C++ -*-----*/
|=====|
|  \ \ /  /  F i e l d      | OpenFOAM: The Open Source CFD Toolbox
|  \ \ /  /  O p e r a t i o n | Version: dev
|  \ \ /  /  A n d           | Web:      www.OpenFOAM.org
|  \ \ /  /  M a n i p u l a t i o n |
|-----*/
FoamFile
{
    version      2.0;
    format       ascii;
    class        dictionary;
    location     "system";
    object       controlDict;
}
// ***** //
application     icoFoam;
startFrom       latestTime;
startTime       0;
stopAt          endTime;
endTime         10;
deltaT          0.05;
writeControl    timeStep;
writeInterval   20;
purgeWrite      0;
writeFormat     ascii;
writePrecision  6;
writeCompression off;
timeFormat      general;
timePrecision   6;
runTimeModifiable true;
// ***** //

```

Figure 3. 5. controlDict file in the system directory.

```

/*-----*- C++ -*-----*/
|=====|
|  \ \ /  /  F i e l d      | OpenFOAM: The Open Source CFD Toolbox
|  \ \ /  /  O p e r a t i o n | Version: dev
|  \ \ /  /  A n d           | Web:      www.OpenFOAM.org
|  \ \ /  /  M a n i p u l a t i o n |
|-----*/
FoamFile
{
    version      2.0;
    format       ascii;
    class        dictionary;
    location     "system";
    object       fvSchemes;
}
// ***** //
ddtSchemes
{
    default      Euler;
}
gradSchemes
{
    default      Gauss linear;
}
divSchemes
{
    default      none;
    div(phi,U)   Gauss limitedLinearV 1;
}
laplacianSchemes
{
    default      Gauss linear corrected;
}
interpolationSchemes
{
    default      linear;
}
snGradSchemes
{
    default      corrected;
}
// ***** //

```

Figure 3. 6. fvSchemes file in the system directory.

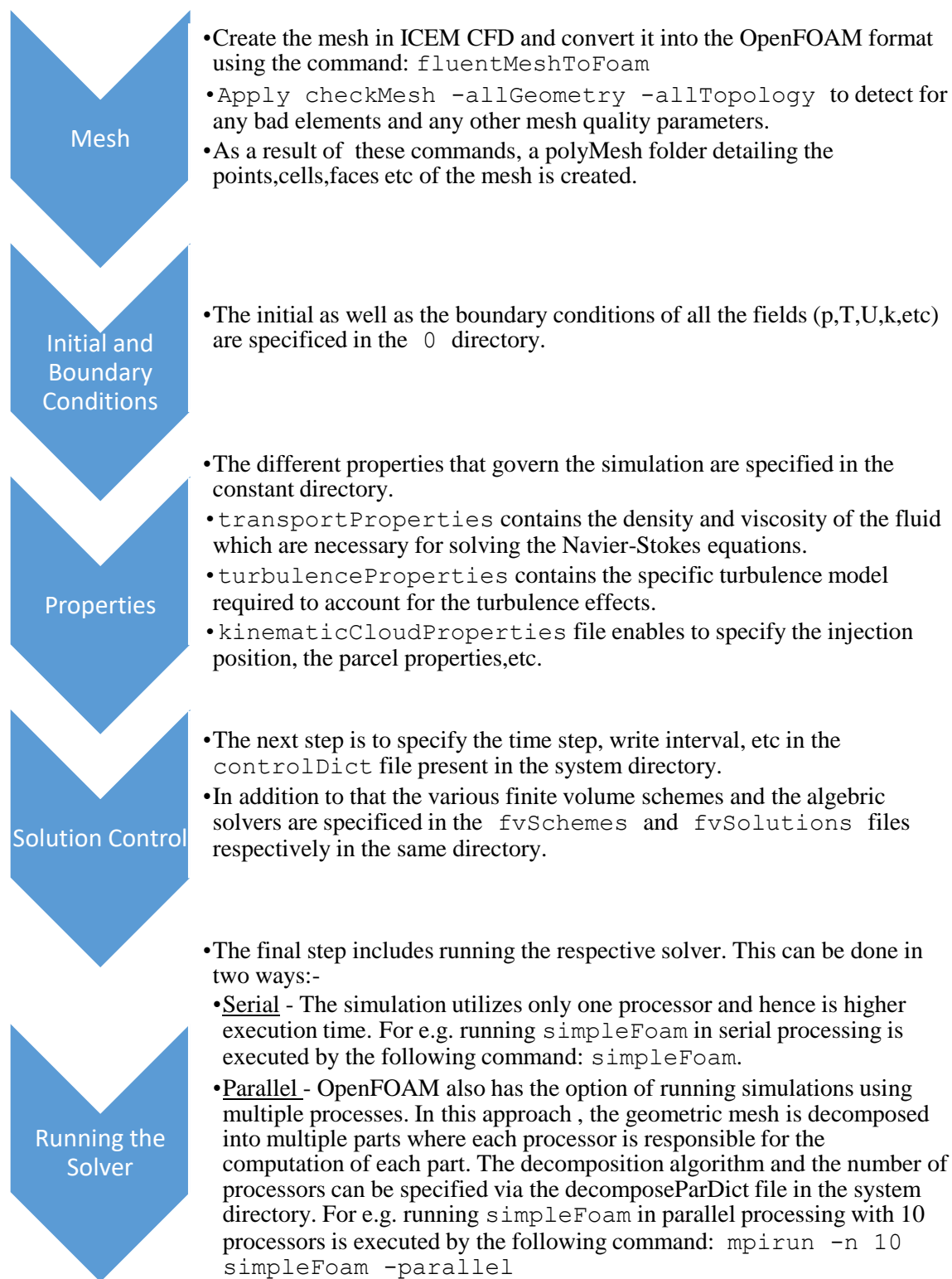


Figure 3. 7. Workflow for conducting OpenFOAM simulations.

3.3. Case Set-up

As explained earlier, this study involves conducting one-way coupled fluid-particle dynamics simulations to determine the particle deposition efficiencies. The focus is on human nasal regions with an emphasis on the olfactory bulb for nanodrug migration across the BBB to the brain. This section underlines the case set-up for conducting this study. To conduct these one-way coupled simulations, the flow evolves first followed by conducting the particle tracking simulation using that flow field. OpenFOAM's steady state, incompressible, turbulent solver `simpleFoam` is used for conducting the steady simulations. Consequently, the convergent flow field is used in `icoUncoupledKinematicParcelFoam` (OpenFOAM's lagrangian solver) to keep track of the particles.

For solving the flow using `simpleFoam`, it is essential to specify the viscosity model as well as the density and kinematic viscosity of the fluid. Figure 3.8 shows the `transportProperties` file used in the current study.

```
/*-----*- C++ -*-----*\
| ===== |
| \\      / F i e l d      | OpenFOAM: The Open Source CFD Toolbox |
| \\      / O p e r a t i o n | Version: 2.2.2 |
|  \\    / A n d           | Web:      www.OpenFOAM.org |
|  \\\\   M a n i p u l a t i o n |
\*-----*\
FoamFile
{
    version      2.0;
    format       ascii;
    class        dictionary;
    location     "constant";
    object       transportProperties;
}
// *****

transportModel Newtonian;

rho          rho [ 1 -3 0 0 0 0 ] 1.2754;

nu           nu [ 0 2 -1 0 0 0 ] 1.48e-05;

// *****
```

Figure 3. 8. `transportProperties` file.

For `icoUncoupledKinematicParcelFoam` it is essential to determine the particle properties will govern their trajectory. As mentioned these properties are specified using the `kinematicCloudProperties` file. Figure 3.9 shows a snippet of the file to show the syntax for providing information regarding the properties of particles, the forces acting on the particles and the injection model to be specified.

```

constantProperties
{
    rho0          1000;
    youngsModulus 6e8;
    poissonsRatio 0.35;
}
subModels
{
    particleForces
    {
        GanserDrag
        {
            phi 1.0;
            a   0.1118;
            b   0.6567;
            c   0.4305;
            d   3305.0;
        }
    }
    gravity;
}
injectionModels
{
    modell
    {
        type          patchInjection;
        parcelBasisType fixed;
        patch          baff1e1_master;
        nParticle      1;
        parcelsPerSecond 2e9;
        massTotal      0;
        U0             (0 0 0);
        flowRateProfile constant 1;
        SOI 0;
        duration       5e-5;
        sizeDistribution
        {
            type          fixedValue;
            fixedValueDistribution
            {
                value 5e-6;
            }
        }
    }
}

```

Figure 3. 9. Snippet of the `kinematicCloudProperties` file.

3.4. Boundary Conditions

It is essential to specify the boundary conditions for all the necessary flow and temperature fields to solve the necessary partial differential equations. In addition to the interior cells, the computational domain also consists of “ghost cells”. Ghost cells are layer(s) of cells that mirror the boundary adjacent interior cells whose values are specified by these boundary conditions. The initial and boundary conditions of the pertaining flow-fields (velocity, pressure, velocity etc.) are set in the 0 folder.

There are three basic boundary conditions in the field of Computational Fluid Dynamics:

- Dirichlet: - When using a Dirichlet boundary condition, a particular value is assigned to the variables at the boundary. e.g. $u(x) = constant$.
- Neumann: - When using a Neumann boundary condition, the gradient normal to the boundary is specified for the variable. e.g. $\partial_n^{u(x)} = constant$.
- Mixed: - This is the mixture of the aforementioned boundary conditions and takes the following form: $a u(x) + \partial_n^{u(x)} = constant$.

Table 3. 1 Boundary conditions for Velocity and Pressure.

Boundary	Velocity		Pressure	
	Type	Syntax	Type	Syntax
NASALINLET	Dirichlet	fixedValue	Neumann	zeroGradient
NASAL	No slip	noSlip/fixedValue	Neumann	zeroGradient
NASOPHARYNX	No slip	noSlip/fixedValue	Neumann	zeroGradient
OUT	Neumann	zeroGradient	Dirichlet	fixedValue set to uniform 0

Table 3. 2 Boundary conditions for Turbulent Kinetic Energy and Turbulence Dissipation Frequency.

Boundary	Turbulent Kinetic Energy		Turbulence Dissipation Frequency	
	Type	Syntax	Type	Syntax
NASALINLET	Dirichlet	fixedValue	Dirichlet	fixedValue
NASAL	Dirichlet	kqR WallFunction	Dirichlet	omega WallFunction
NASOPHARYNX	Dirichlet	kqR WallFunction	Dirichlet	omega WallFunction
OUT	Neumann	zeroGradient	Neumann	zeroGradient

For a given boundary, different types of boundary conditions can be used for different variables. Table 3.1 shows the pressure and velocity boundary conditions while Table 3.2 shows the boundary conditions for the turbulence parameters: Turbulence Kinetic Energy and Specific Dissipation Frequency. The detailed description for the boundary conditions is given below:

```
<patchName>
{
    type
    <Boundary Condition Type>;
    value
    uniform <Specific Value>;
}
```

<patchName> is used to specify the name of the boundary patch as per the mesh.

`type` is used to specify the name of the boundary condition recognized by the solver.

`value`, as the name suggests denotes the specific value (scalar or vector) of the boundary condition.

The type options used in this particular study are as follows:-

- **fixedValue:-** This option maintains a particular value at the boundary patch. It is a type of Dirichlet boundary condition. The value needs to be specified under the `value` option. E.g. `uniform (0 1 0)` for a vector, `uniform 2.0` for a scalar etc.
- **noSlip:-** This is special type of `fixedValue` boundary condition whose value is 0.
- **zeroGradient:-** This option indicates that the gradient of the variable normal to the boundary is 0. It is a type of Neumann boundary condition.

$$\frac{\partial \mathbf{u}}{\partial \mathbf{n}} = \mathbf{0} \quad (3.1)$$

\mathbf{u} corresponds to the particular variable and \mathbf{n} is the normal vector to the boundary patch.

As explained in Section 2.3, certain flowrates used for this study correspond to transitional regimes and hence it is essential to model the effects of turbulence. The existence of turbulence creates random fluctuations and as a result the velocity profile and wall effects are different from the laminar regime. A non-dimensional number y^+ (Eq) is used to divide the region near the wall into three parts: viscous sublayer, buffer layer and log-law region.

$$y^+ = \frac{u_\tau y}{\nu} \quad (3.2)$$

where u_τ (eq) is the shear velocity, y is the distance from the wall and ν is the kinematic viscosity of the fluid.

$$u_\tau = \sqrt{\frac{\tau_w}{\rho}} \quad (3.3)$$

τ_w is the wall shear stress and ρ is the density of the fluid.

$$\begin{aligned}
& \text{Viscous Sublayer for } y^+ < 5 \\
& \text{Buffer Layer for } 5 < y^+ < 30 \\
& \text{Log – law layer for } 30 < y^+ < 200
\end{aligned}
\tag{3.4}$$

y^+ value can be thought of as a local Reynolds number and shows the relative significance between the turbulent and viscous stresses. Viscous Sublayer is the region closest to the wall where the laminar stresses are dominant. In the buffer region the stresses are of the same order while the log-law makes up >90% of the region where turbulence dominates. Due to its transitional nature, it is difficult to capture the flow-field physics of the buffer layer unlike the other two other layers. Hence there is a need for empirical wall functions; for example, `kqRWallFunction` and `omegaWallFunction` are options for the turbulence kinetic energy (k) and turbulent dissipation rate (ω), respectively. These two turbulence parameters are essential to form a closed system of turbulence equations that are required to resolve the flow completely. `kqRWallFunction` is a `zeroGradient` type of Neumann boundary condition. `omegaFunction` has a functionality of changing the value based on the y^+ value.

The syntax for the aforementioned wall functions is similar to that of that of pressure and velocity. In addition to the initial and boundary conditions, the case set-up also requires the numerical schemes that are being used to solve the partial differential equations.

3.5. Numerical Schemes

The Navier-Stokes equations are a set of non-linear partial differential equations that govern the physics of the flow. These equations are not theoretically solvable and hence the need for Computational Fluid Dynamics (CFD) studies. CFD involves converting these complex equations into simple algebraic equations using certain numerical schemes. For the purposes of stability, convergence and accuracy, it is important to select the appropriate numerical schemes.

Table 3. 3. Numerical Schemes used in simpleFoam.

Differential Operation	Sub-Directory	Variable	Scheme Used
Divergence	divSchemes	u	bounded Gauss linearUpwind
		k	bounded Gauss limitedLinear 1
		ω	bounded Gauss limitedLinear 1
		ε	bounded Gauss limitedLinear 1
Temporal	ddtSchemes	u	Euler
Gradient	gradSchemes	u	Gauss linear
Laplacian	laplscianSchemes	u	Gauss linear corrected
Interpolation	interpolationSchemes	u	Linear

$$\underbrace{\nabla \cdot \vec{u}} = 0 \quad (3.5)$$

Divergence

$$\underbrace{\frac{\partial \vec{u}}{\partial t}} + (\vec{u} \cdot \nabla) \vec{u} = g + \underbrace{\frac{\mu}{\rho} \nabla^2 \vec{u}} - \frac{1}{\rho} \underbrace{\nabla p} \quad (3.6)$$

Temporal

Laplacian

Gradient

Eq. 3.5 and 3.6 show the incompressible Navier-Stokes equations along with the various differential operators. OpenFOAM provides the opportunity to specify a separate scheme for each of the differential operators.

Table 3.3 shows the various numerical schemes used in the `simpleFoam`. These are mentioned under the `fvSchemes` dictionary in the system directory. It also shows the sub-dictionaries corresponding to the differential operators. The finite-volume method solves for the average value of the system variables. However, the aforementioned numerical schemes require the values at the boundary of each cell. Hence the need for the `interpolationSchemes` sub-dictionary. These schemes can be adjusted as per the requirements of the problem.

3.6. Solution Control

Table 3. 4. Algebraic solvers used in `simpleFoam`.

Variable	Solver	Smoother
U	<code>smoothSolver</code>	<code>GaussSeidel</code>
P	<code>GAMG</code>	<code>GaussSeidel</code>
K	<code>smoothSolver</code>	<code>GaussSeidel</code>
Ω	<code>smoothSolver</code>	<code>GaussSeidel</code>

Once the differential equations are converted into algebraic equations by the appropriate numerical schemes, certain algebraic solvers are used to get the values of the field variables at each time step. The choice of the solvers affects the computational time and stability of the simulation. Table 3.4 shows the algebraic solvers used for the system variables. `GAMG` (Generalized geometric algebraic multi-grid) solver is used for pressure while the `smoothSolver` is used for the rest of the variables. `GAMG` is a multi-grid solver and is considerably faster than the standard methods. This solver generates a quick solution for a coarser mesh, maps this solution onto the finer mesh and using it as an initial guess. The `smoothSolver` uses a standard Gauss Seidel approach to calculate the solution.

CHAPTER 4. MODEL VALIDATIONS

4.1. Introduction

Predictive computational fluid-particle dynamics (CF-PD) simulations are an essential tool to analyze complex fluid systems that are otherwise too costly and intricate to evaluate *in vitro*. *In vivo* studies of, say, the nasal cavity, are difficult to undertake due to the delicate nature of the organs involved. Hence the need for conducting “computer experiments” that capture the physics of the problem with reasonable realism and accuracy. These CF-PD simulations allow evaluating the impact of significant parameters (e.g., system configuration, flowrate, particle diameter, etc.) and eliminating extraneous factors. This chapter is divided into multiple sections based on different case studies that have been validated. As explained earlier, these simulations are carried out using an open source CF-PD toolbox named OpenFOAM®. These validations were necessary as they confirm the validity of the solvers and models available in OpenFOAM. Section 4.3 compares the Euler-Lagrange approach used for tracking micron-size particles inside the nasal cavity with the results presented by Calmet et al., 2018(60). Section 4.4 discusses the legitimacy of the Lagrangian approach for nanoparticle tracking. Numerical simulation results are compared with an analytical solution presented by Ingham, 1975 (76). Section 4.4 compares the Euler-Lagrange approach used for tracking nanoparticles inside the nasal cavity with the results presented by Tian et al., 2019(69). As the thesis involves studying particle deposition, it is pivotal to mention the methodology behind the Euler-Lagrange particle tracking solvers in OpenFOAM. For steady-state simulations of the Eulerian phase, OpenFOAM uses the SIMPLE (Semi-Implicit Method for Pressure-Linked Equations), while employing the PIMPLE algorithm for transient cases. The PIMPLE algorithm is a combination of the PISO (Pressure Implicit with Splitting of Operator) and SIMPLE. In each time step, the Eulerian variables (u , p , k , ω , etc.) were solved until residual convergence

(mentioned in the `fvSolutions` directory) was achieved. Consequently, these field variables determined the values of the forces required for tracking the particle cloud.

4.2. Geometry and Mesh of the Representative Nasal Cavities

The geometry of the nasal cavity is shown in Figure 4.1. The figure depicts the nasal cavity and the nasopharynx. Furthermore, there is an extruded portion attached to the nostril to accurately simulate the inhaling action. Figure 4.2 shows the complete view of the nasal cavity from all angles. The complexity of the nasal cavity geometry is evident from these figures; thus, requiring proper care in generating the mesh. The nose geometry is constructed from the MRI scans of a healthy 53 year old, non-smoking male (weighing 73kg and 173 cm tall) provided by CIIT (Research Triangle Park, NC) (77-79).

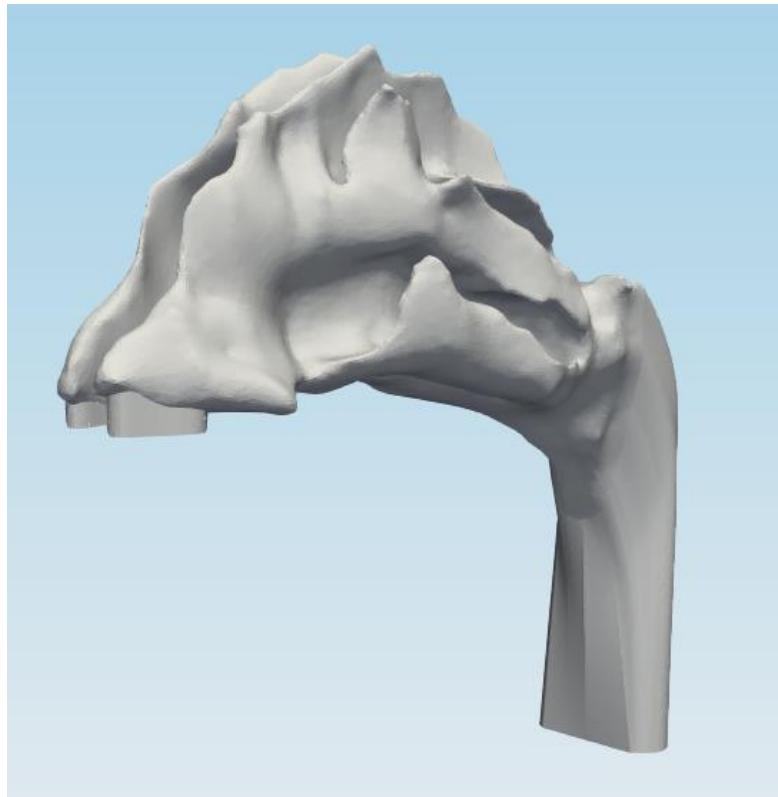


Figure 4. 1. Geometry of the nasal cavity.

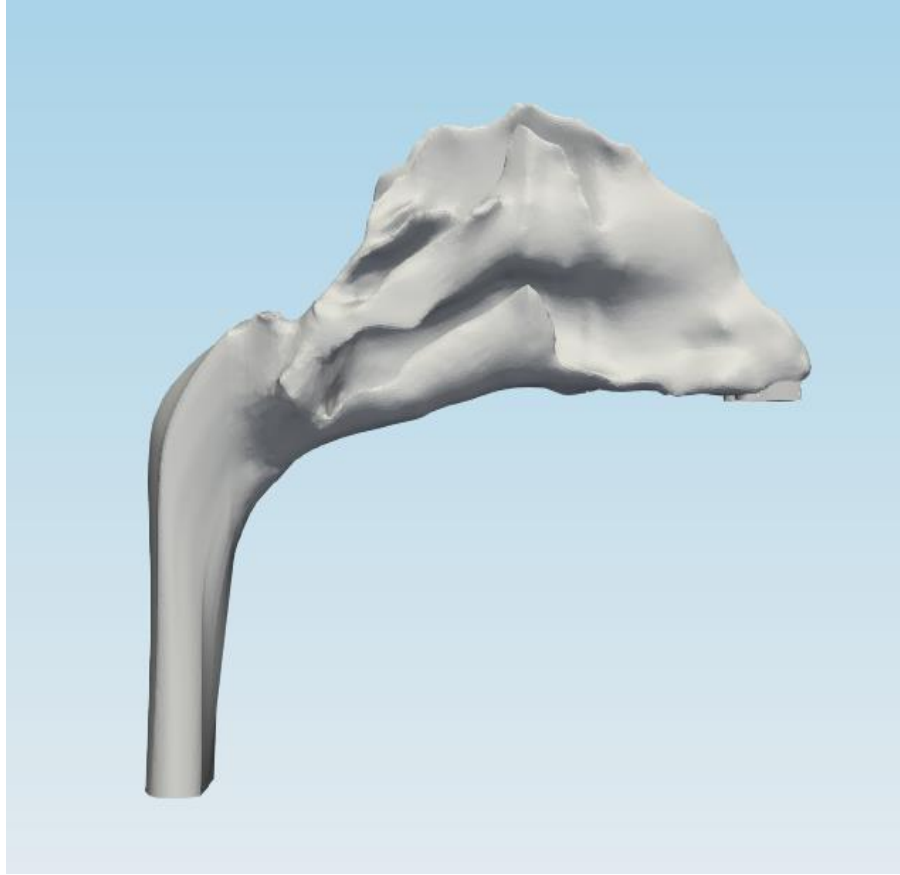


Figure 4. 2. Complete view of the Nasal Cavity Geometry.

Table 4.1 summarizes the various geometrical features of the geometry used. All the measurements are listed in MKS units. Particle deposition is subject-specific, i.e., variations in these geometrical features allow for comparisons between different patients. As a result, correlations can be established between these geometrical parameters and the particle deposition efficiencies.

Table 4. 1. Geometry features of the Nasal Cavity.

Geometry Features	
Length	0.105
Height	0.093
Length/Height	1.129
Area	0.02280071
Volume	3.22981e-5
Area/Volume	705.945
Nostril Length	0.0111965
Nostril width	0.0040418

Computing with this geometry requires that mesh discretization is of high quality. To capture the intricacies of the computational domain, an unstructured mesh was created using ANSYS ICEM CFD (ANSYS Inc., USA). The procedure for generating the mesh is as follows:

- An octree-based method (80) was used in creating a high resolution surface mesh.
- The resulting surface mesh was then successively smoothed using Laplace smoothing (81) to avoid shrinkage.
- Subsequently a Delaunay approach (82) was used to create a volumes mesh from the surface mesh.

- Finally, prism layers were added to capture the boundary layers.

The final mesh is composed of tetrahedral elements in the core, prism elements along the boundary and pyramid elements in-between to have smooth transition between the elements. The cell size is highest in the core and lowest along the periphery. The finer prism cells serve to accurately capture the near wall physics and the turbulent characteristics of the flow. Due to the complex structure of the nasal cavity, repeated smoothing iterations were performed to ensure that the quality parameters, such as Aspect Ratio and Skewness, are of the minimum threshold required to obtain an accurate solution.

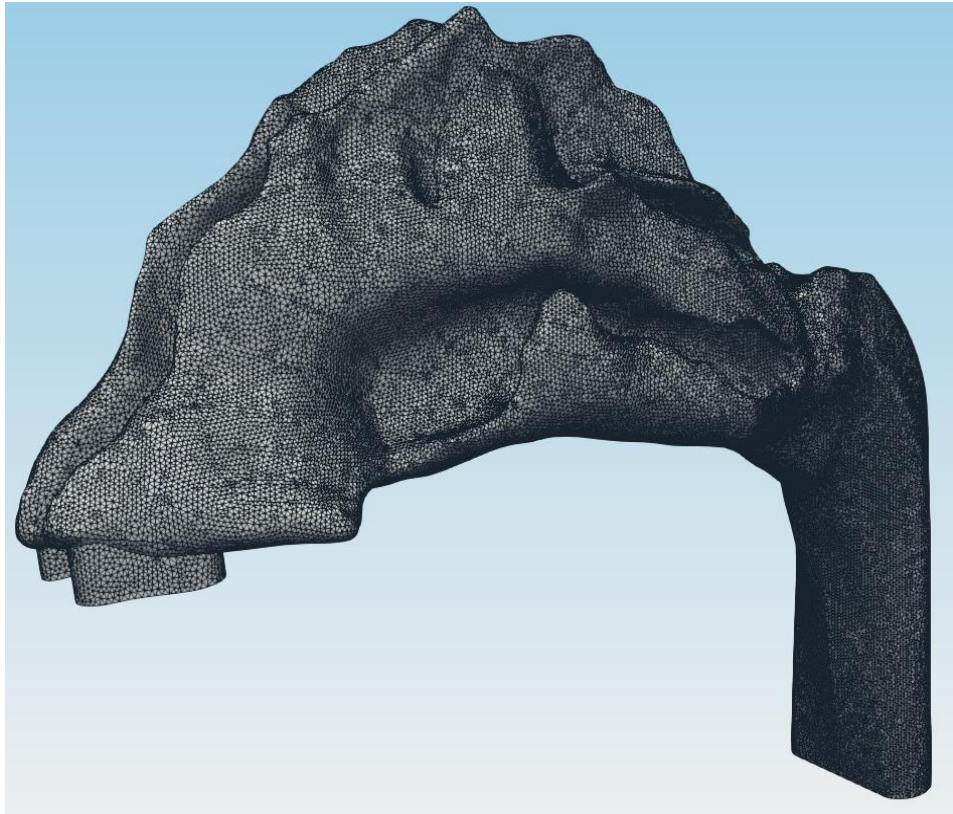


Figure 4. 3. Isometric view of the unstructured mesh of the representative nasal cavity.

Figure 4.3 depicts the hybrid unstructured mesh of the nasal cavity used in conducting the various CF-PD simulations performed, while Table 4.2 provides the descriptive statistics associated

with the aforementioned mesh.

Table 4. 2. Unstructured mesh characteristics.

<u>Mesh Statistics</u>	
Number of Points	1071282
Number of Elements	4269286
Number of Faces	9106628
Number of prism elements	906380
Number of tetrahedral elements	3362856
Number of pyramid elements	50
Number of prism layers	4
Minimum edge length	3.08642e-06
Maximum edge length	0.00103895

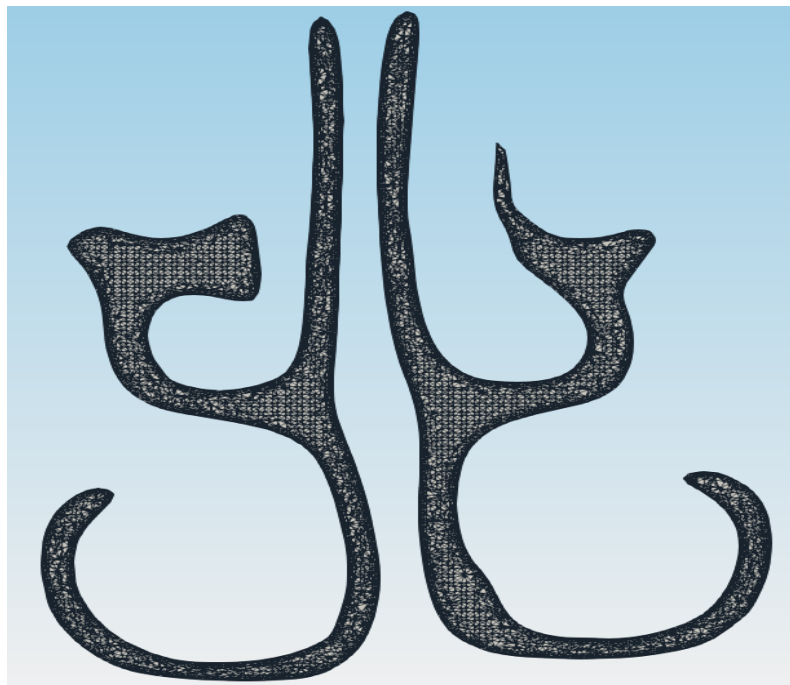


Figure 4. 4. Mesh slice of the mid-section of the nasal cavity.

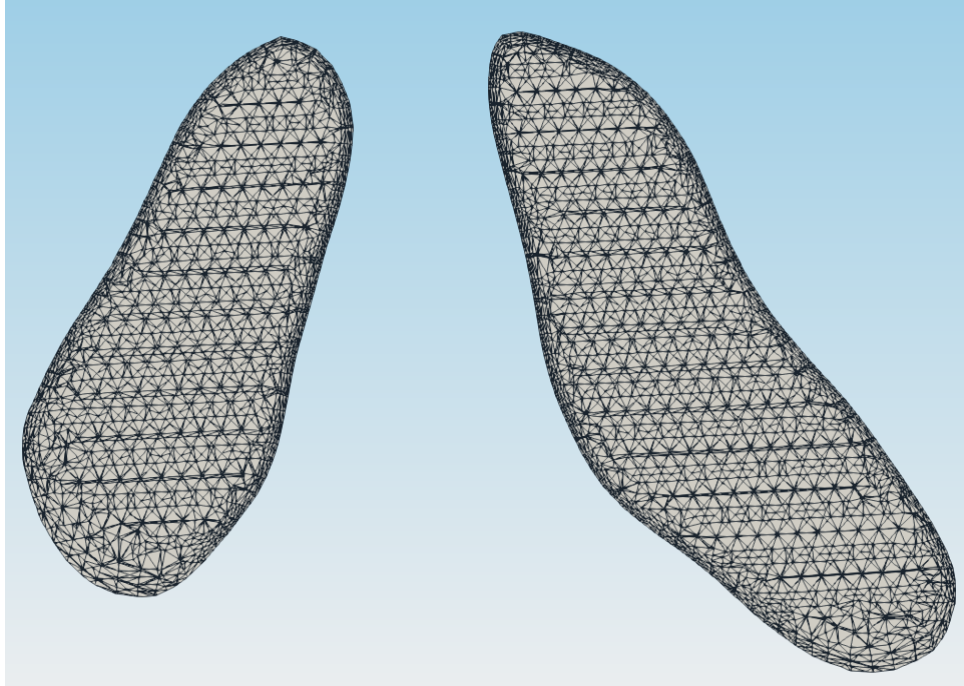


Figure 4. 5. Mesh slice of the nostrils.

4.3. Comparison with Calmet et al., 2018

For model validation, the present results were compared to airflow pattern and particle deposition of Calmet et al., 2018 (60). This was done to confirm the validity of the Lagrangian micron-particle tracking approach used in OpenFOAM®. The paper presents a detailed analysis on the airflow and particle deposition efficiencies for varying flowrates (7.5lpm to 20lpm). Furthermore, a subject-variability study compared the velocity contours and deposition fractions between three different geometries. However, for the purposes of this thesis, only one representative nasal geometry has been considered, namely Subject A which is being used in this thesis.

4.3.1. Airflow Field Results

For the purposes of analyzing the flow field, six slices have been cut into the nasal geometry. The location of these slices are shown in Figure 4.6. The flow is assumed to be steady

and the inlet flowrate is set to be at 20lpm. The velocity contours in each of these slices are given in Figure 4.7, where these are dimensionless velocity contours (u/U_{inlet}) perpendicular to the plane. Furthermore, the dimensionless velocities of the first two slices range until unity and the rest of them range from 0 to 0.75. As it is evident from Slice 1-1', higher velocities are observed in the left nasal cavity because of the smaller cross sectional area for the same inflow rate. The presence of these narrow, intricate pathways creates a jet-like flow. Slice 2-2' shows the undulating pathway inside the nasal cavity. It also indicates that the bulk velocity is located in the middle where the superior portion receives zero flowrates.

Slices 3-3' to 5-5' in Figure 4.8 cover the region of the nasal cavity known as the meatuses. These slices indicate that there is a near symmetric flow distribution in the left and right meatuses with slight differences due to the unusual asymmetry in the middle-meatus region. Slice 6-6' (Figure 4.8) marks the end of the nasal cavity and the start of the nasopharynx. It shows an asymmetric velocity distribution with the posterior region with elevated flowrates due to the presence of Dean Vortices. This is resulting from the geometry undergoing a 90° bend from the nasal passages to the descending nasopharynx. In summary, the airflow entering through nostrils undergoes a drastic change as it traverses through the complicated, undulating pathways of the nasal cavity. Most of the air flows through the wider middle-to-lower portion of the cavity that are free of obstacles. As the air passes, due to the no-slip condition boundary layer forms along the boundary of the main meatuses and the main passageway. Finally, airflow from both the passageways converge in the nasopharynx. Wall shear stress is an important factor representing the resistance to the flow during respiration. Figure 4.9 shows the wall shear stress contour of the nasal cavity for a flowrate of 20lpm. Through the figure it can be observed that the maximum wall shear

stress is observed in the nasal valve. This is because the change in the direction of the flow directs the core of the flow closer

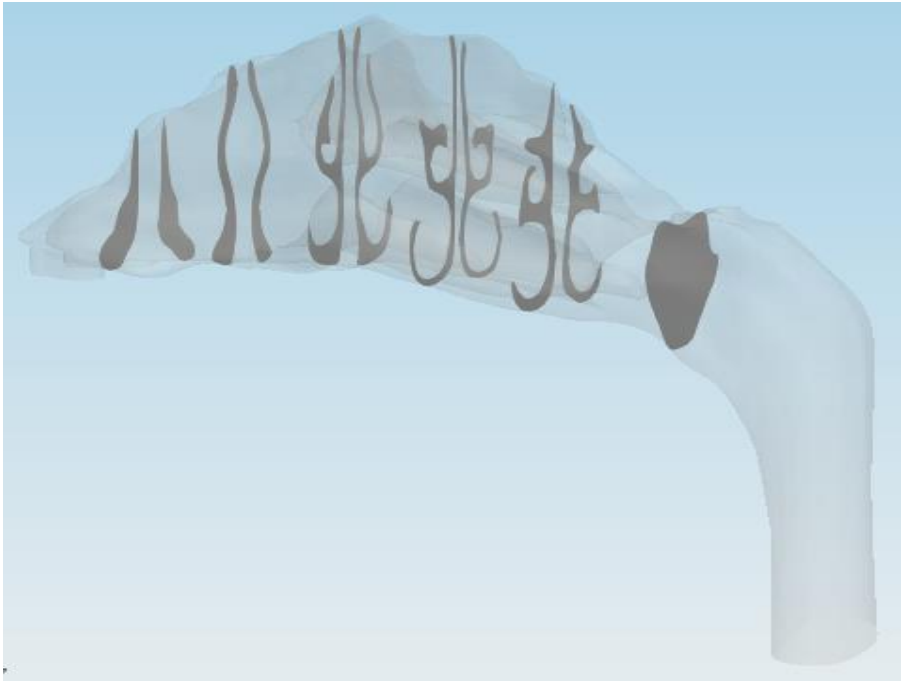


Figure 4. 6. Slices 1-1' to 6-6' (left to right) of the nasal geometry.

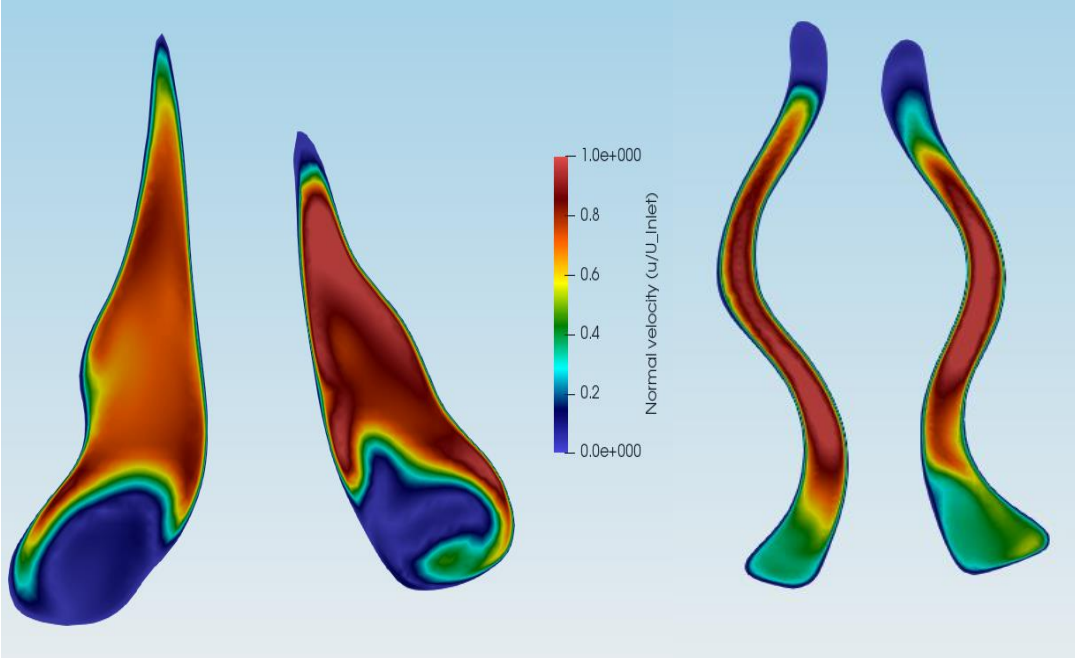


Figure 4. 7. Velocity contours (Slice 1-1' and 2-2').

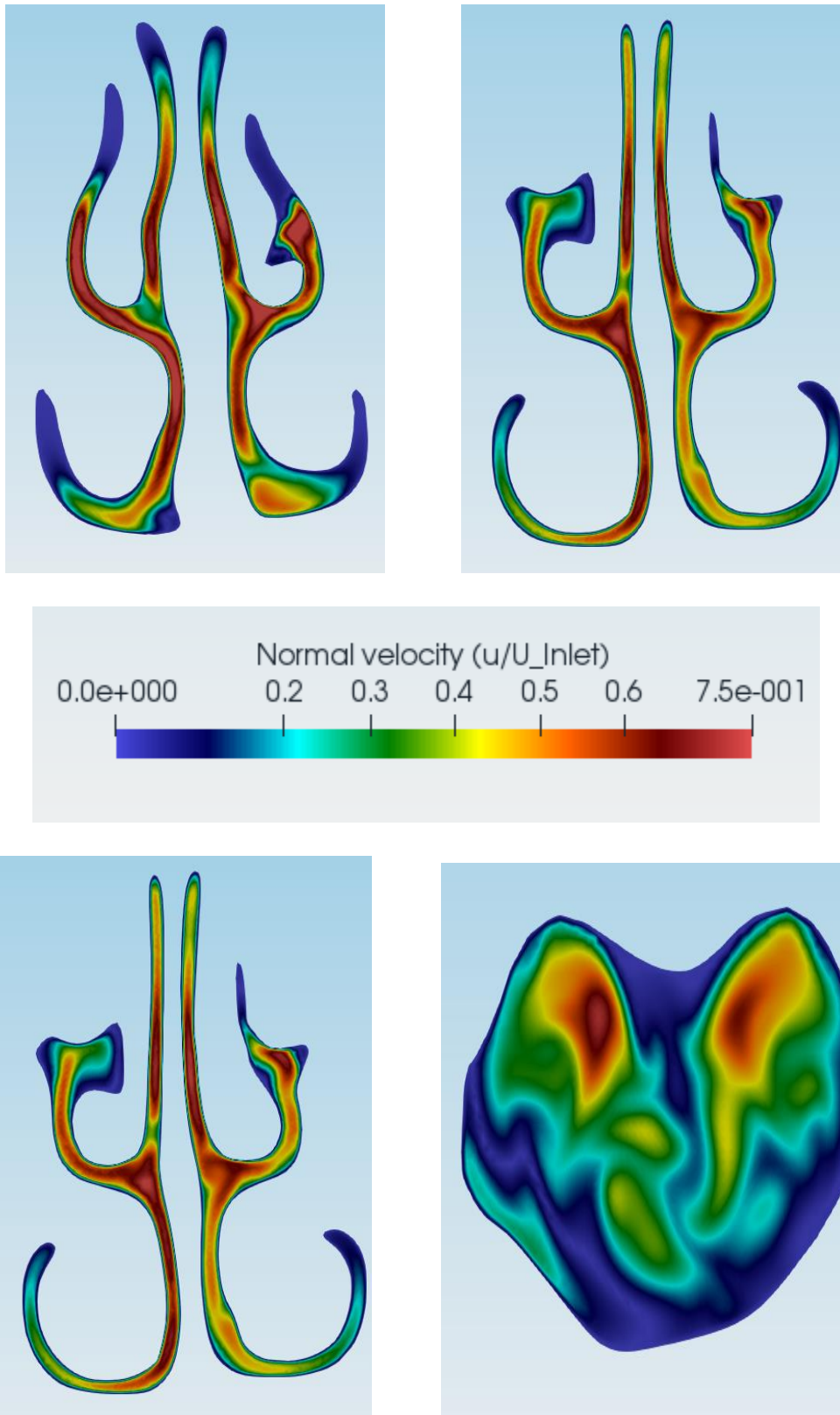


Figure 4. 8. Velocity contours (Slice 3-3' to Slice 6-6').

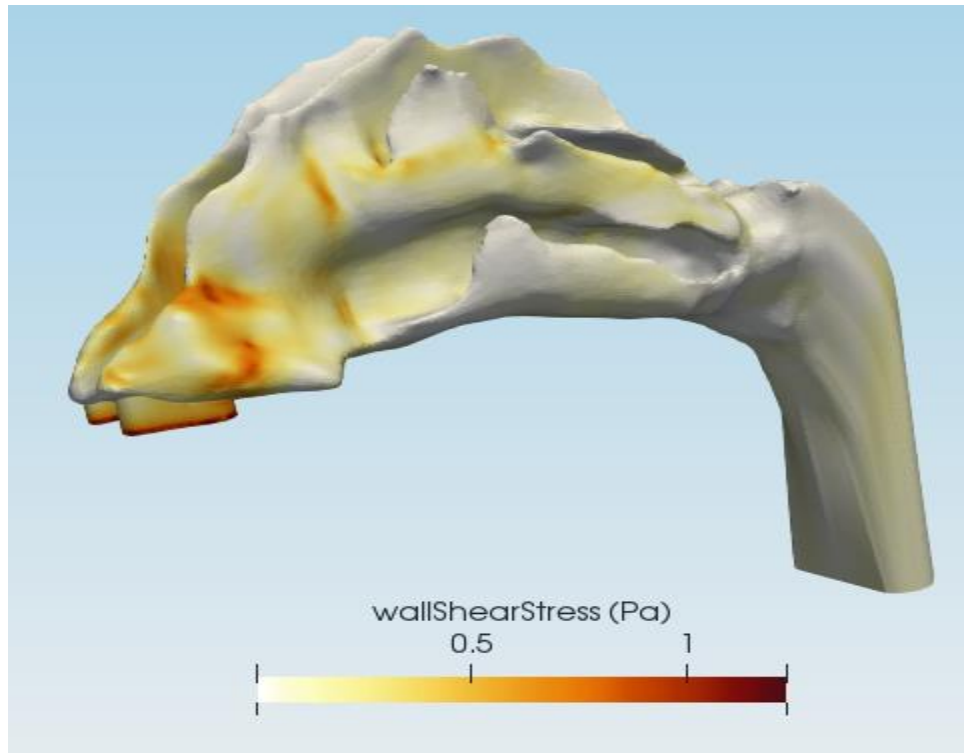


Figure 4. 9. Wall Shear Stress contour of the nasal cavity for 20 lpm.

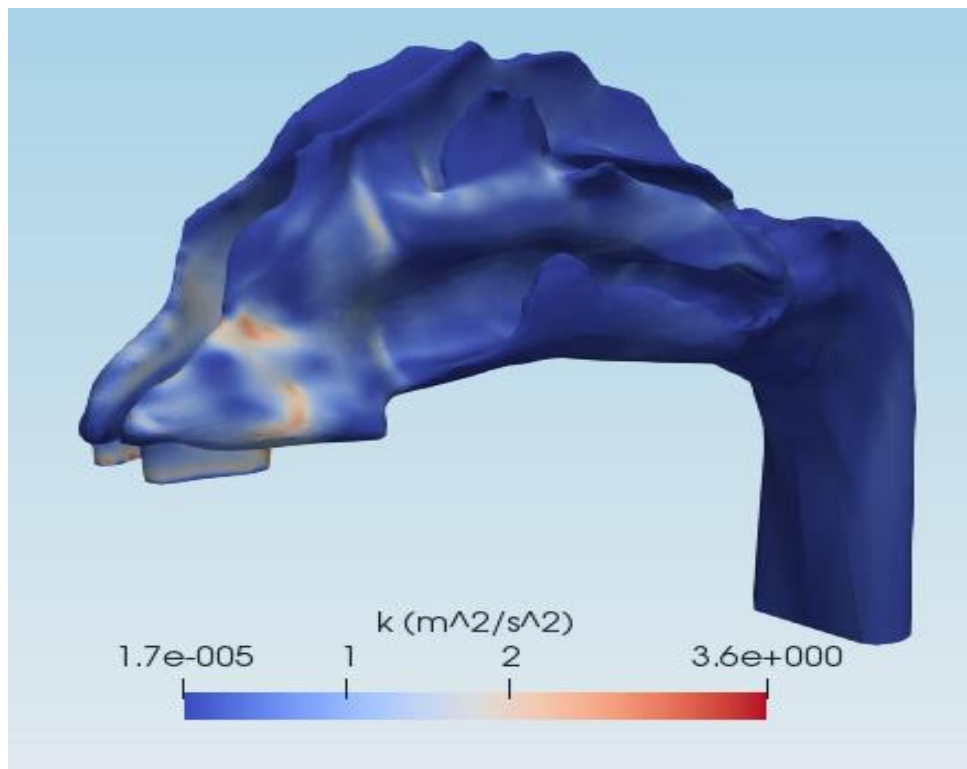


Figure 4. 10. Turbulent kinetic energy contour of the nasal cavity for 20 lpm.

towards the wall thereby resulting in elevated wall shear stresses. Aside from that there are local maxima observed on the complex, undulating curved protrusions above the middle turbinates. These complex structures partition the flow thereby exposing the nasal lining the flow thus increasing the wall shear stress. It is noteworthy to mention that the qualitative distribution of turbulent kinetic energy (Figure 4.10) closely resembles to that of the wall shear stress. The jet created by the nasal valve creates a region of local turbulence as shown in the figure. A similar explanation can be given for the increased turbulence level above the turbinates. For micron sized particles it is expected to observe particle deposition in these regions corresponding to higher wall shear stress and turbulent kinetic energy.

4.3.2. Particle Deposition Results

4.3.2.1. Total Nasal Deposition

Figure 4.11 shows the particle deposition patterns for 2 μm , 10 μm and 20 μm spheres. As evident from this graphs, the nasal deposition is highly dependent on the particle diameter. Small particles follow somewhat the streamlines while larger microspheres with their inertia cross streamlines, thereby resulting in higher depositions (see Table 4.3). The slight discrepancy in the values may be due to the difference in the number of particles injected. The smaller particles go with the flow and escape through the nasopharynx, while the larger particles deposit inside the nasal cavity due to the dominating effects of inertia and secondary flows.

Table 4. 3. Comparison of particle deposition efficiencies.

Particle Diameter (μm)	Total Deposition Efficiency %	
	Simulations	Calmet et al. (2018)
20	98.5	97.9
10	53.37	55.65
2	3.32	3.12

4.3.2.2. Sectional Deposition

Next to determining the total deposition, it is also essential to find the spatial deposition in the nasal cavity. Figures 4.12 and 4.13 depict the sectional deposition inside the nasal cavity for 20 μm and 10 μm particles, respectively. Here, 0 in the horizontal axis represents the nose tip and 7 represents the end of the nasopharynx, while 1 to 6 denote the slices shown in Figure 4.6. Hence, the values in the vertical axis denote the particle deposition efficiencies in-between the consecutive slices. In the aforementioned figures, the Sectional Deposition Efficiency is given as:

$$\text{Sectional Deposition Efficiency} = \frac{\text{Number of particles deposited in a particular section}}{\text{Total number of particles inside the geometry}}$$

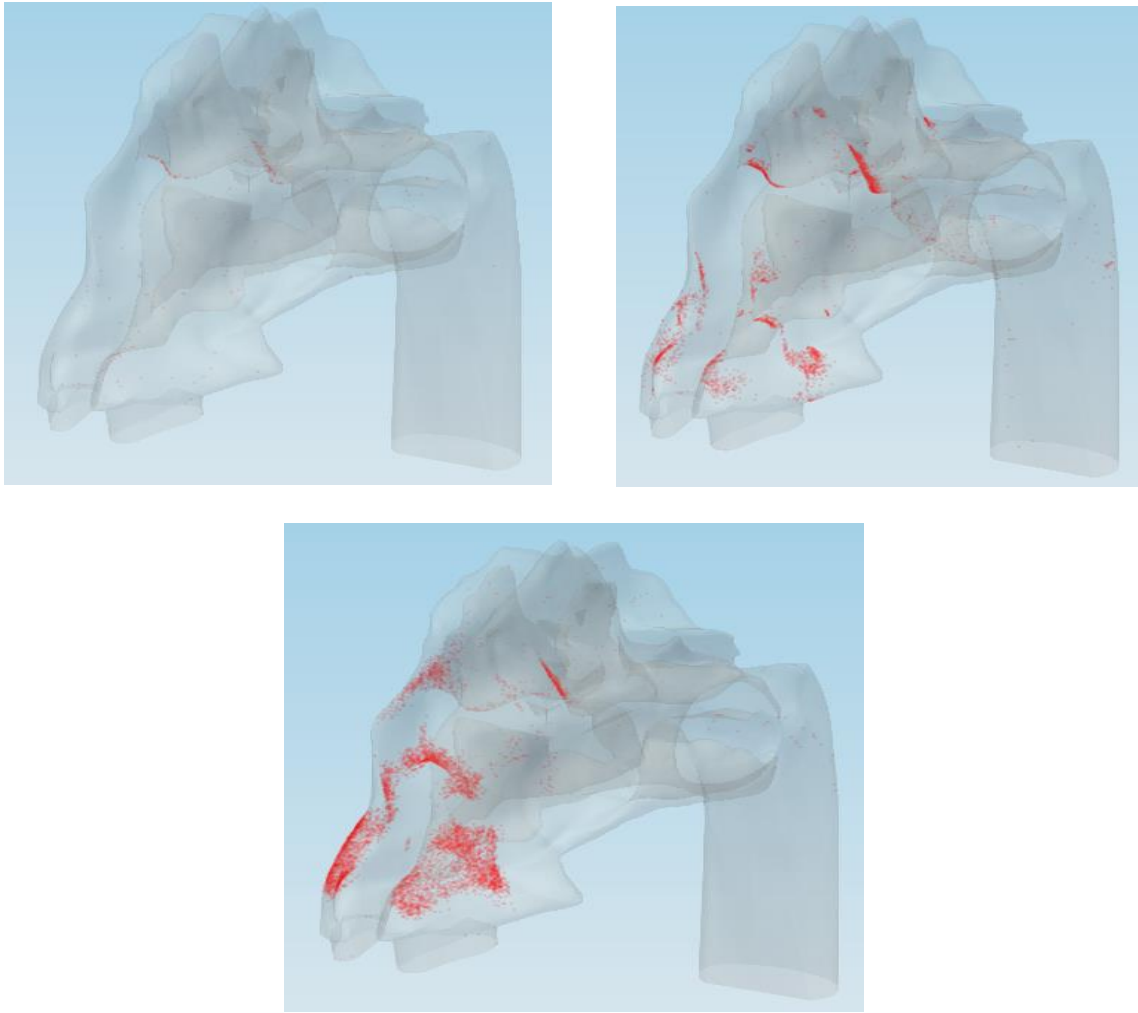


Figure 4. 11. Particle Deposition Pattern for 2, 10 and 20 μm particles (clockwise from the top).

The figures demonstrate that the simulation and previously reported literature results are in very good agreement. The inertial effect on micron-size particles is evident from these figures. Most of the particles are deposited in the vestibule region for 10 μm and 20 μm -sized particles. This is because the inlet flow is in the vertical direction and the inertia of the micron-sized particles enable them to cross the streamlines and deposit in the vestibule region. These particles are unable to follow the flow, which turns horizontal. It is also worthwhile to notice the similarities between the

It is also worthwhile to notice the similarities between the deposition pattern of 20 μm particles and the wall shear stress contour in Figure 4.9. The particle hotspots reasonably matched the high wall shear stress regions of the nasal cavity. Hence it can be concluded that for high inertial particles, hotspots are to be anticipated in the regions of high wall shear stress.

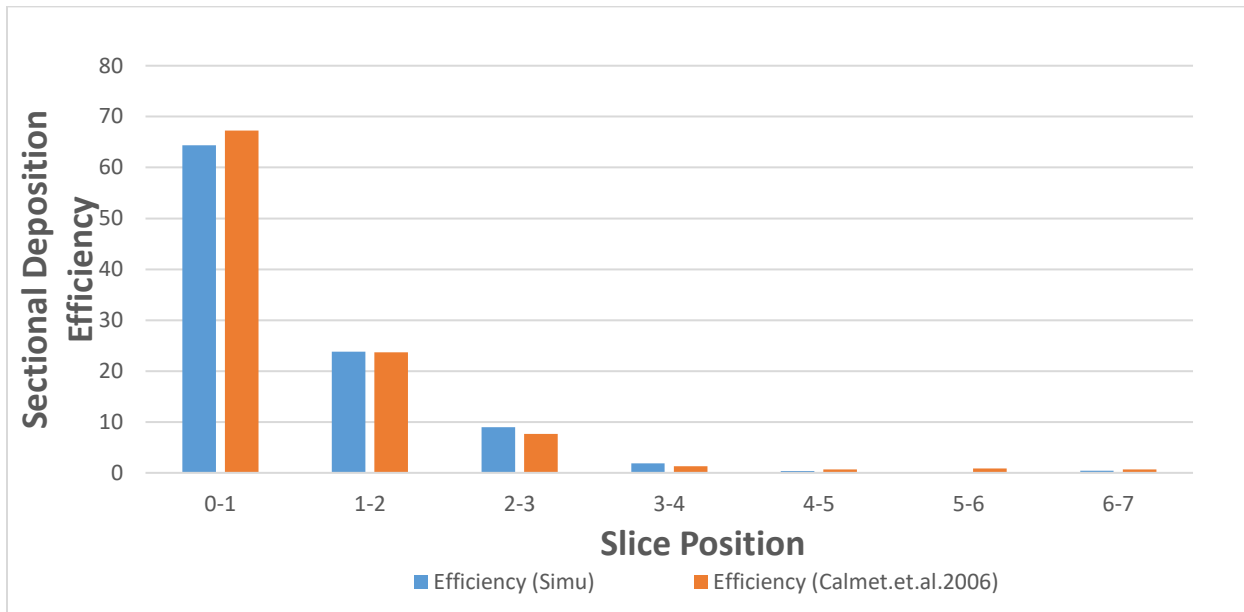


Figure 4. 12. Sectional Deposition for 20 μm particles.

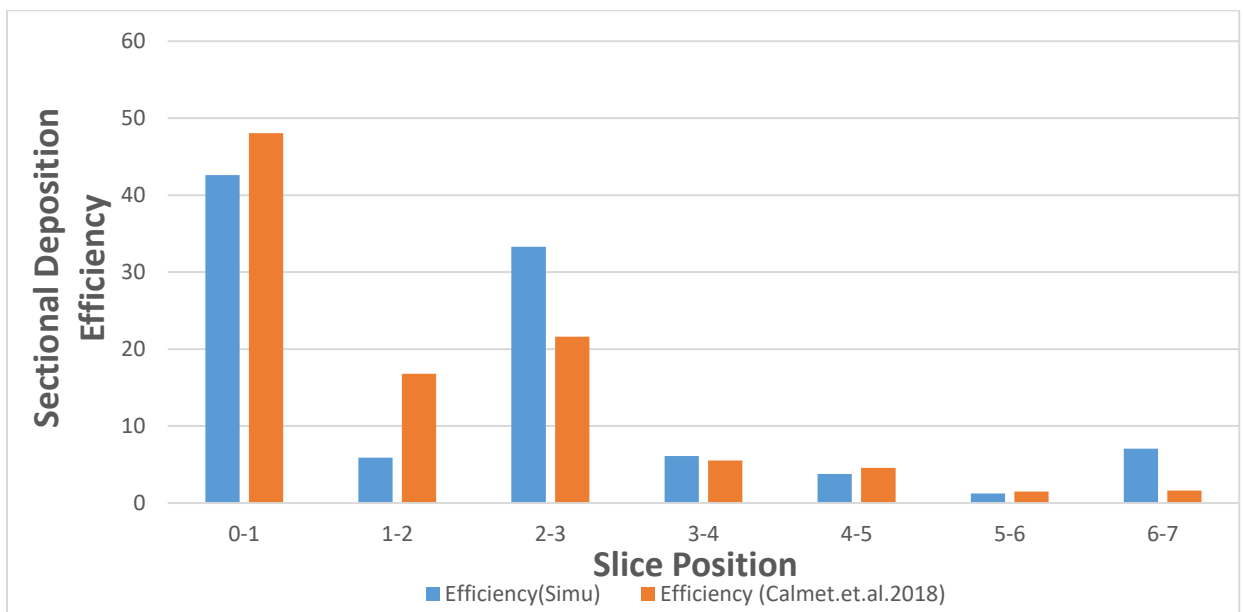


Figure 4. 13. Sectional Deposition for 10 μm particles.

4.4. Comparison with Ingham (1975)

Conventionally nanoparticles are tracked in the Eulerian frame rather than in the Lagrangian phase. However, the Eulerian approach is time intensive and does not offer a lot of flexibility as it pertains to parameters like injector position, number of injected particles, local deposition, site-targeting, etc. Furthermore, the Lagrangian approach offers a more realistic view of the fluid-particle dynamics inside the nasal cavity. In this section, the use of Brownian force, Cunningham drag force and the Saffman lift force (detailed in Section 2.4) for Lagrangian particle tracking of nanoparticles is validated by the analytical results presented by Ingham, 1975 (76). The particles are extremely small and are influenced by the process of diffusion. Typically the species-mass convection-diffusion equation has been employed for nanoparticles of $d_p < 100\text{nm}$. So, this validation not only seeks to establish the accuracy of the solutions but also justifies the approach of using the Lagrangian approach for nanoparticle tracking. This Lagrangian approach has been validated in previous numerical studies as well (83, 84).

4.4.1. Geometry and Mesh

For this validation, a cylinder of diameter 0.0045m and length 0.09m was used, following Ingham (1975). The fluid-particle simulation was carried out with a finely structured mesh comprised of 673721 elements. The mesh was created using an O grid block. The geometry and the mesh used in the study is shown in Figure 4.14 and Figure 4.15, respectively.

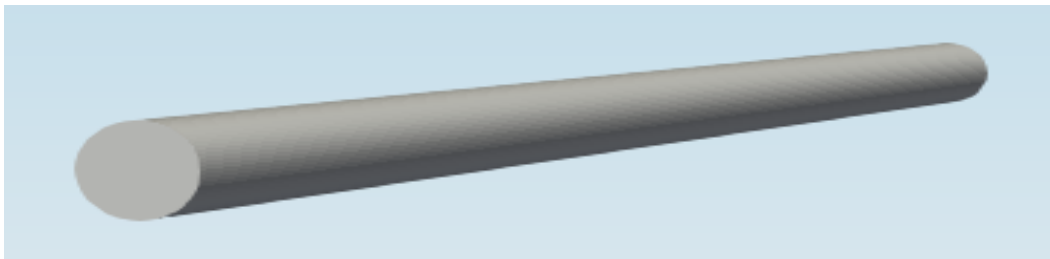


Figure 4. 14. Cylindrical geometry.

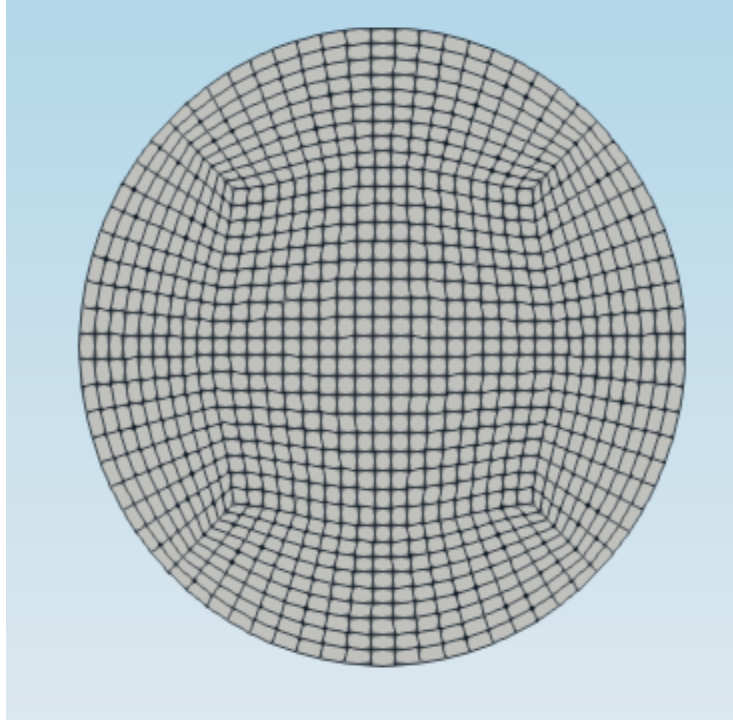


Figure 4. 15. O-grid meshing of the cylinder geometry.

The flow in the pipe was fully developed laminar flow. The particles were distributed from the inlet as:

$$\dot{m}(r) = \dot{m}_0 \left(1 - \frac{r^2}{R^2}\right) \quad (4.1)$$

Ingham (1975) presented the Deposition Efficiency (DE) correlation as follows:

$$DE = 1 - (0.819e^{-14.63\Delta} + 0.0976e^{-89.22\Delta} + 0.0325e^{-228\Delta} + 0.0509e^{-125.9\Delta^{\frac{2}{3}}}) \quad (4.2)$$

where

$$\Delta = \frac{DL_{pipe}}{4U_{inlet}R^2} \quad (4.3)$$

4.4.2. Results and Discussions

As mentioned above, Ingham (1975) produced an analytical solution for the deposition efficiency of particles flowing through a cylindrical tube. In this study the deposition efficiency is

studied for the flowrate of 1lpm (Figure 4.16) and 5lpm (Figure 4.17) which correspond to a Reynolds number of 312 and 1561 respectively. The numerical results are not only compared with the analytical solution as well as results presented by Inthavong et al., 2016 (83).

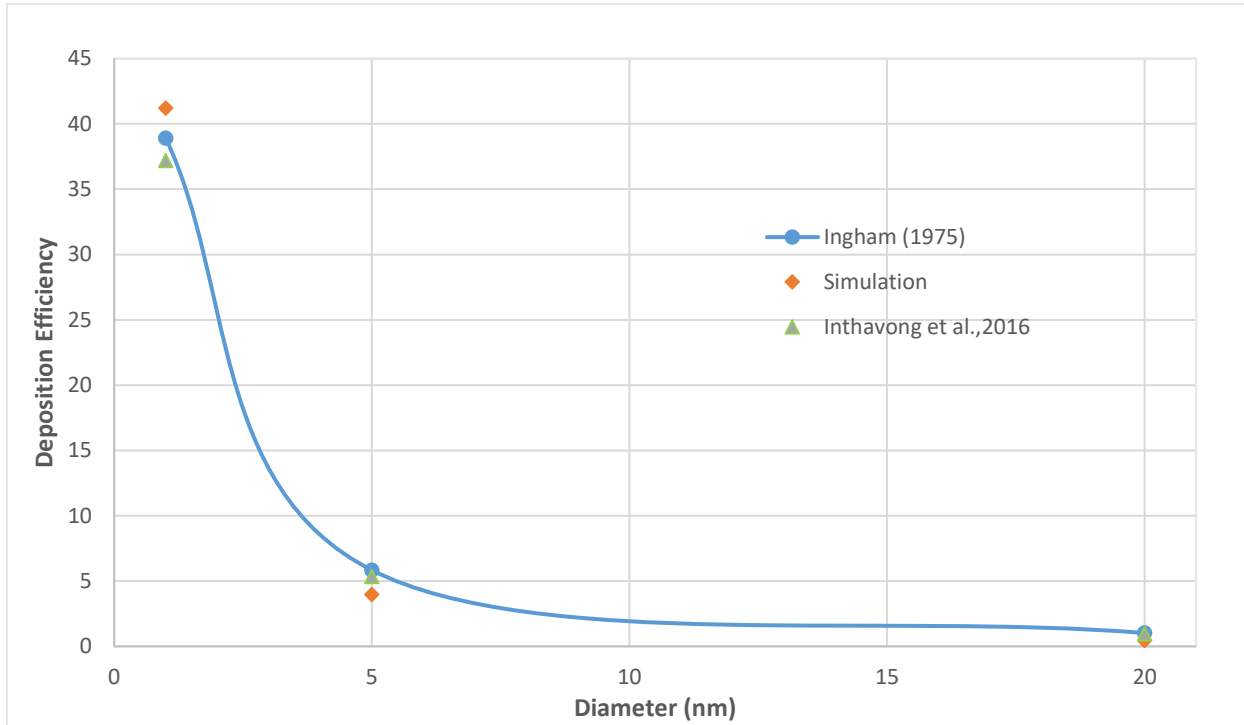


Figure 4. 16. Deposition efficiency comparison for a flowrate of 1 lpm.

As evident from the figures, the computer simulations closely resemble the analytical solution as well as the results presented in (83). The accuracy of nanoparticle deposition efficiency is dependent on the mesh size, the time step, and the number of particles injected. In this study 113,300 nanoparticles were injected and the time step of $1e-4$ was used for time marching of the Lagrangian solution. The slight differences between the different studies can be attributed to the difference in the aforementioned parameters. The graph also illustrates that the larger the nanoparticle size, the lower is their dispersion and consequently a reduction in deposition efficiency occurs. Furthermore, nanoparticle deposition is inversely correlated with the flowrate. Higher flowrates imply stronger inertia and hence more particles are carried away by the flow in

the axial direction, restricting radial dispersion of the nanoparticles. This phenomenon is shown by the maximum deposition efficiency of 41 % in Figure 4.14 and 13.8 % in Figure 4.15.

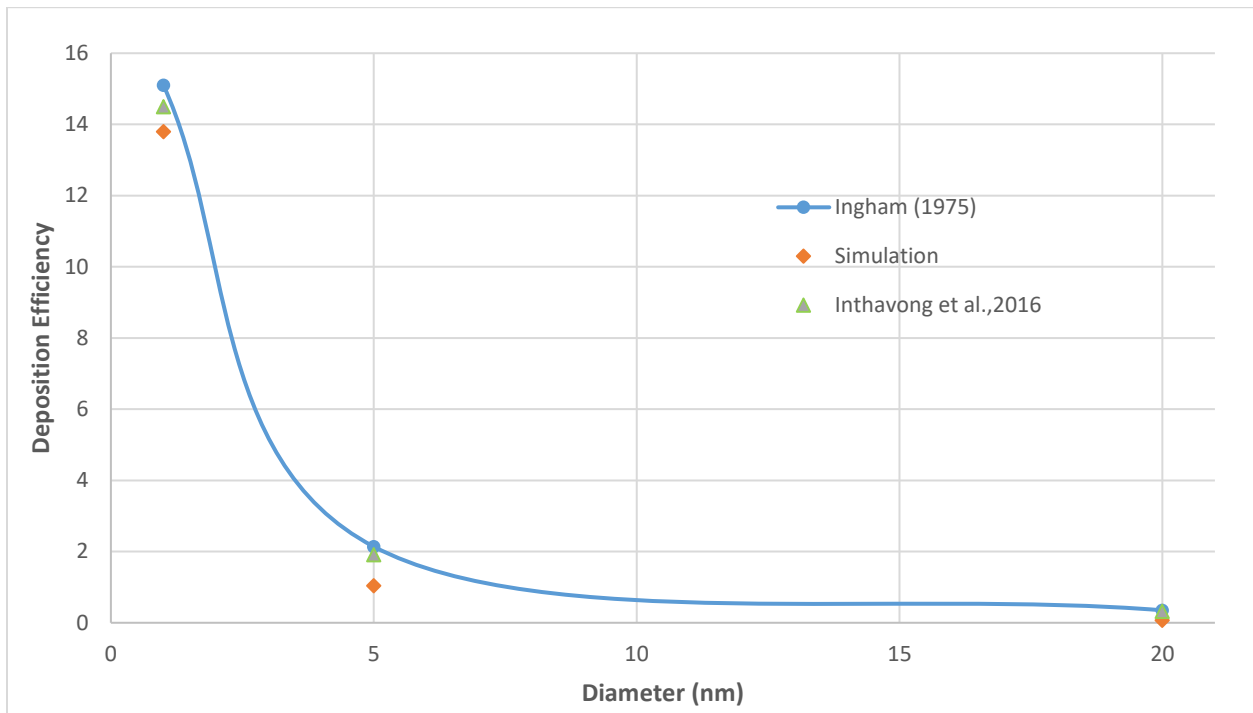


Figure 4. 17. Deposition efficiency comparison for a flowrate of 5 lpm.

4.5. Comparison with Tian et al., 2019

This section validates the nasal and olfactory deposition simulations for nanoparticles. Tian et al., 2019 (69) numerically analyzed the deposition of ultrafine particles (1 to 100 nm) under low and medium breathing rates for a realistic human nasal cavity. Nasal and olfactory depositions are highly subject-sensitive and before establishing any results, a comparison between the geometrical features needs to be done. G1 is the geometry used in the current study (Figure 4.18) and G2 (58) (Figure 4.19) is the geometry used by Tian et al. (2019). Table 4.4 compares the total and olfactory surface area of the nasal cavity between G1 and G2.

It can be seen from Table 4.4 that the area parameters for both the geometries are close and hence a comparative deposition study with the same range of flowrates can be done. However, Figures

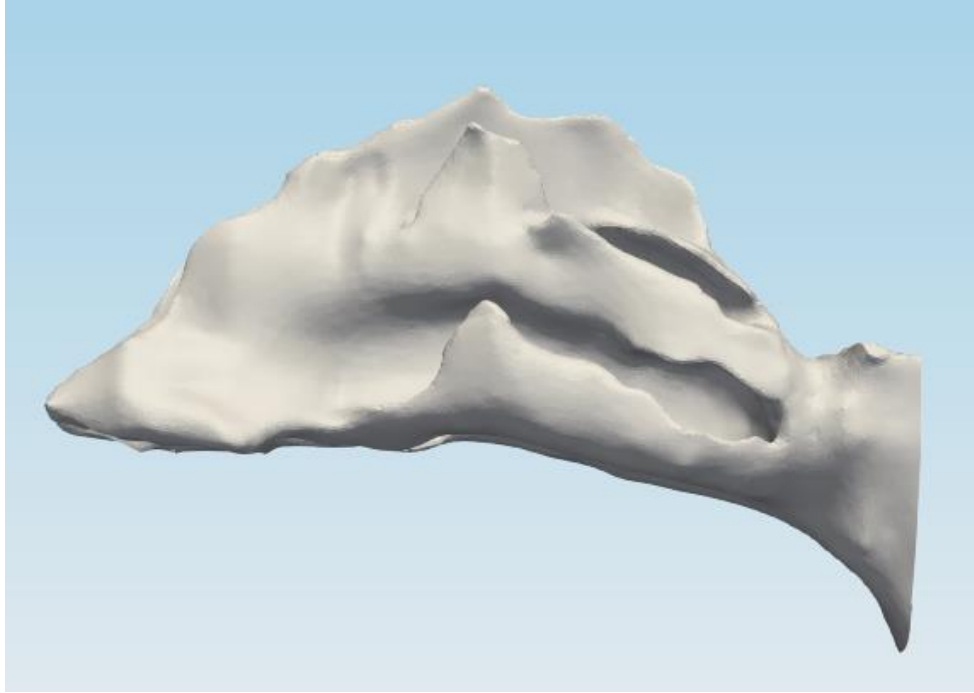


Figure 4. 18. Geometry G1.

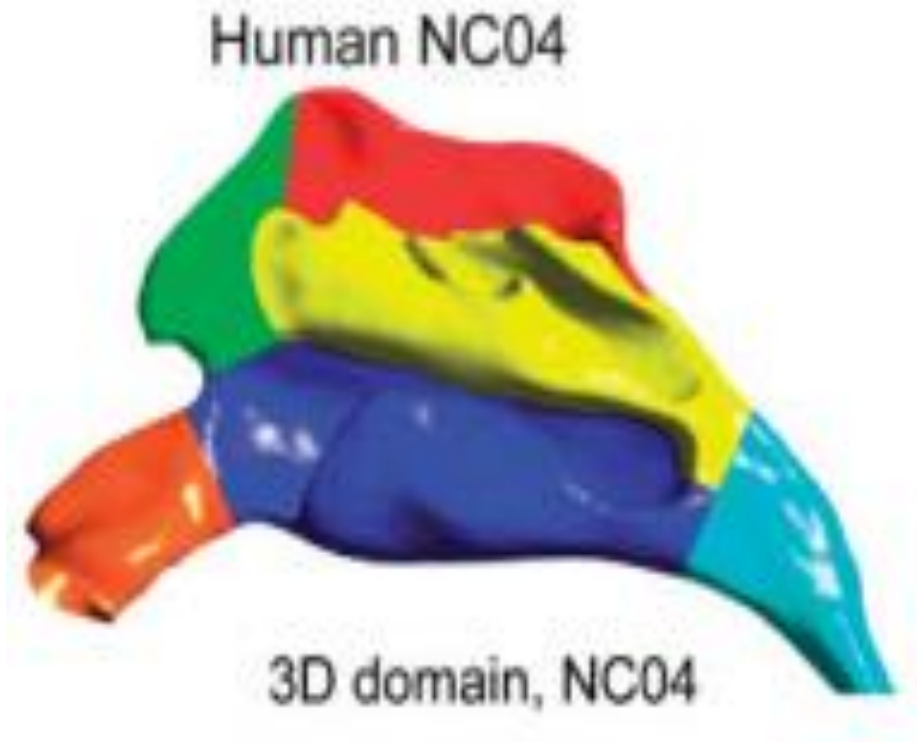


Figure 4. 19. Geometry G2.

4.18 and 4.19 highlight the contrasting shape-features of these two nasal configurations. G1 has a narrow vestibule region as compared to the G2 geometry. In addition, a distinctive feature separating the two geometries is that G1 has a concave cavity separating the vestibule region and the nasal passages while G2 is characterized by a smooth transition between the vestibule and the airway passage. Apart from that, both the geometries have well-defined upper, middle and lower passages.

Table 4. 4. Surface Area Comparison between G1 and G2 in MKS units.

	G1	G2
Nasal Cavity Surface Area	.0196563	.019882
Olfactory Region Surface Area	.00208761	.00194583
% of Olfactory to Nasal Surface Area	10.6	9.78

4.5.1. Airflow Field Results

Figures 4.20 and 4.21 show the sectional velocity contours for the in-house geometry, considering the sedentary breathing rates of 5lpm and 10lpm, respectively. It can be seen that both the flowrates have the same qualitative velocity contours. The air enters the nostrils in the vertical direction before accelerating in the vestibule region followed by deceleration inside the nasal cavity. Finally, due to the decrease in the size of the cross sectional area, the airflow accelerates into the nasopharynx.

An important characteristic of the flow inside the nasal cavity is that the superior meatus receives almost no airflow, which poses a hindrance in olfactory deposition. Hence, most of the flow passes through the middle and inferior meatus; hence, it is to be expected that major depositions occur in those areas.

Figure 4.22 provides the streamlines and the respective velocity magnitudes throughout the nasal cavity. Since the study involves multiple flow rates (5, 7 and 10lpm) and all the flowrates lie in the laminar regime, the magnitudes are normalized with the inlet velocities. Ambient air enters the nostrils in the upward direction and turns 90 degrees entering the middle and inferior meatus before finally turning 90 degrees again towards the nasopharynx. Air enters the nostrils at a high velocity before decelerating inside the meatuses. It can also be seen that the olfactory region receives almost no air which is a major problem when it pertains to olfactory drug targeting. This phenomenon can be deduced from Figure 4.23.

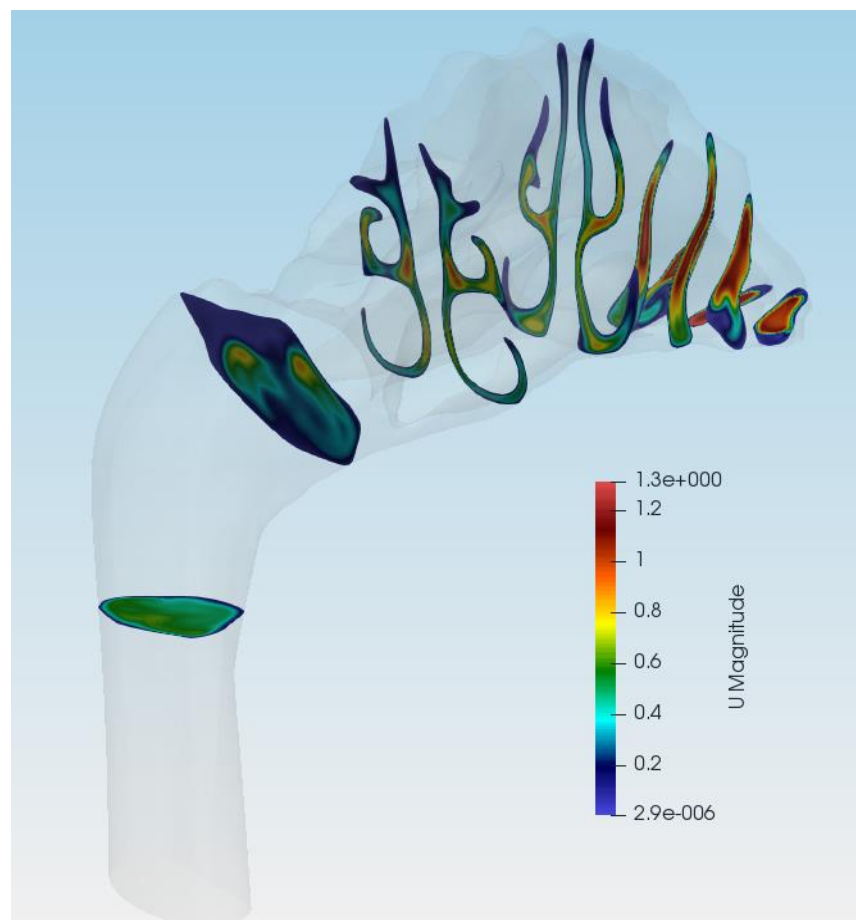


Figure 4. 20. Velocity contours along the nasal cavity for 5 lpm flowrate.

After traversing through the meatuses, fluid accelerates into the nasopharynx due to the reduction in the cross-sectional area. It is also noteworthy to see the formation of recirculation zone formed around the nostrils (Figure 4.24). The nostrils are wider than the inlet that creates a low-pressure region resulting in the formation of the recirculation zone. Hence, it is reasonable to anticipate deposition of particles around the nostril region.

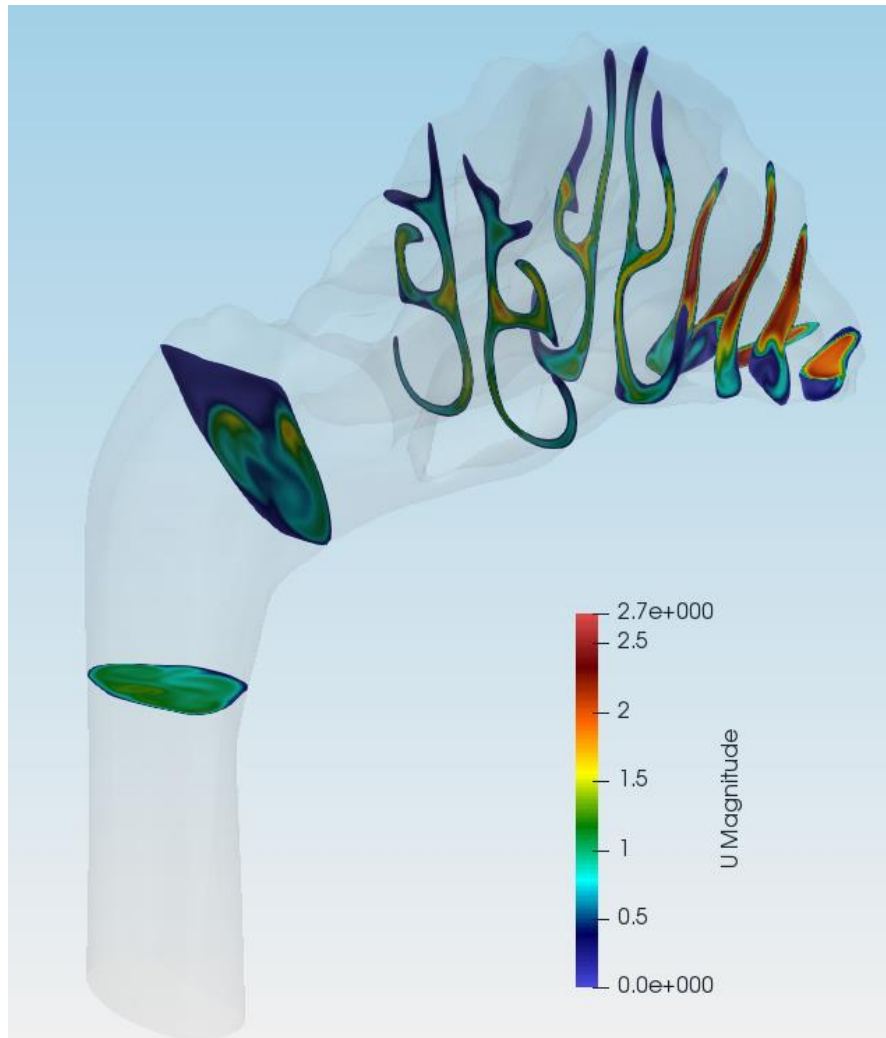


Figure 4. 21. Velocity contours along the nasal cavity for 10 lpm flowrate.

Another interesting phenomenon is the formation of Dean's vortices at the start of the nasopharynx (Figure 4.25). Due to the curved nature of the nasopharynx, an adverse pressure gradient is created resulting in a decrease in the velocity close to the convex wall and the opposite close to the concave

wall. In summary, most of the air inside the nasal cavity passes through the middle and inferior meatuses with very low velocities observed in the superior meatus closer to the olfactory region.

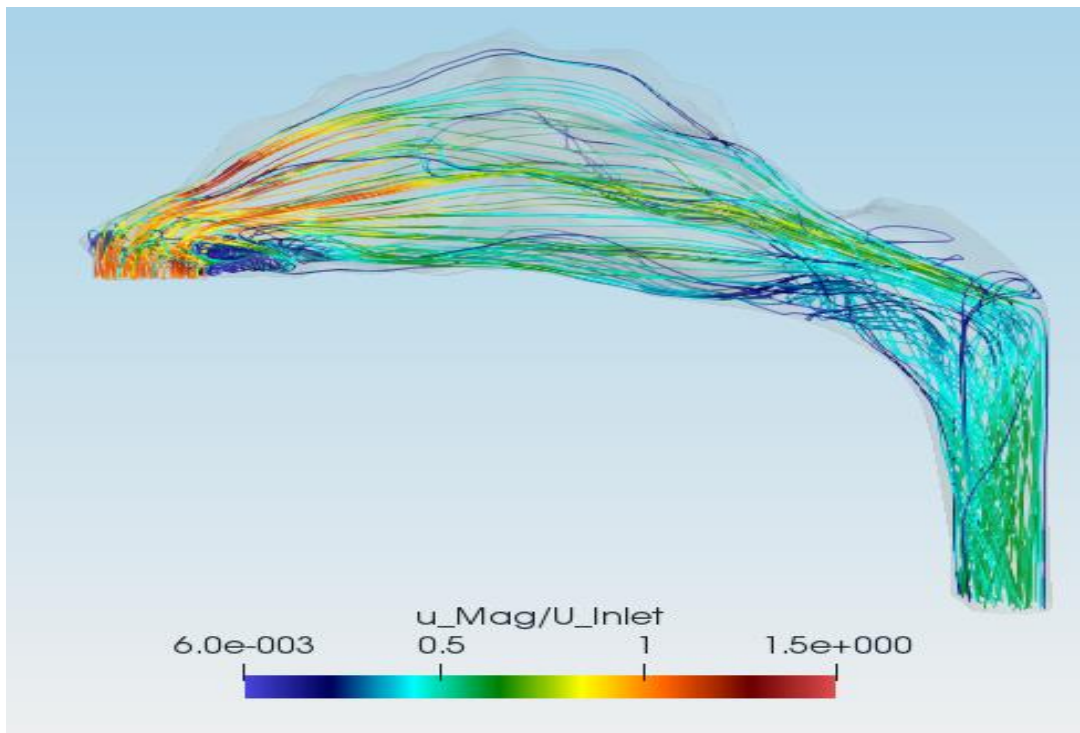


Figure 4. 22. Velocity streamlines across the nasal cavity.

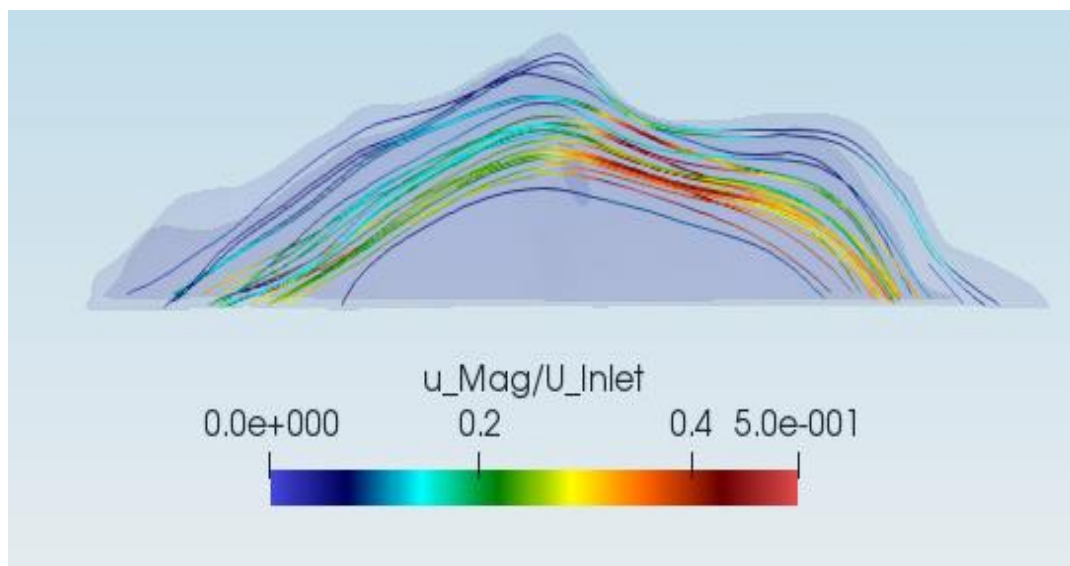


Figure 4. 23. Velocity streamlines in the olfactory region.

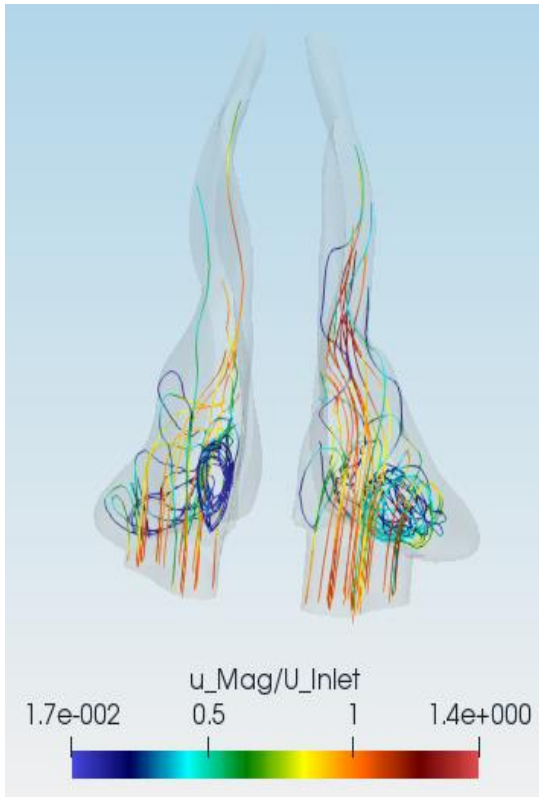


Figure 4. 24. Recirculation regions in the nostrils

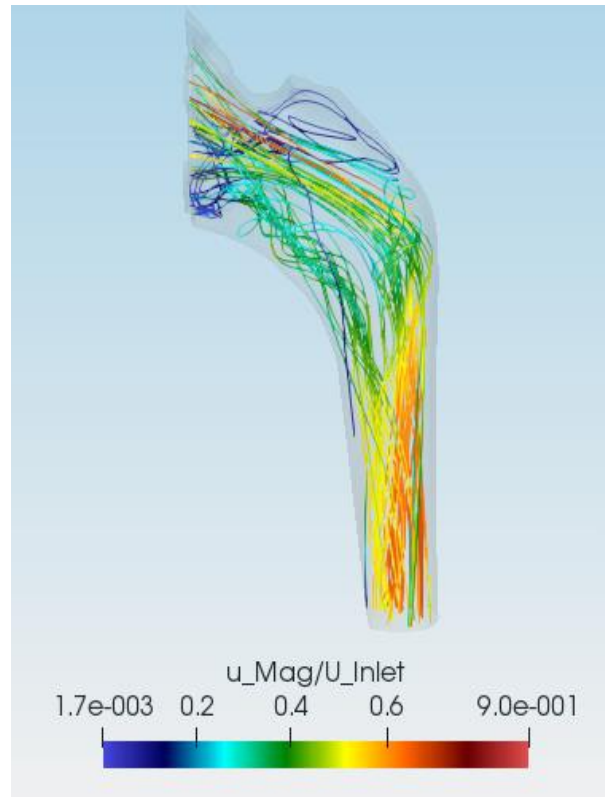


Figure 4. 25. Dean vortices in the nasopharynx

4.5.2. Particle Deposition Results

This section deals with nasal and olfactory depositions of micron-size particles, where the drag force and gravity are dominant, determining the trajectories of the particles. Clearly, deposition in the olfactory bulb is insufficient to be practical for drug delivery to the brain. Furthermore, micron-size particles are too large to pass through the Blood Brain Barrier (BBB), thereby reducing its effectiveness further. Thus, there is an urgent need to find ways to transport nanoparticles into the olfactory region. Unlike micron particles whose trajectories are mainly determined by inertia, nanoparticles are characterized by random behavior. Cunningham Drag and Brownian motion force are used to model nanoparticles in this study. These forces are explained in Section 2.4. Figure 4.26 shows the particle deposition pattern inside the nasal cavity for a steady flowrate of 10 lpm and a particle diameter of 1nm. Comparing this figure with Figure 4.11 clearly

shows the difference in fluid-particle dynamics between nanoparticles and micron particles. Micron-size particles show preferential deposition mainly in the vestibule region, thereby resulting in certain deposition “hotspots”. This is because the motion of micron particles is determined by the relatively high inertial forces which enable the particles to cross streamlines. For example in the case of 20 μm , the particle inertia is carried by the vertical airflow through the nostrils and deposited majorly in the vestibule region. On the other hand, nanoparticle deposition is dispersed throughout the nasal cavity. Due to the considerably lower inertia of nanoparticles, they are carried further into the nasal cavity rather than just depositing in the vestibule region by inertial impaction. Figure 4.27 shows the comparison of the total deposition efficiencies (TDE) between the results presented by Tian et al., 2019 and that of the present simulations. However, it is noteworthy to mention that the simulation showed a higher deposition efficiency for a specific particle diameter. This difference can be attributed to the difference in the shapes of the two nasal cavities. Most pronounced, the geometry used in Tian et al., 2019 has a sudden circular bend after the nasal vestibule (see Figure 4.19).



Figure 4. 26. Deposition pattern for 10 lpm flowrate and 1nm diameter particle.

Due to this the velocity streamlines are unable to immediately conform to the geometry surface. Consequently low pressure and a region of recirculation are created around the circular bend. As a result, the olfactory region receives less air, i.e., much lower flow to the olfactory region, thereby restricting nanoparticles to reach the olfactory epithelium. On the other hand the nasal geometry used in the simulation has a smooth transition from the vestibule to the meatuses. This enables a higher concentration of streamlines through the olfactory region and as a result, more deposition was observed in the simulation geometry. In addition, a higher flowrate results in lower total deposition. This can be attributed to the fact that unlike micron particles, nanoparticles do not have enough inertia to cross streamlines and they are easily carried away by the flow. At higher flowrates, more particles exit through the nasopharynx.

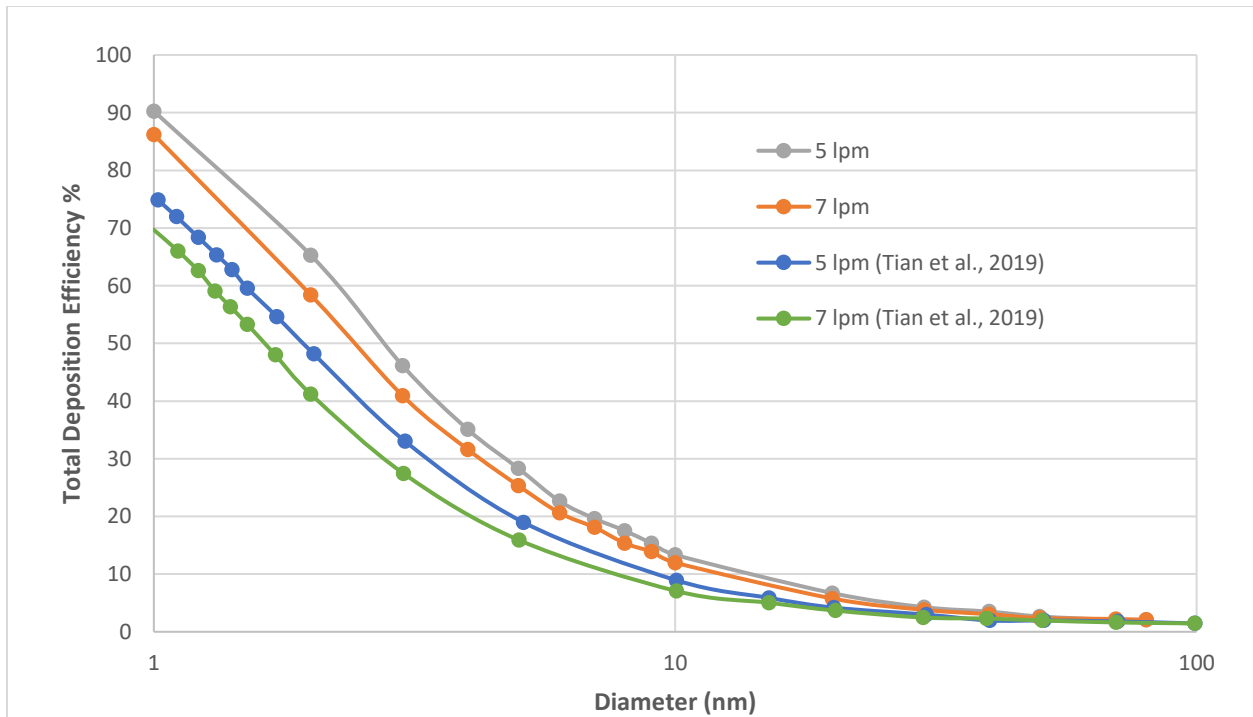


Figure 4. 27. TDE comparisons for 5 lpm and 7 lpm flowrates.

While considering Lagrangian particle tracking simulations, the number of particles (NOP) injected can skew the deposition efficiency values. Hence, to validate the force formulations and

the methodology used in the current study, it is essential to show that the deposition results are independent of the number of particles injected. Figure 4.28 shows the comparison of total deposition results inside the nasal cavity for a sedentary 10 lpm breathing rate with two different values of the number of particles injected. The respective graphs are almost coincident, indicating that the number of particles injected is not an essential parameter to consider while conducting the particle-tracking simulations. The main goal of this study is to find ways towards enhanced NP-deposition in the olfactory bulb.

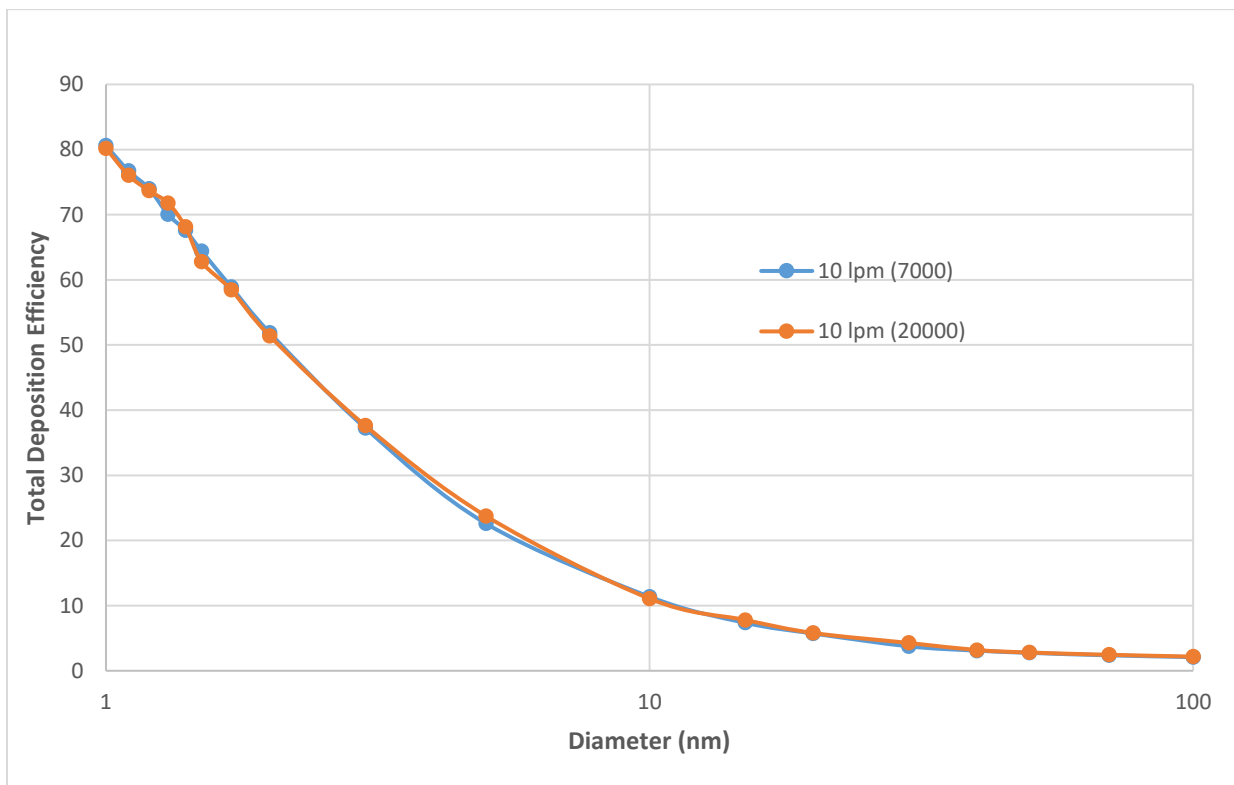


Figure 4. 28. NOP-independence study for Total Deposition (10 lpm).

Figure 4.29 shows the dependence of the olfactory deposition efficiency (ODE) with particle diameter (1-100 nm) for the sedentary breathing rates of 5 lpm and 7 lpm. It also shows the comparison between the results presented in this study and the results presented in (69). It can be seen that the olfactory deposition does not follow the same trend as that of the total nasal

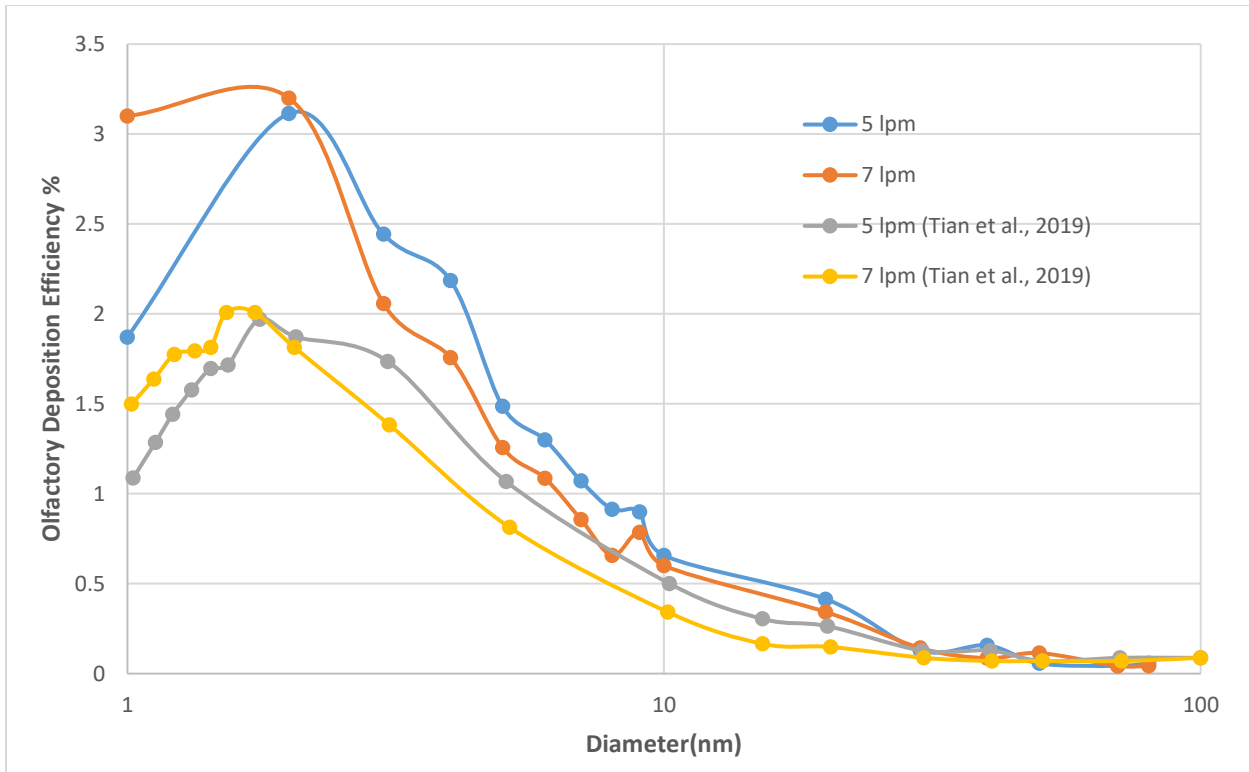


Figure 4. 29. ODE comparison for 5 lpm and 7 lpm flowrates.

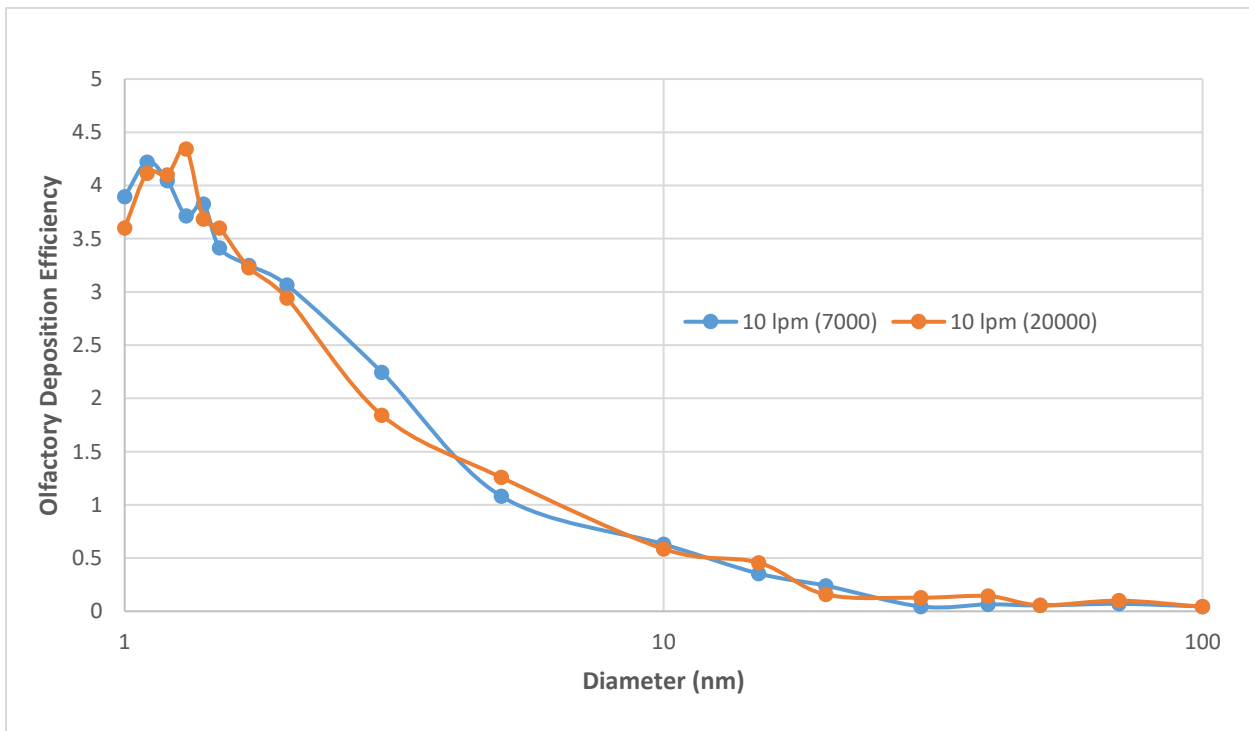


Figure 4. 30. NOP Independent study for Olfactory Deposition (10 lpm).

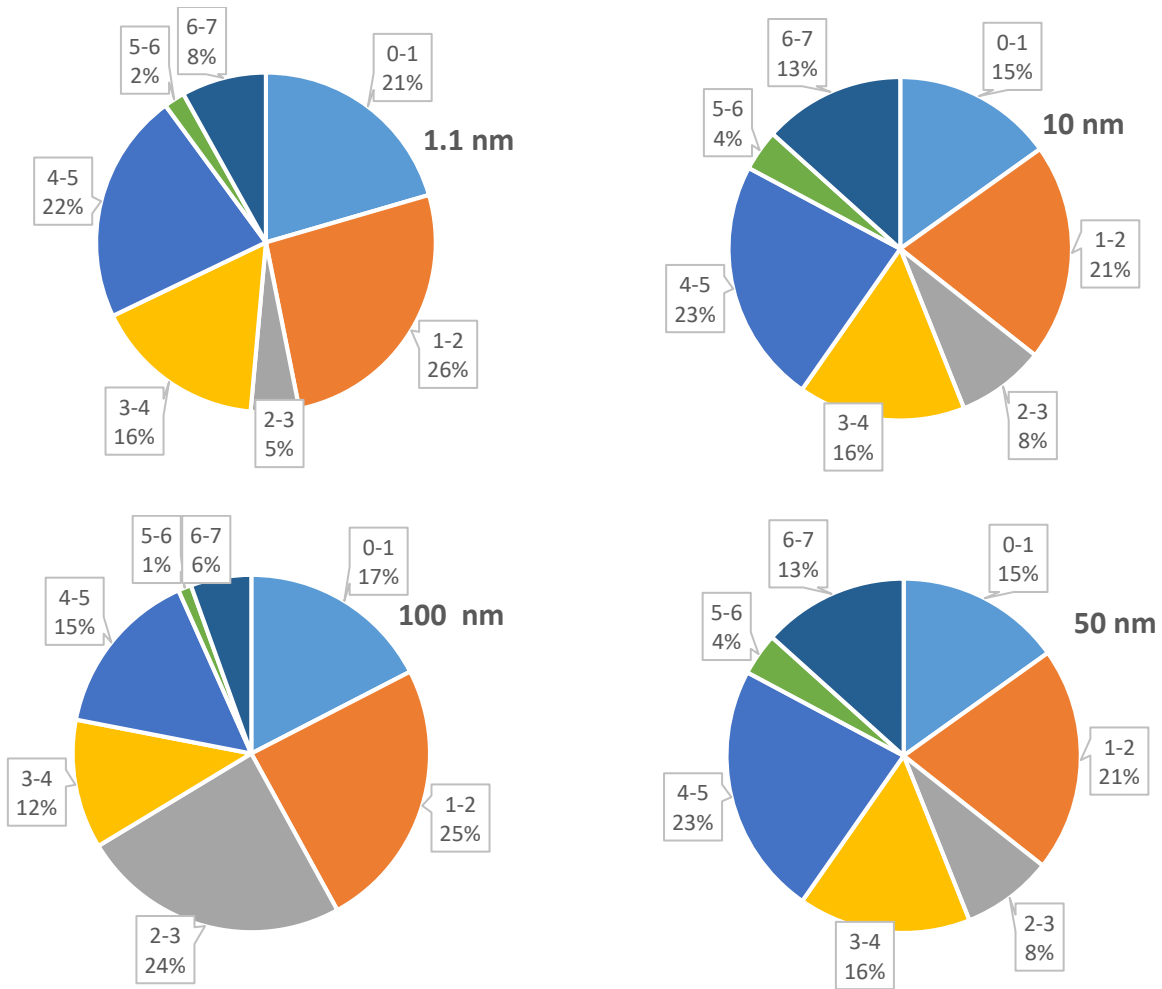


Figure 4. 31. Sectional Deposition for 1.1 nm, 10nm, 50 nm and 100 nm (clockwise from the bottom) at a flowrate of 10 lpm.

deposition. There is a local maximum observed for the 2nm particle diameter. The unusual peak can be explained as follows. 1 nm particles are highly diffusive in nature and their deposition is completely dependent on the brownian dispersion force. 2 nm particles are slightly less diffusive and are more susceptible to be carried away by the streamlines and hence more particles reach the olfactory region. Most 1 nm particles on the other hand don't reach the olfactory region due to either being deposited in the vestibule region or passing through the middle passage. The subsequent decrease in olfactory deposition with increase in the size of nanoparticles can be

reasoned due to the less diffusive nature of the particles. So even if the particles travel to the passage of the olfactory region, their low diffusivity inhibits them from being deposited. The maximum olfactory deposition for 5 lpm and 7 lpm using the simulation is 3.1% and 3.2%, respectively, which confirms published NP-deposition data.

Figure 4.30 shows that the olfactory results are independent of the number of particles injected. It is also noteworthy to compare the sectional deposition for nanoparticles (Figure 4.31) to that of micron particles (Figure 4.12 and Figure 4.13). While micron-size particles generate “particle hotspots”, nanoparticles are distributed almost uniformly throughout the nasal cavity and nasopharynx. This is due to the impact of Brownian motion that produces random, ie, diffusional, changes in the trajectories of the nanoparticles. Furthermore, the size of the nanoparticles has a miniscule effect on sectional deposition. This indicates that local deposition for nanoparticles is greatly governed by the shape of the nasal geometry. The shape of the nasal geometry determines the flow distribution which subsequently is the driving force along with the Brownian force in particle deposition along the different sections of the geometry.

CHAPTER 5. PARTICLE RELEASE MAP FOR OLFACTORY DRUG TARGETING

5.1 Introduction

Targeted drug delivery is based on the idea that a specific diseased organ site is targeted for drug delivery to produce a significant therapeutic efficiency. Drug administration can take place through the mouth in the form of pills, through injection using a syringe (known as the parenteral route), through the nasal route in the form of inhalers and so on and so forth. Usually the parenteral and the oral routes result in the drug formulations reaching throughout the body via the bloodstream. While most drugs are innocuous, some drug formulations might be toxic to certain parts of the body and hence the need for targeted drug delivery. Furthermore targeted drug delivery increases the efficiency of drug deposition on the targeted site significantly. Olfactory drug targeting through the nasal route has gained a lot of priority in recent years. Since only nanoparticles are small enough to successfully cross the Blood Brain Barrier (BBB), the progress in the field of nanotechnology has further made this approach more feasible. Furthermore, recent advances in nebulizer technologies have shown to produce aerosol particles and droplets in the nanoparticle range (85-87). The aforementioned technologies in conjunction pave the way for efficient drug targeting in the future. Results from Chapter 4 show that the maximum olfactory deposition efficiency observed was 3-4 %. This deposition is not enough to be of clinical significance. Hence the need for further research into improving the deposition. The approach for olfactory drug deposition in Chapter 4 involved injecting particles randomly throughout the nostrils and checking the drug deposition efficiency. It may be beneficial to utilize the Particle Release Map (PRM) (88, 89) approach to decide the optimal injection area that results in maximum olfactory deposition efficiency. The PRM approach involves injecting particles uniformly throughout the nostrils and studying the regional deposition inside the nasal cavity. These

deposited particles are backtracked to their injection position and marked. Each area of deposition is marked differently in the PRM. This methodology gives the position of the injection that would majorly transport the particles to the specific region.

5.2 Methodology

In this study, Particle Release Maps (PRMs) are generated for nanoparticles and micron sized particles under different flow conditions. The particle deposition is studied for low (5 lpm) and medium (20 lpm). OpenFOAM generates an extensive data file showing the particle positions, their ID's, deposited particles and so on and so forth. This information is essential for creating the Particle Release Map. The PRM is constructed via the following steps:-

1. Conducted a `simpleFoam` simulation to get a steady state flow field for a particular flowrate.
2. Using the flow field, conducted a CF-PD simulation using `icoUncoupledKinematicParcelFoam` for lagrangian tracking of individual particles and measuring the regional and total deposition efficiency. In this simulation the particles are uniformly distributed throughout the nostrils and all of them are released initially all at once.
3. Tracked all of these particles until all of them are either deposited or escaped.
4. The initial and final position of the particles are then compared using the particle ID to determine which particles are deposited in a specific region in the nasal cavity. This was done using a Matlab script.
5. Marking each specific region deposited particles with a separate marker on the initial injection position file gives the full-fledged particle release map.

The purpose of the PRM is to determine the optimal injection position for maximum regional deposition to the specific area. In this study, once the PRM is constructed, another simulation is conducted by injecting similar amount of particles from the position on the PRM that is suitable for olfactory drug targeting. This is done so as to

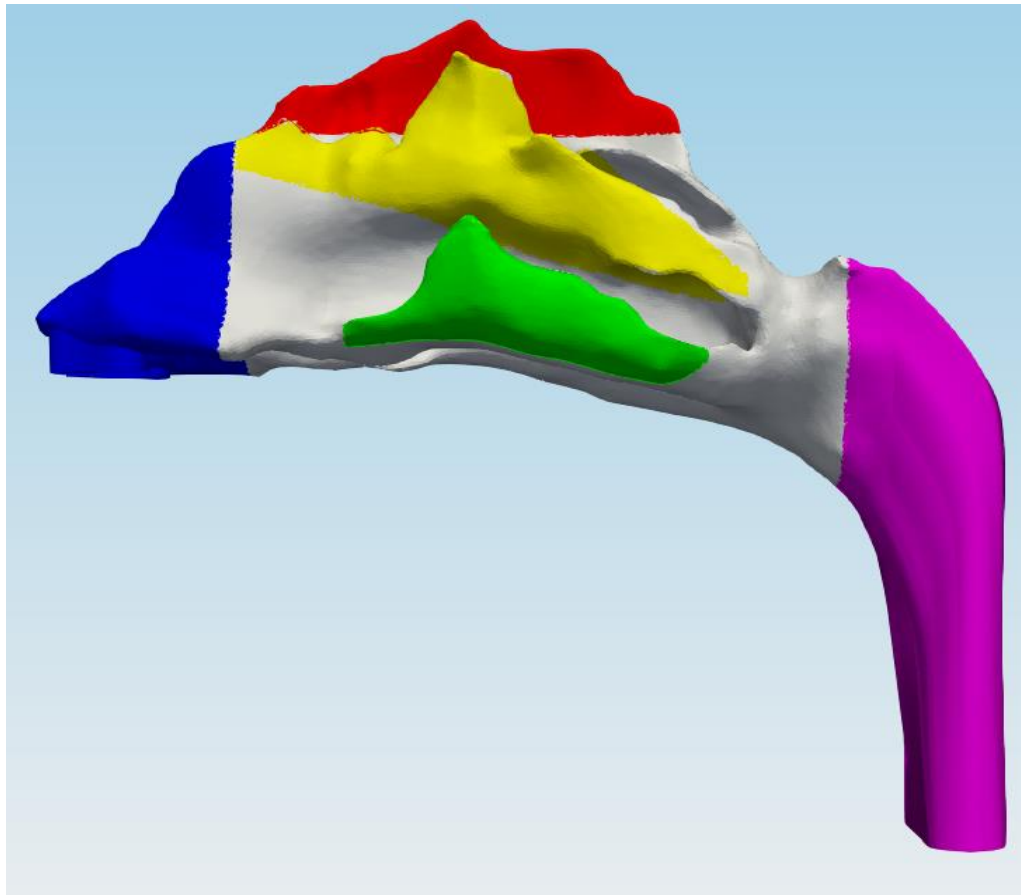


Figure 5. 1. Nasal geometry with the specific regions that will be represented in the Particle Release Map

Table 5. 1. Legend correlating the color to the specific region.

Colour	Region
Blue	Anterior
Red	Olfactory
Yellow	Middle Meatus
Green	Inferior Meatus
Magenta	Nasopharynx

establish the effectiveness of the PRM approach. For each flowrate, both micron-sized particles (2 μm , 5 μm and 10 μm) and nanoparticles (1 nm, 10 nm and 100 nm) were considered. Figure 5.1 shows the nasal geometry with the different parts highlighted in specific color. These are the regions that will be represented by the particle release map. Table 5.1 represents the legend correlating the highlighted colors with the specific regions.

5.3. Results and Discussion

5.3.1. Micron-size Particles

The study is done for different flowrates and multiple particle diameters but it is easier to combine the two parameters for analyzing the particle deposition for micron particles where inertia is dominant. The parameter is called the Impaction Parameter (IP) which is given by:

$$IP = d^2Q$$

Where d is the particle diameter and Q is the volumetric flowrate. These parameters represent the cumulative effect of the size of the particle and the fluid inertia. Figures 5.2.1 – 5.6.1 show the Particle Release Maps for various impaction parameter values. The specific color on the PRM denote the region of the nasal geometry where the particles deposited as per Table 5.1. The particle release maps clearly show the preferential sites of injection for olfactory deposition. These are located at the narrower end of the nostrils. Using these PRMs, separate computer simulations are conducted by injecting particles to target the olfactory region. Figures 5.2.2-5.6.2 show the comparison of deposition efficiencies between normal and targeted injection. As the impaction parameter increases, the total nasal deposition efficiency increases for normal injection. This is primarily because of inertial impaction and most of the particles deposit in the vestibule region. However, the trend for olfactory deposition is the opposite. This is because low inertia results in

more particles entering the nasal passage rather than getting stuck in the vestibule region. For the same reason, nasopharynx deposition follows the same trend as that of olfactory deposition.

The olfactory deposition observed from normal injection is extremely low ($<0.05\%$). To improve the deposition efficiency, a circular injector-nozzle of diameter 0.5mm was employed. The figures indicate that targeted injection greatly increases the olfactory deposition efficiencies. The maximum nasal and olfactory depositions observed are 54% and 11 % respectively in Figure 5.5.2. Figures 5.7 and 5.8 illustrate the effect of the targeted injection on the deposition pattern inside the nasal cavity. The phenomenon of targeted injection directs the micron particles to the olfactory region. However, because of their ability to cross streamlines, a major fraction of these particles deposit just before the olfactory region and consequently a maximum deposition of only 11 % occurred. As shown in Figure 5.8, the olfactory as well as nasal deposition achieves a maximum for an IP of 8333.333, caused by the gravitational effect. The higher impaction number generally signifies higher particle diameters, amplified by the dependence on the square of the particle diameter. So higher impaction parameter values with targeted injection results in pushing particles upwards from the nostrils into the olfactory region. However, as the particle diameter increases, the effect of gravity becomes more significant and the particles that were being pushed upwards start going due to the middle and lower portion of the nasal passages. This phenomenon is called the “sedimentation effect”. This can be observed by comparing Figures 5.8 and 5.9. Through the comparison it can be observed that the higher impaction parameter yields lower nasal and olfactory depositions.

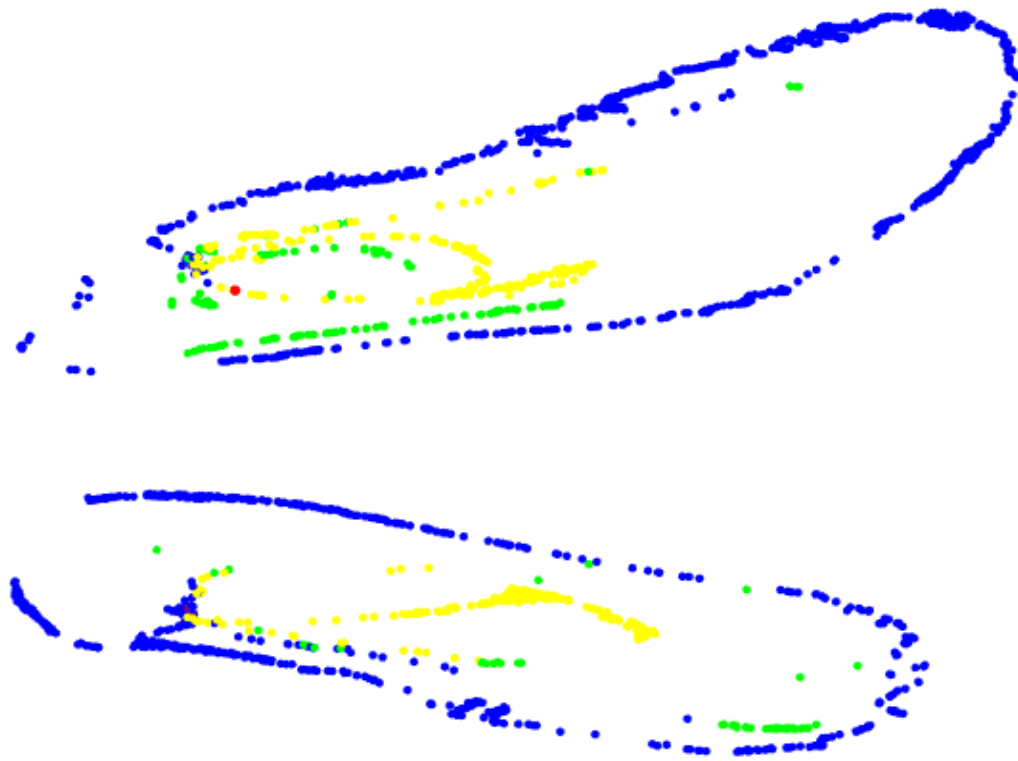


Figure 5. 2.1. PRM for an impaction parameter of $333.333 \mu\text{m}^2 \text{cm}^3 \text{s}^{-1}$.

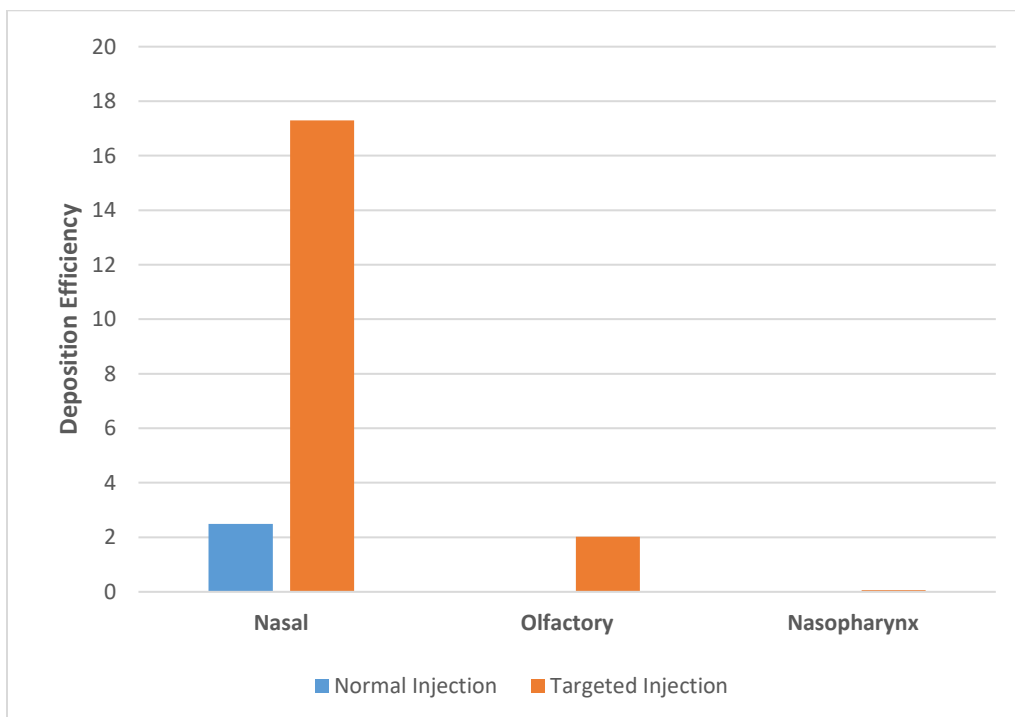


Figure 5.2.2. Deposition efficiency comparison between normal and targeted injection.

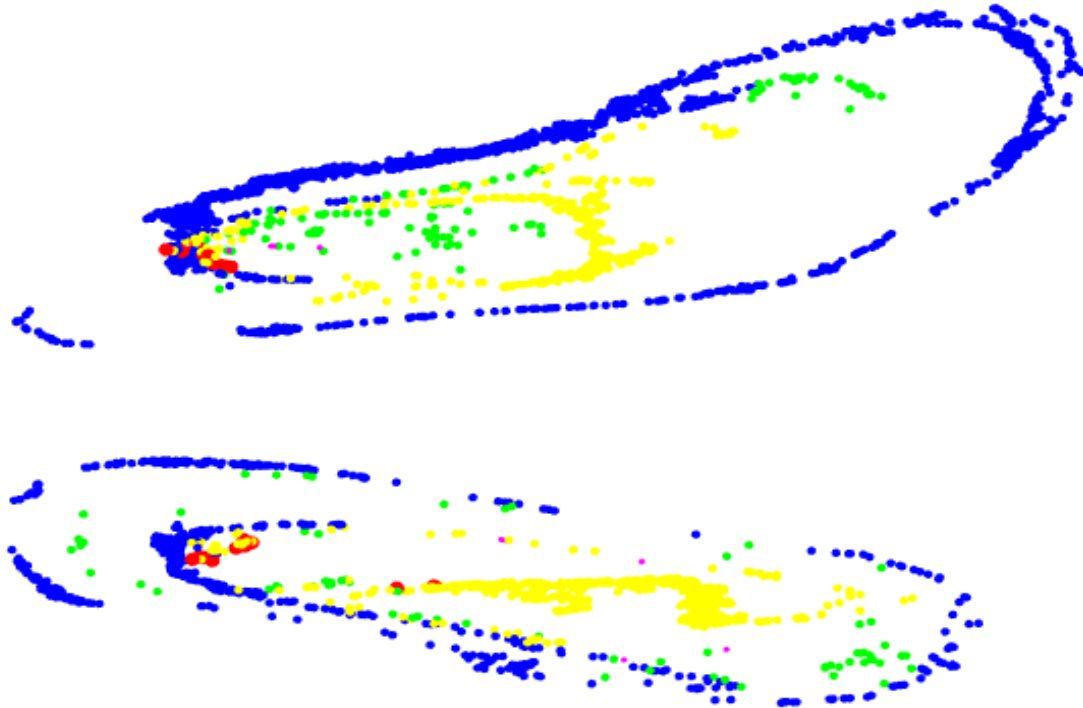


Figure 5. 3.1. PRM for an impaction parameter of $1333.333 \mu\text{m}^2\text{cm}^3\text{s}^{-1}$.

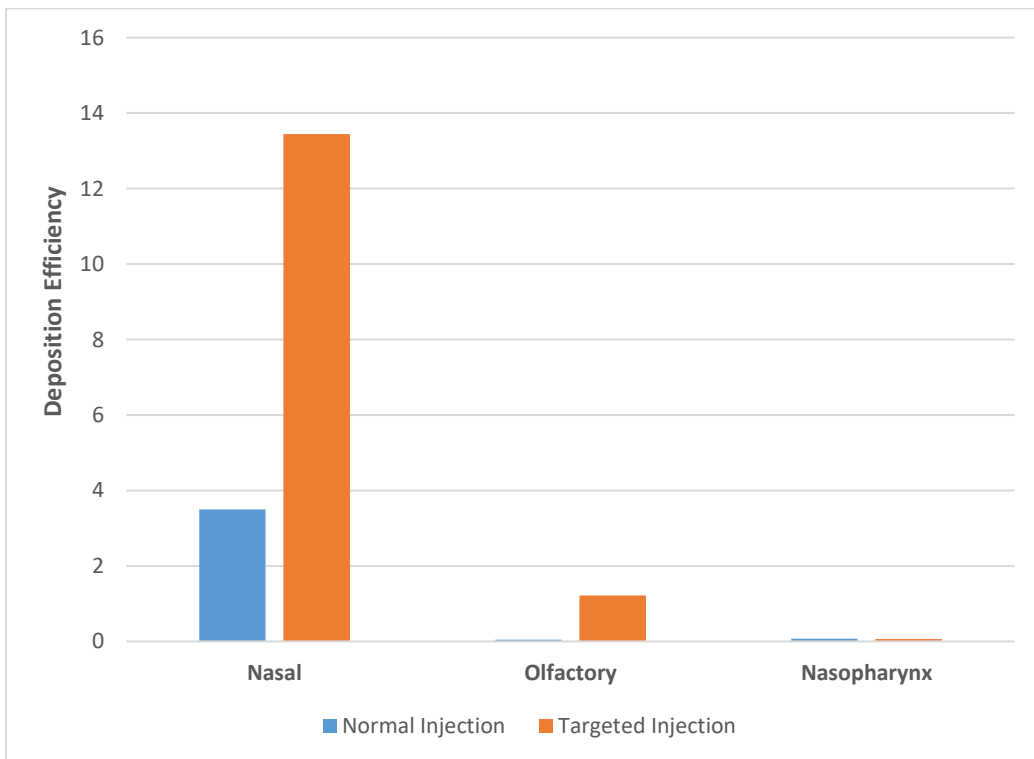


Figure 5.3.2. Deposition efficiency comparison between normal and targeted injection.

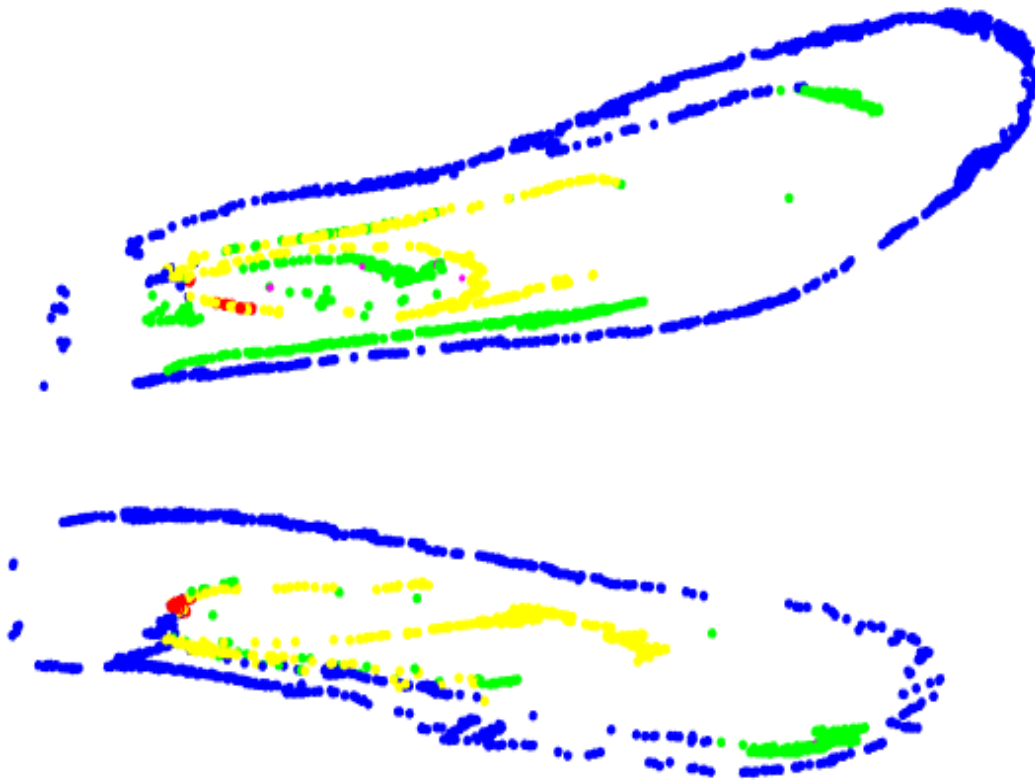


Figure 5. 4.1. PRM for an impactation parameter of $2083.333 \mu\text{m}^2\text{cm}^3\text{s}^{-1}$.

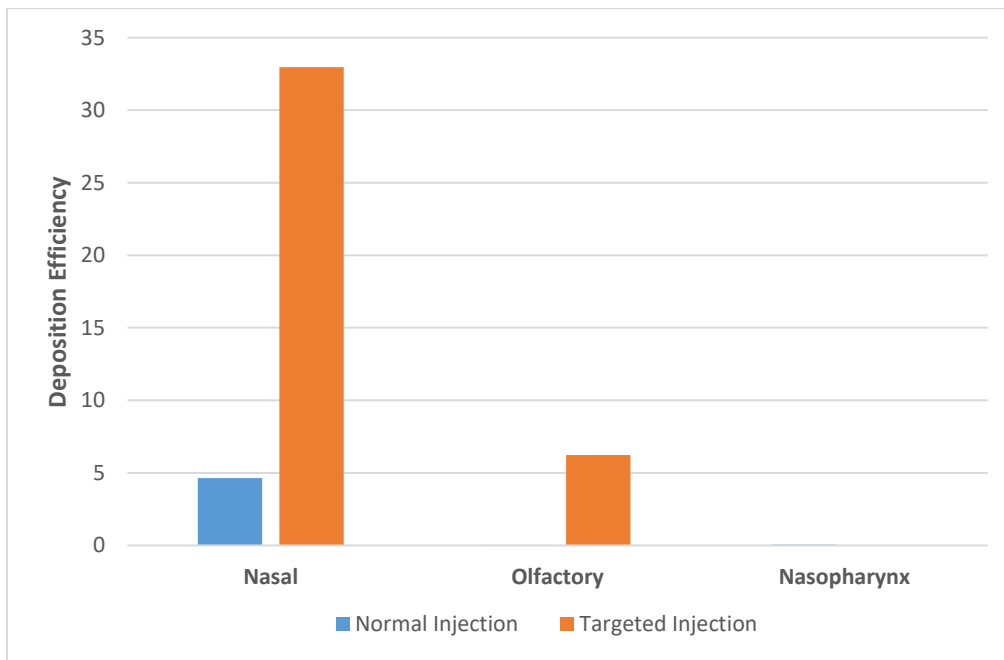


Figure 5.4.2. Deposition efficiency comparison between normal and targeted injection.

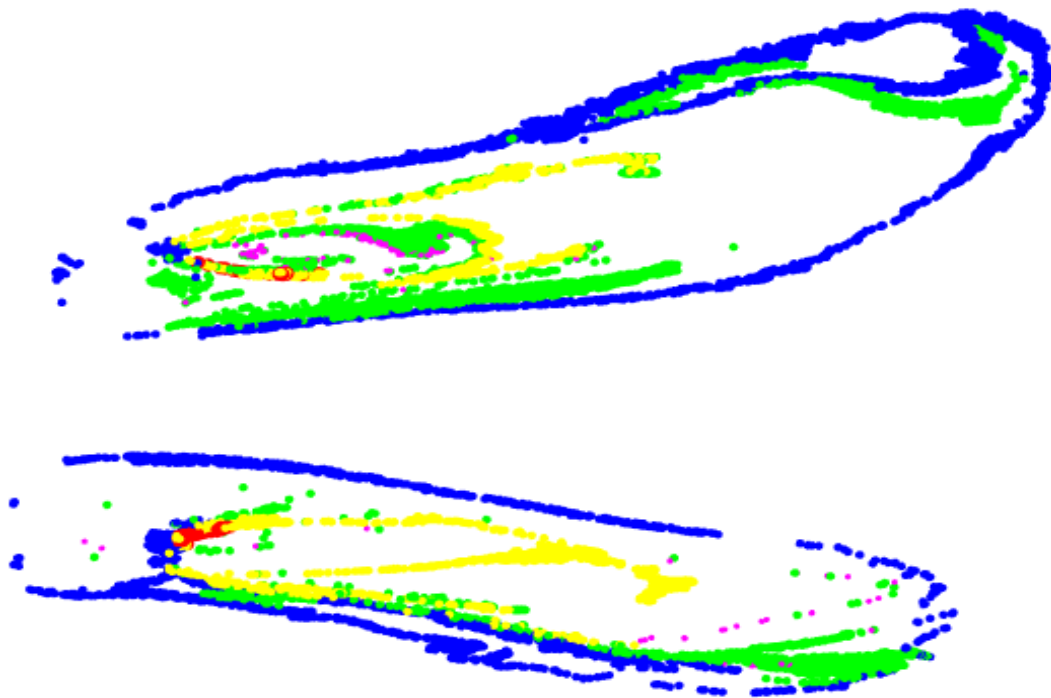


Figure 5. 5.1. PRM for an impaction parameter of $8333.3333 \mu\text{m}^2\text{cm}^3\text{s}^{-1}$.

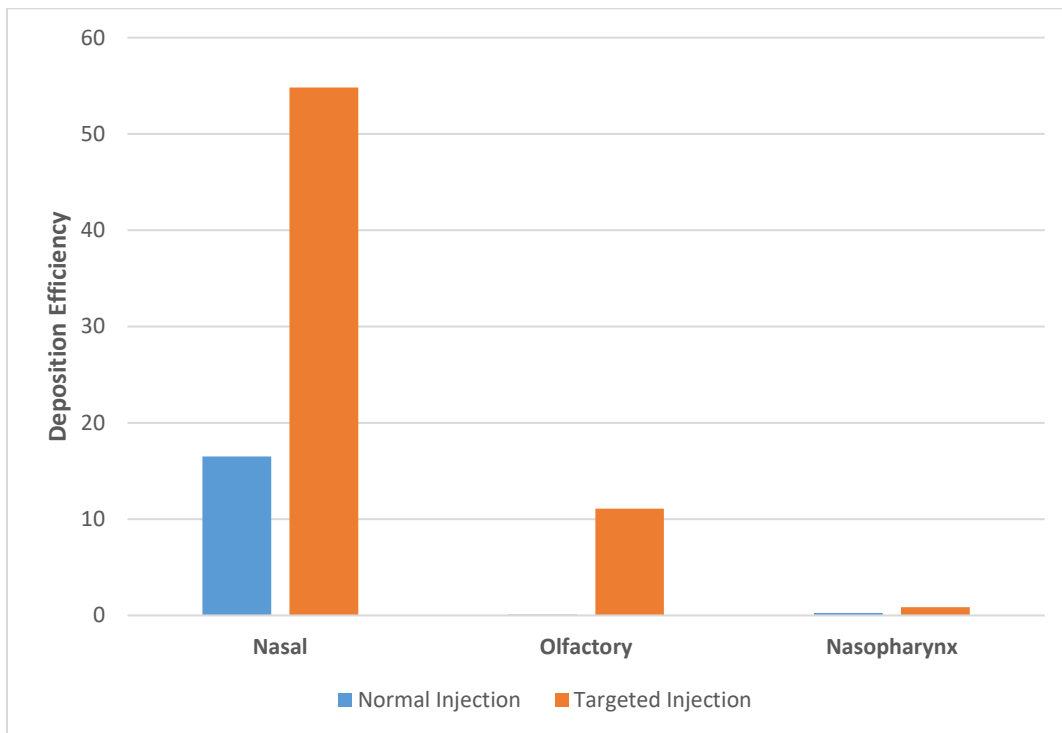


Figure 5.5.2. Deposition efficiency comparison between normal and targeted injection.

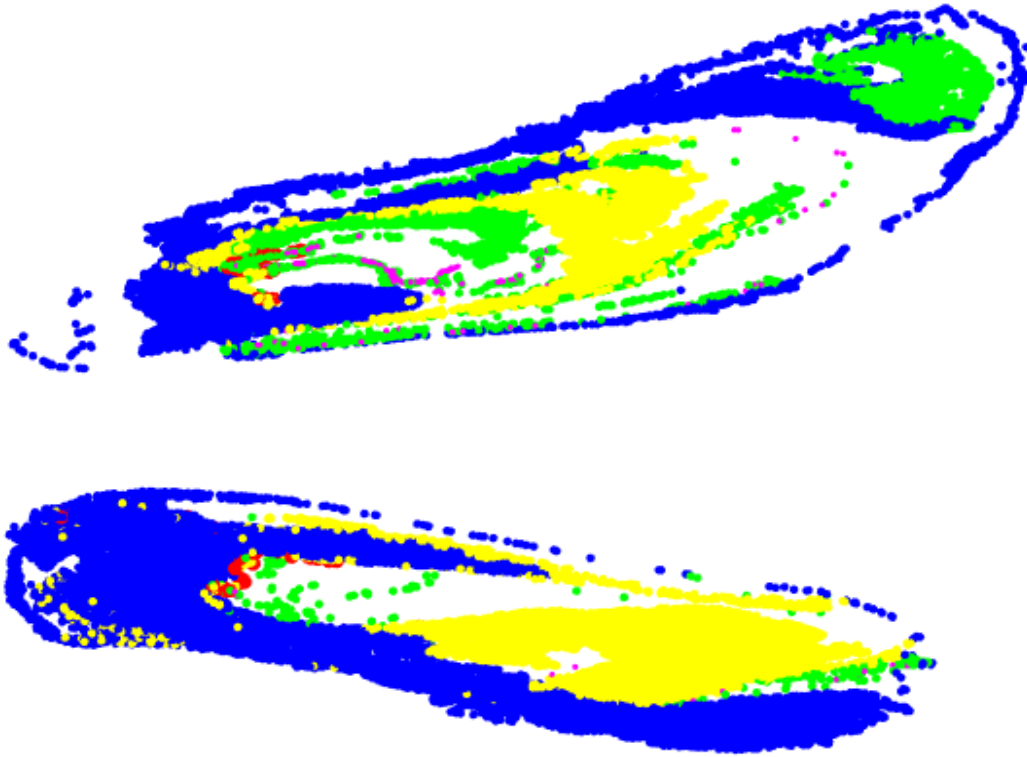


Figure 5. 6.1. PRM for an impaction parameter of $33333.3333 \mu\text{m}^2\text{cm}^3\text{s}^{-1}$.

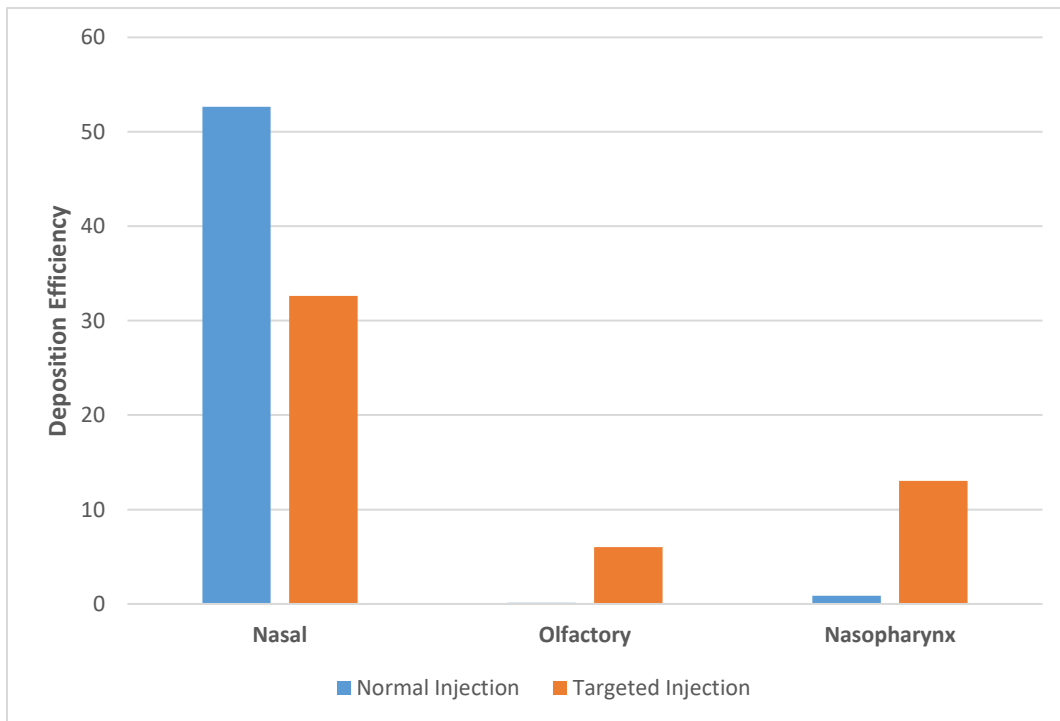


Figure 5.6.2. Deposition efficiency comparison between normal and targeted injection.

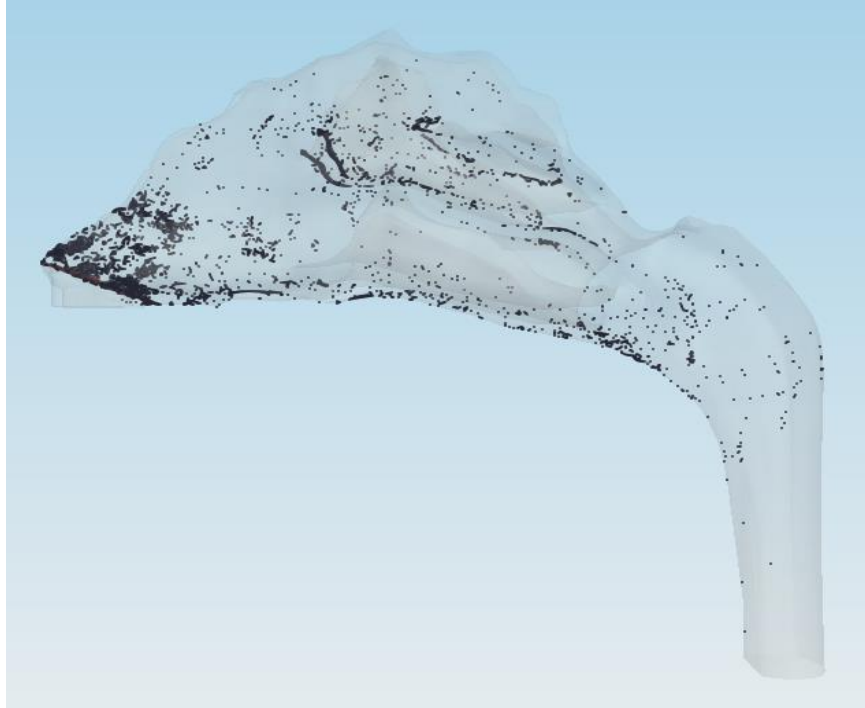


Figure 5. 7. Deposition Pattern due to normal injection
for an IP of $8333.3333 \mu\text{m}^2\text{cm}^3\text{s}^{-1}$.

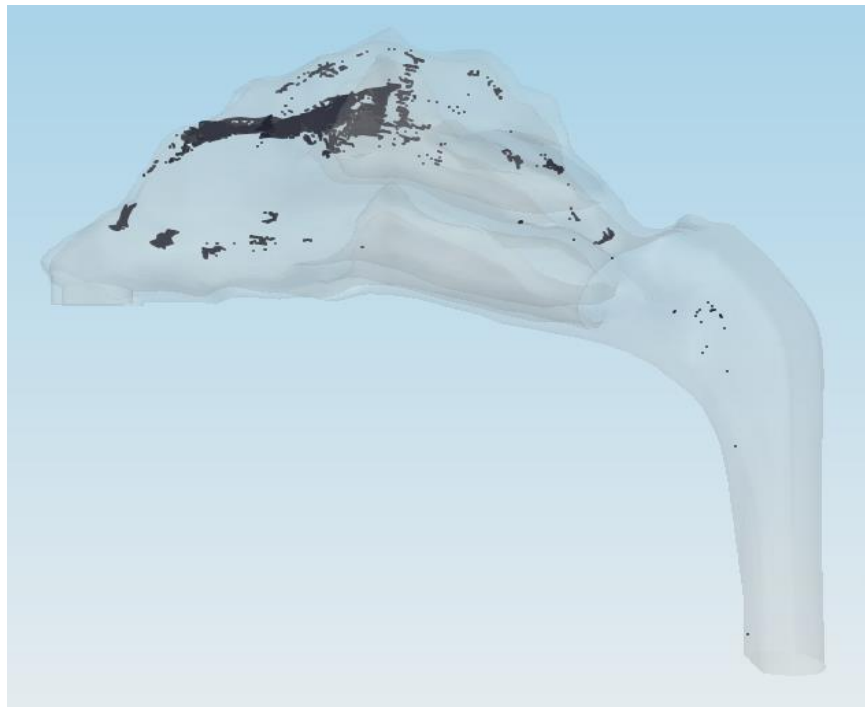


Figure 5. 8. Deposition Pattern due to targeted injection
for an IP of $8333.3333 \mu\text{m}^2\text{cm}^3\text{s}^{-1}$.

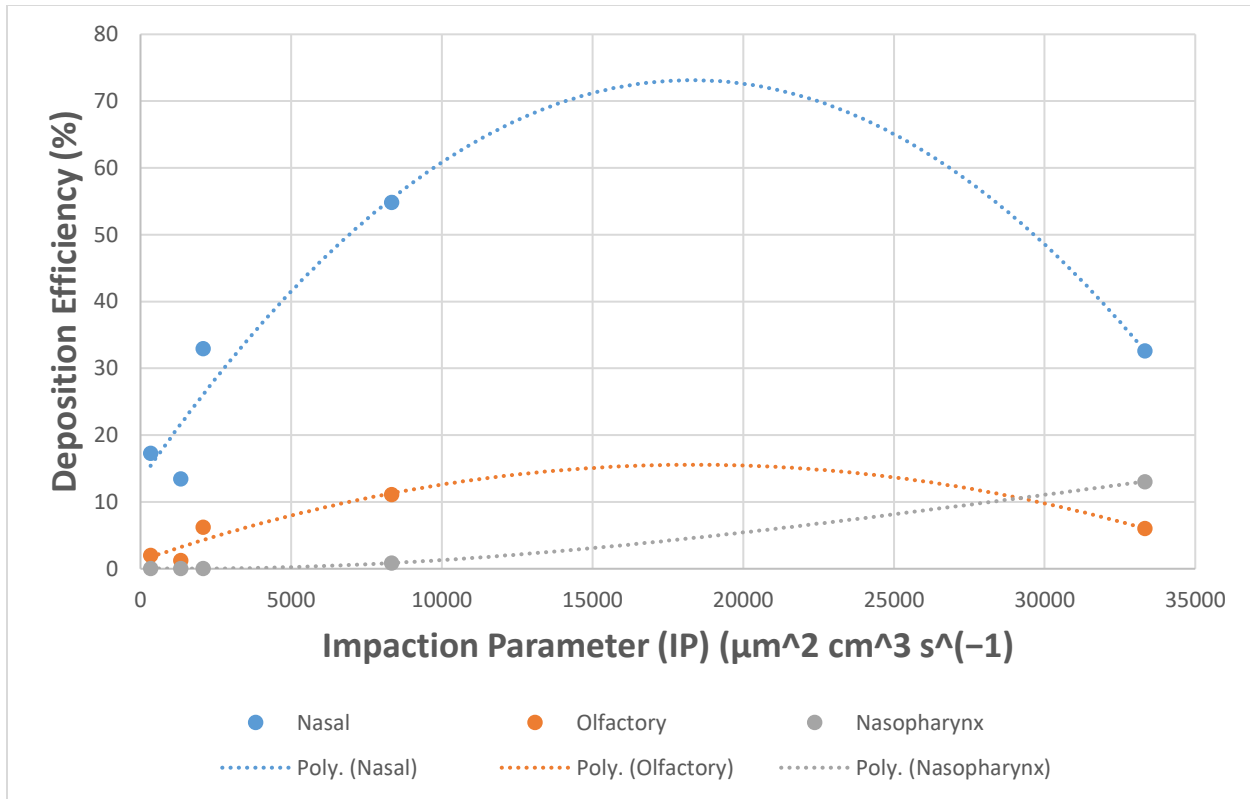


Figure 5. 9. Deposition Pattern due to targeted injection.

Although the targeting directs the particles towards the olfactory region, gravity counteracts this effect, thereby pushing the particles towards the lower and middle passages, as evident with the nasopharynx deposition in Figure 5.10. The effect of gravity pushes particles through the middle passages and subsequently into local Dean vortices in the nasopharynx which results in higher nasopharynx depositions.

This section highlighted the fluid-particle dynamics and their effect on olfactory deposition. It is shown that targeted injection, employing the Particle Release Map (PRM) approach, does indeed increase olfactory deposition. Also the olfactory deposition increases with larger impaction parameter values - up to a point and subsequently decreases due to gravity. For the flowrates and the particle diameters analyzed in this study, the combination of 20 lpm flowrate

and 5 μm particle diameter ($\text{IP} = 8333.3333 \mu\text{m}^2\text{cm}^3\text{s}^{-1}$) yields the maximum olfactory deposition of 11 %.

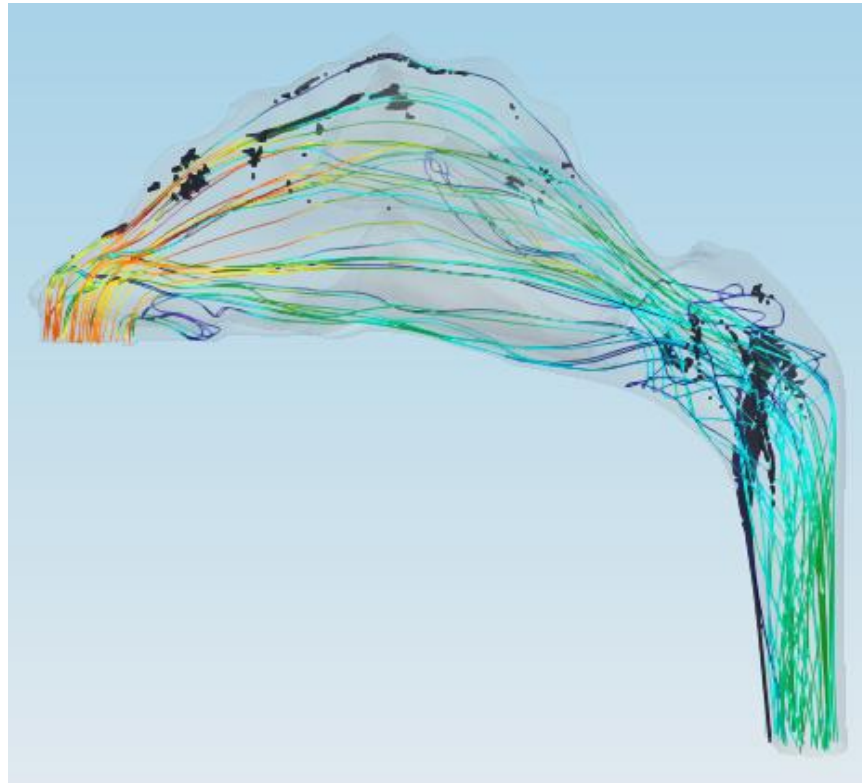


Figure 5. 10. Deposition Pattern due to targeted injection
for an IP of $33333.3333 \mu\text{m}^2\text{cm}^3\text{s}^{-1}$.

5.3.2. Nanoparticles

The previous section shows the influence of targeted injection of micron-size particles. This section is concerned with nanoparticles for targeted drug delivery to the olfactory region. The forces involved are highlighted in Section 2.4. It is understood that unlike micron particles, nanoparticles do not generally cross streamlines due to inertia. The particle dynamics is governed by random Brownian forces. Figures 5.11-5.13 show the particle release map and the particle deposition pattern for a flowrate of 5lpm with 1nm, 10nm and 100nm particles, respectively.

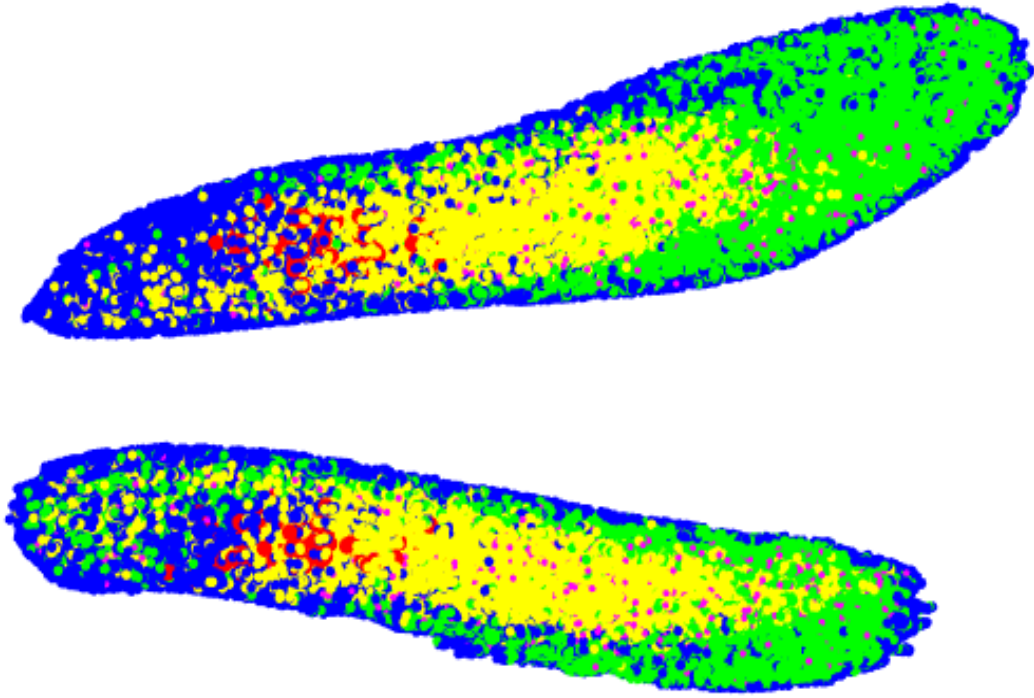


Figure 5. 11.1. PRM of 1 nm particles for the flowrate of 5 lpm.

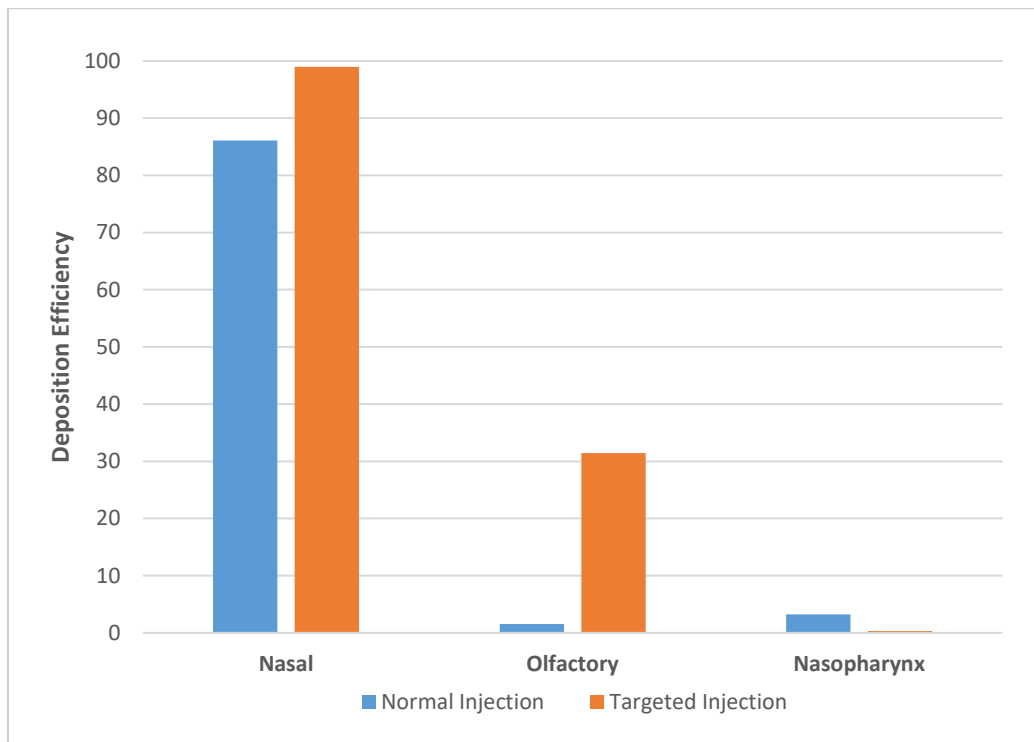


Figure 5.11.2. Deposition efficiency comparison between normal and targeted injection.

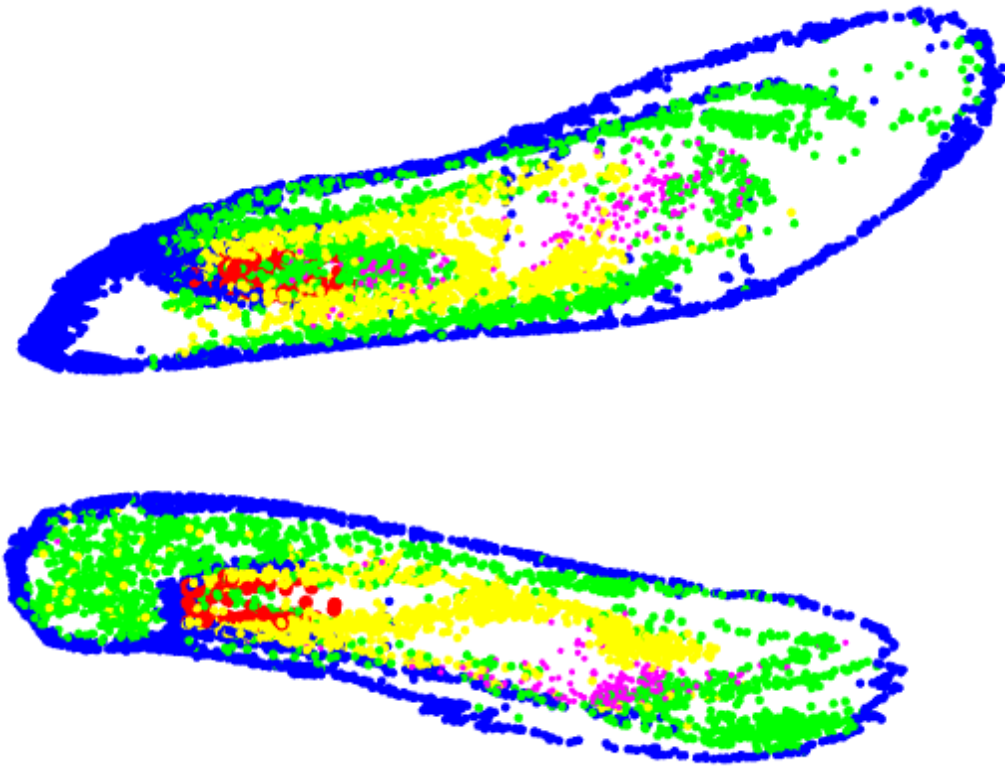


Figure 5. 12.1. PRM of 10 nm particles for the flowrate of 5 lpm.

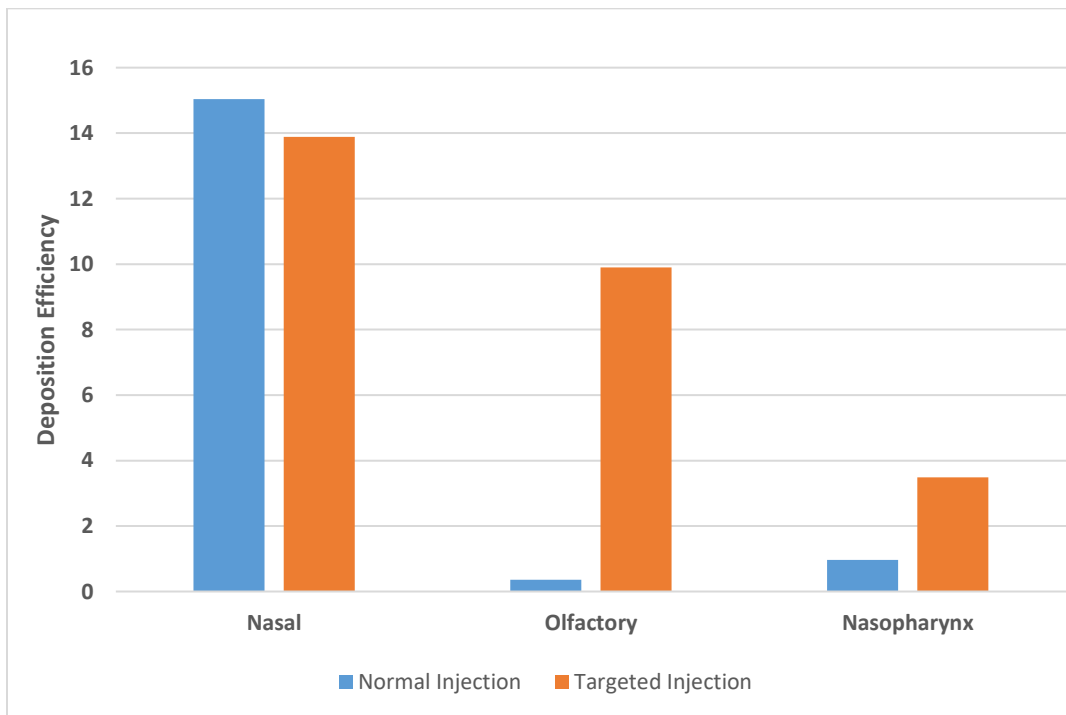


Figure 5.12.2 Deposition efficiency comparison between normal and targeted injection.

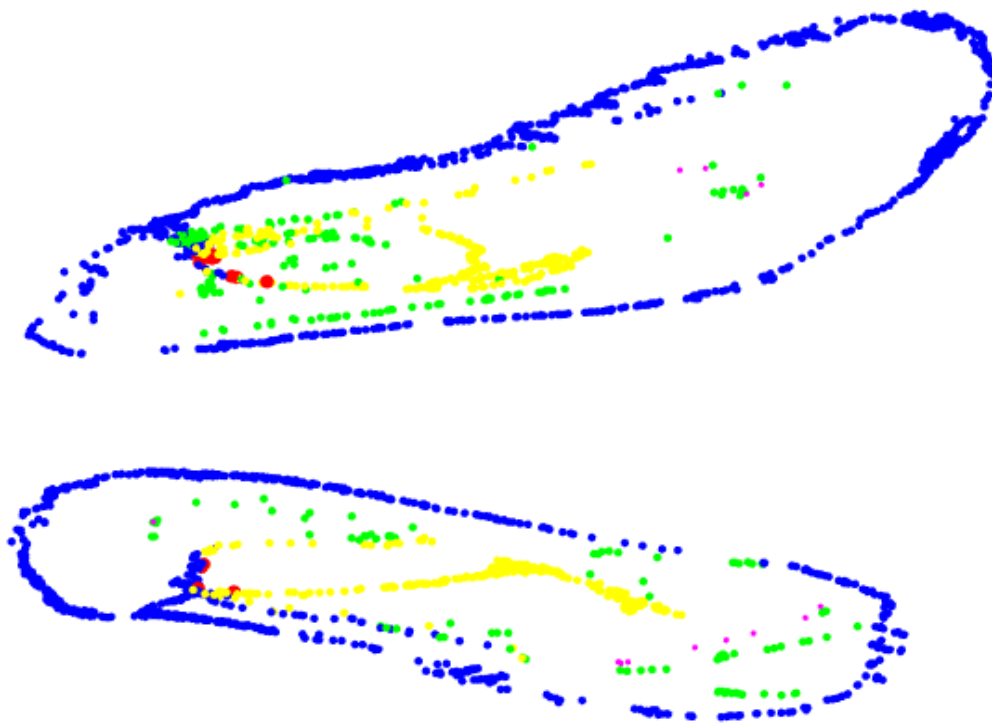


Figure 5. 13.1. PRM of 100 nm particles for the flowrate of 5 lpm.

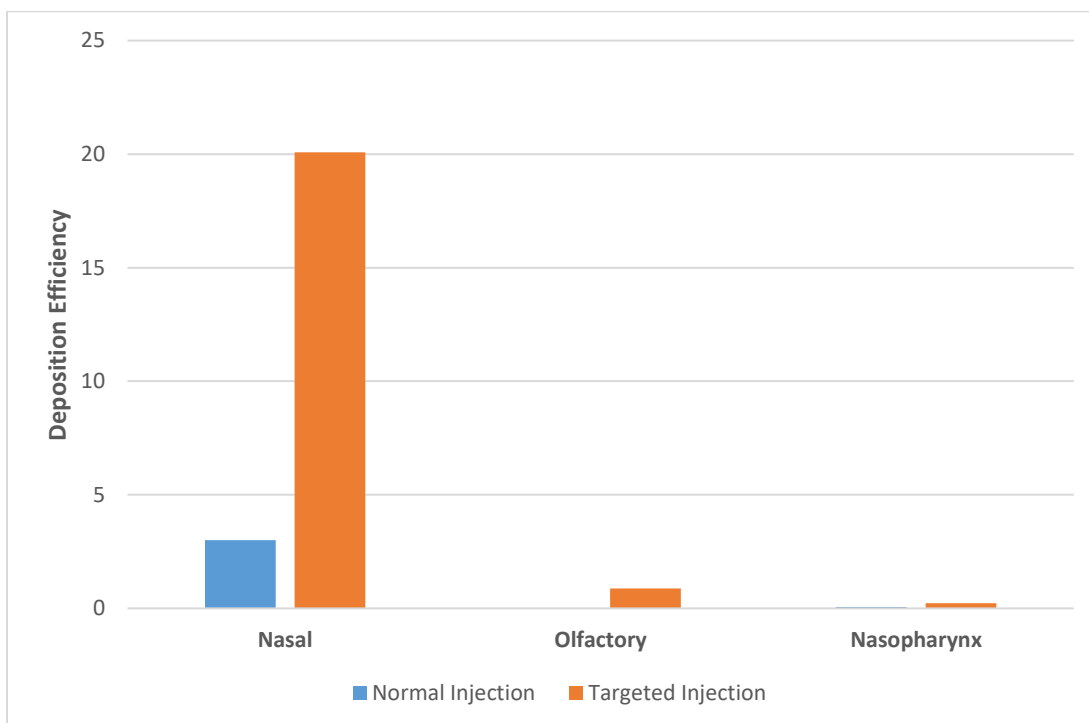


Figure 5.13.2. Deposition efficiency comparison between normal and targeted injection.

Figures 5.14-5.16 are for a flowrate of 20 lpm; where subsection 1 represents the particle release map and subsection 2 shows the comparison between normal and targeted injections. As expected, for small sized nanoparticles, targeted injection substantially increases the olfactory deposition efficiency with the maximum increase from 1 to 50% (see Figure 5.14.2). However, drug-particle sizes below 50nm are presently not available. The effect of targeted injection decreases with the increase in particle size. This is because for very small nanoparticles there is a well-defined region for olfactory deposition in the particle release map, whereas for 100nm particles there are only distinct points on the particle release map corresponding to olfactory deposition. This results in olfactory deposition efficiencies of 0.87% and 1.15% for Figures 5.13.2 and 5.16.2, respectively. The deposition pattern of 10nm particles for a 20 lpm flowrate due to normal and targeted injection is shown in Figure 5.17 and Figure 5.18 respectively. It shows that the targeted injection greatly changes the deposition pattern inside the nasal geometry. Normal injection results in a uniformly spread deposition pattern, while the targeted injection concentrates the particles in the upper region of the nasal cavity closer to the olfactory region. The comparison between Figure 5.8 and Figure 5.18 highlight the differences in the behavior of micron particles and nanoparticles. The phenomenon of targeted injection works on low sized nanoparticles due to the property of nanoparticles to follow the streamlines. Micron particles on the other hand are carried away by inertia and deposit in regions other than the intended target. The impact of targeted injection decreases with the increase in the particle diameter size (Figure 5.19). Furthermore higher flowrate generates higher olfactory deposition efficiency.

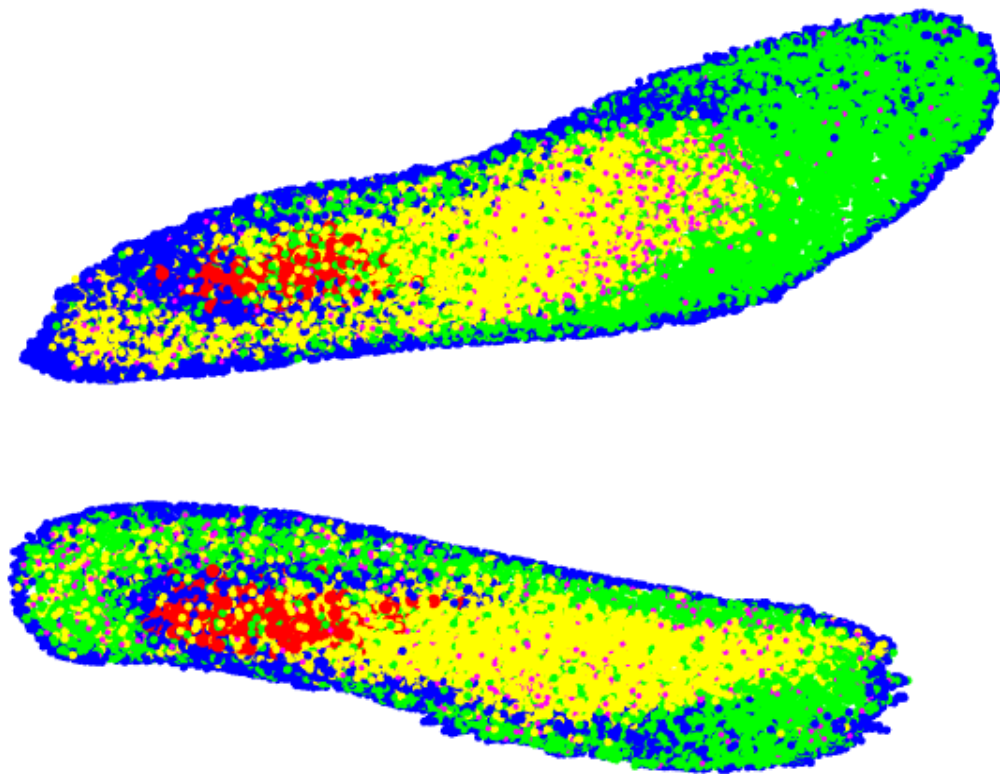


Figure 5. 14.1. PRM of 1 nm particles for the flowrate of 20 lpm.

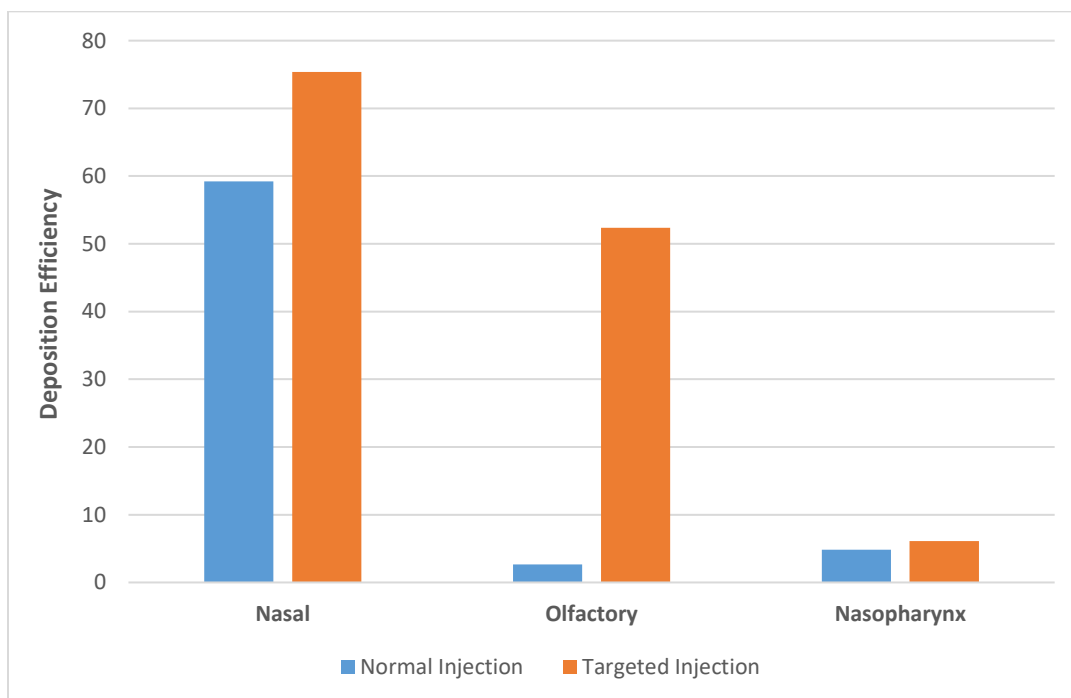


Figure 5.14.2. Deposition efficiency comparison between normal and targeted injection.

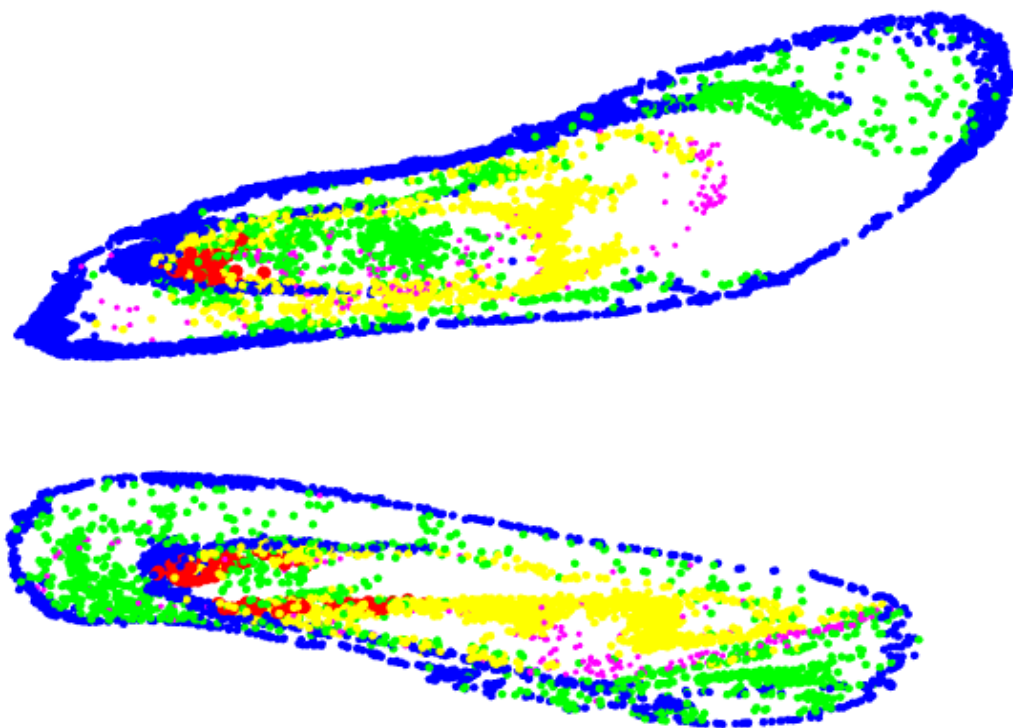


Figure 5. 15.1. PRM of 10 nm particles for the flowrate of 20 lpm.

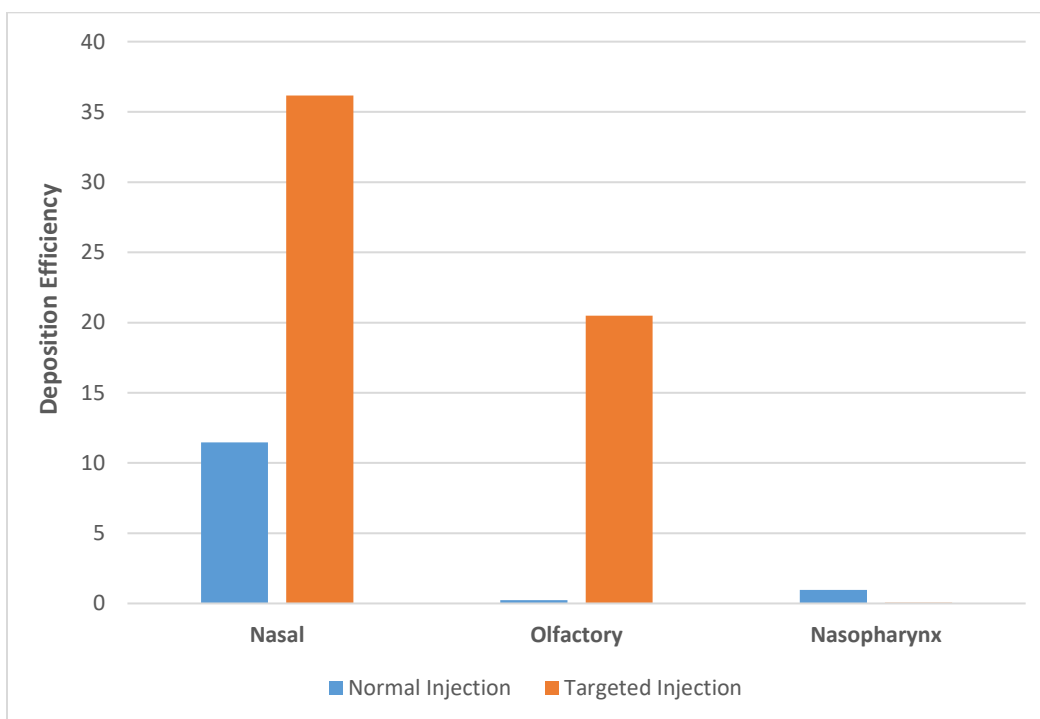


Figure 5.15.2. Deposition efficiency comparison between normal and targeted injection.

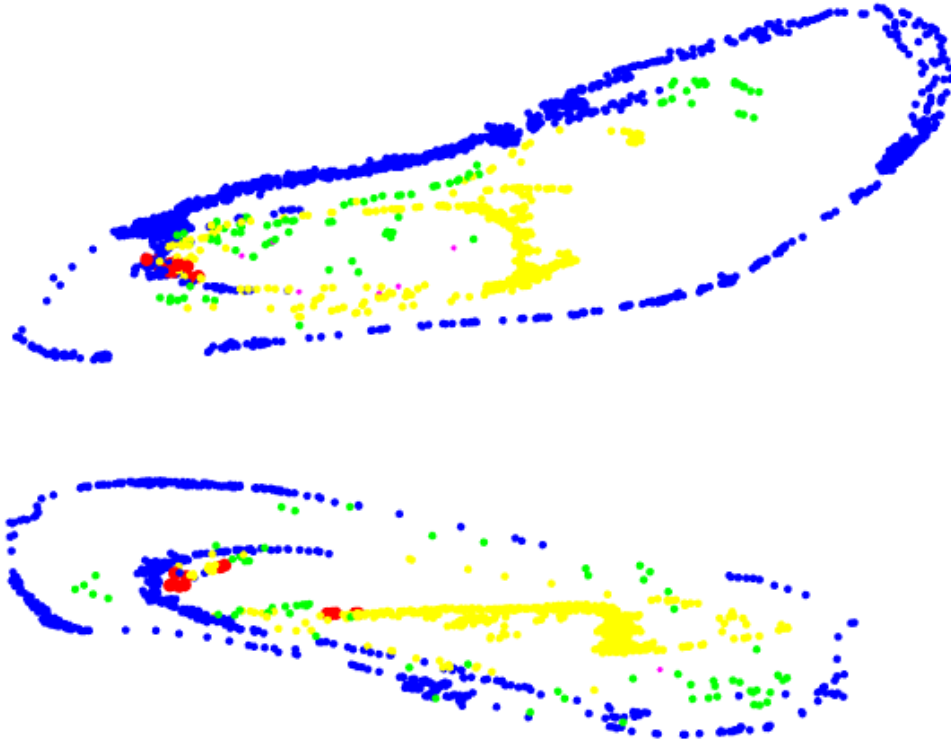


Figure 5. 16.1. PRM of 100 nm particles for the flowrate of 20 lpm.

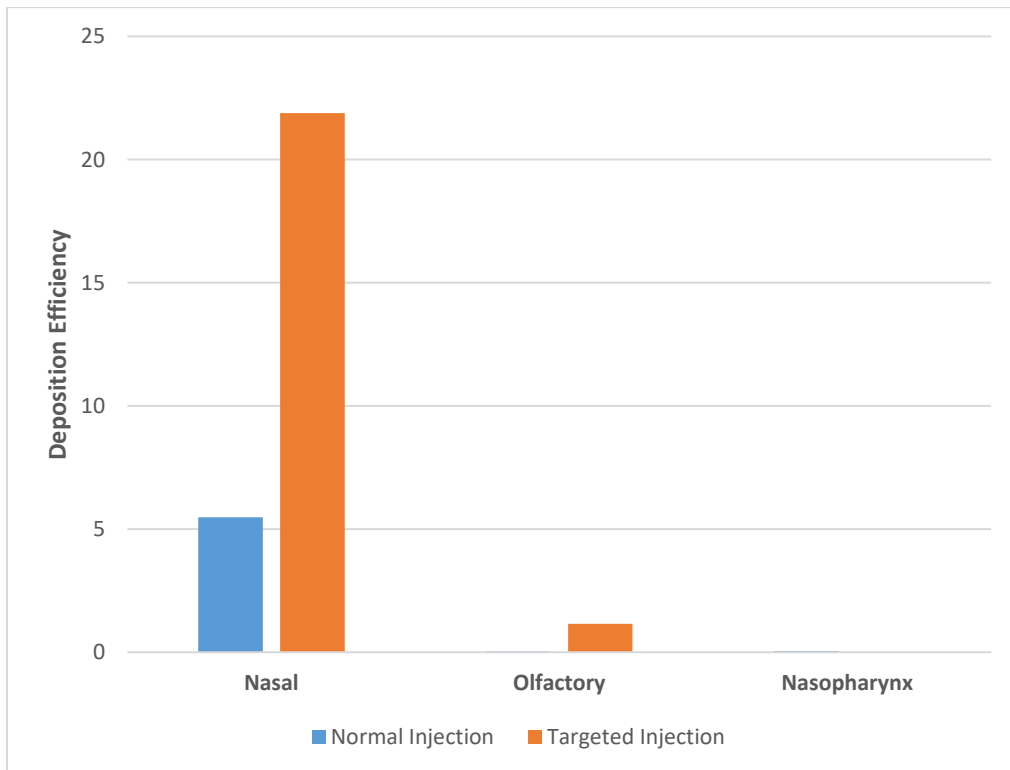


Figure 5.16.2. Deposition efficiency comparison between normal and targeted injection.

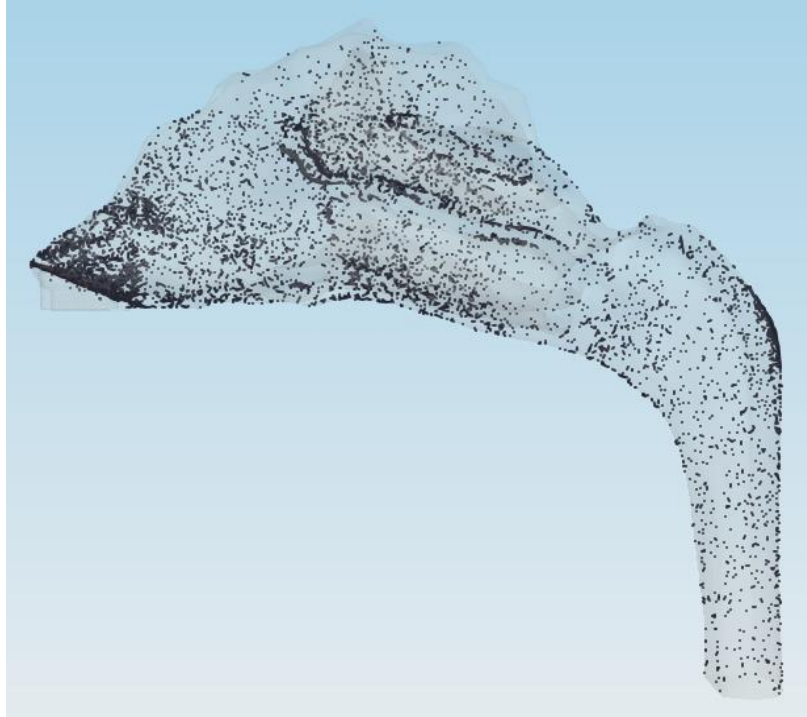


Figure 5. 17. Deposition Pattern due to normal injection of 10 nm particles for a flowrate of 20 lpm.

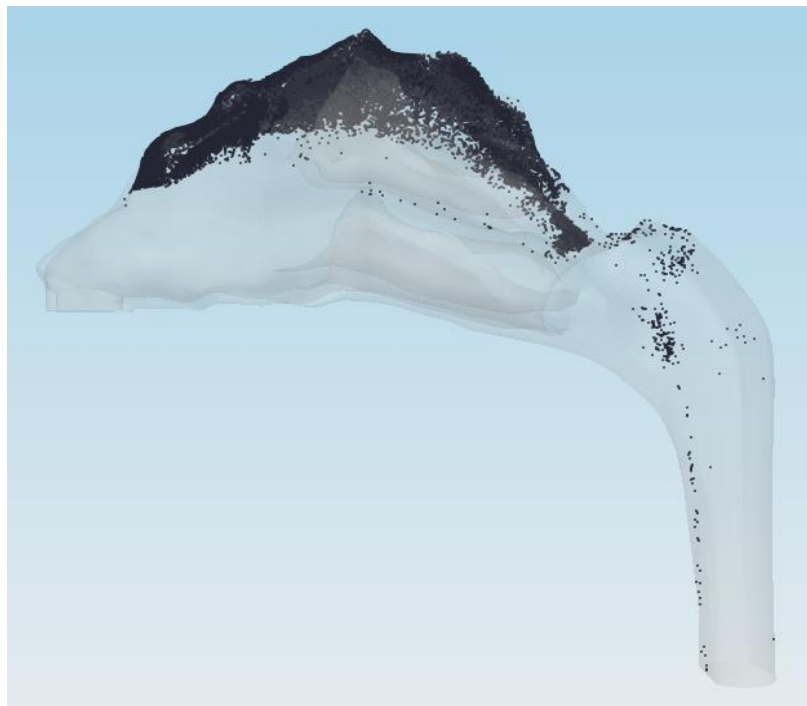


Figure 5. 18. Deposition Pattern due to targeted injection of 10 nm particles for a flowrate of 20 lpm.

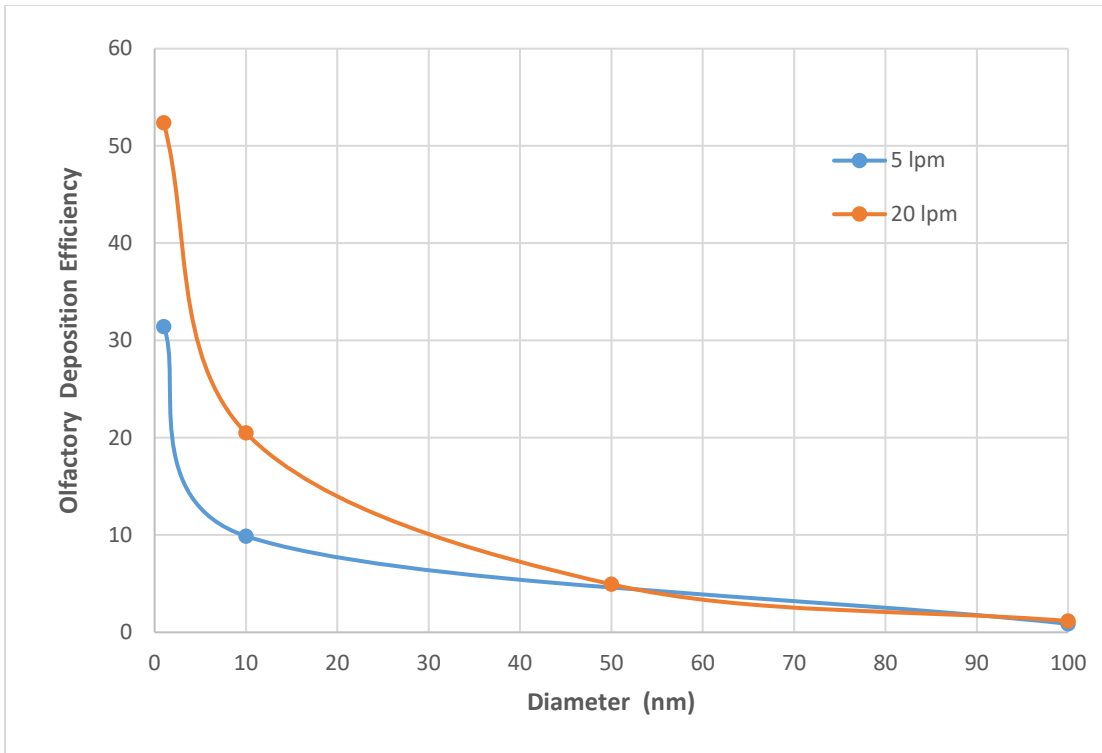


Figure 5. 19. Olfactory Deposition Efficiency trend due to targeted injection.

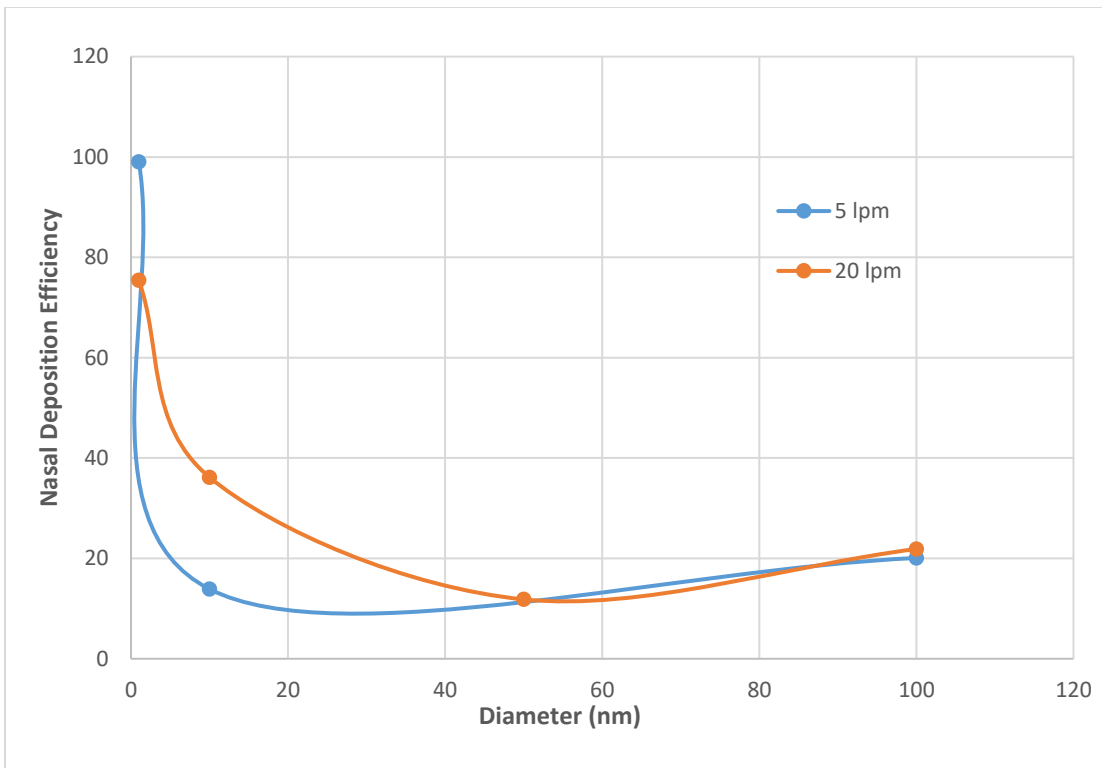


Figure 5. 20. Nasal Deposition Efficiency trend due to targeted injection.

CHAPTER 6. NASAL CANNULA FOR OLFACTORY DRUG TARGETING

6.1 Introduction

As indicated with the particle release maps (PRMs) for nanoparticles (as shown in Chapter 5) nanoparticles are unable to cross the streamlines owing to their low inertia. Hence, the most effective way of transporting nanoparticles to the olfactory region is to introduce particles into the streamlines that reach the desired site or region. From the PRMs, it is observed that the streamlines close to the narrower section of the nostrils travel to the olfactory region and hence that would be the optimal position of injection to achieve maximum olfactory deposition.

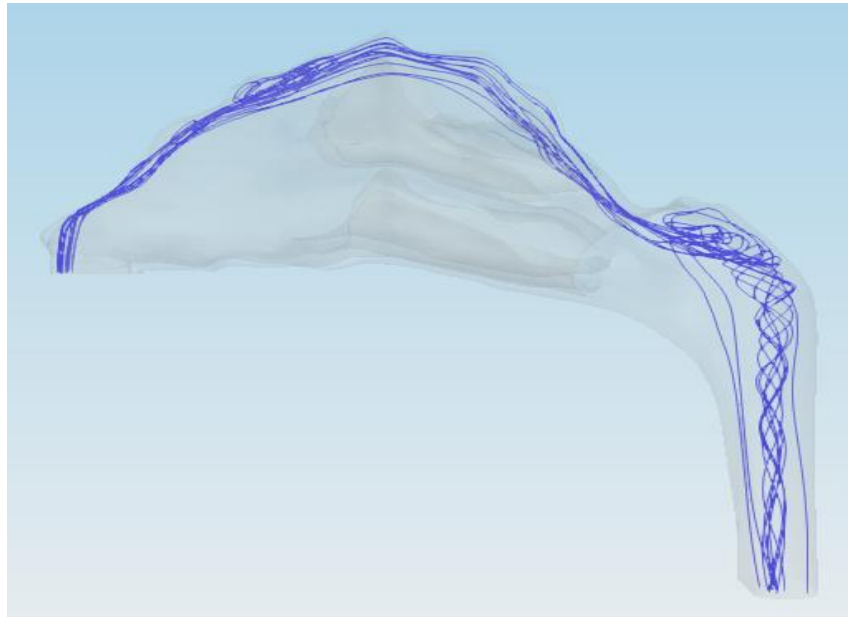


Figure 6. 1. Streamlines to the olfactory region.

Figure 6.1 shows the streamlines going to the olfactory region. The reason for the low olfactory deposition efficiency is that the major amount of streamlines pass through the lower and middle meatuses. This is the principle behind targeted injection in Chapter 5. In this chapter, computer experiments are conducted to analyze the deposition of particles by employing a nebulizer (or inhaler) with a cannula-type attachment to reach further inside the nasal cavity geometry. Cannulas

have been used in High flow Nasal Cannula (HFNC) therapy for ventilation as well as aerosolized drug transport (Figure 6.2) to lung areas. The cannula with its position of injection are shown in Figure 6.3 along with the direction of the injection of the particles.

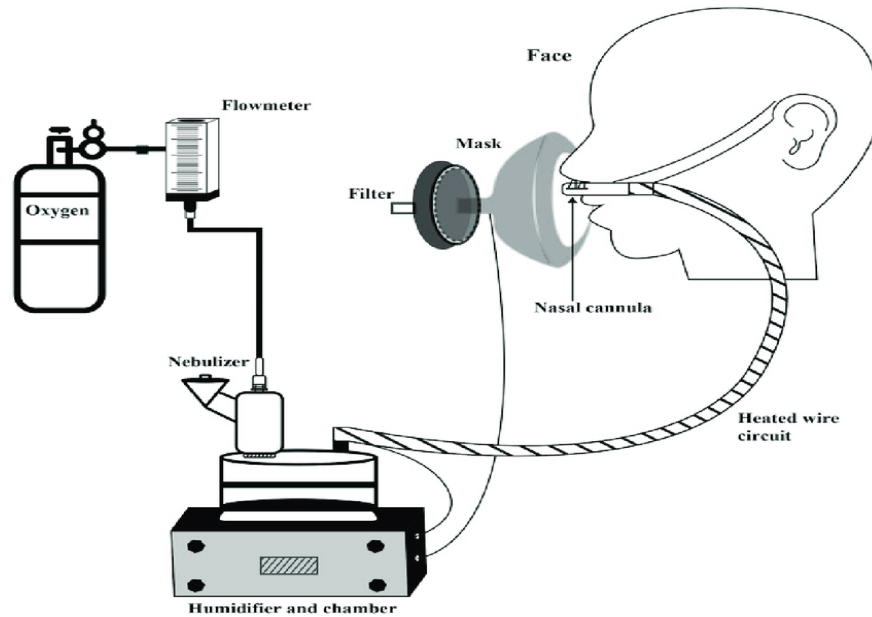


Figure 6. 2. Schematic of aerosol delivery using HFNC with a nebulizer.(45)

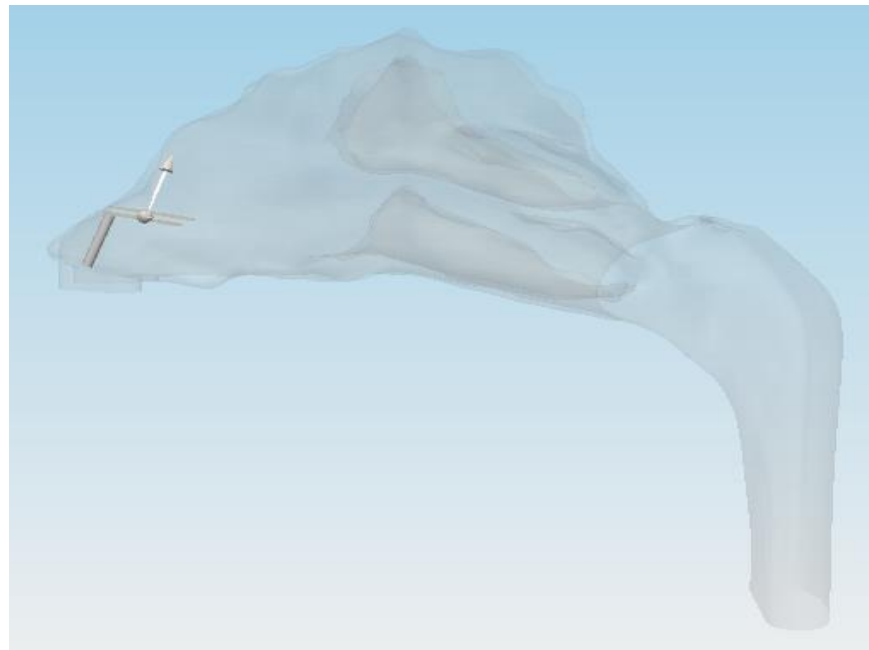


Figure 6. 3. Position of the injection of particles from the cannula.

Again using the methodology of the particle release map, first particles are injected uniformly from the plane shown above and then a simulation focusing on targeted injection is conducted. The nanoparticles were injected with a test velocity of 10 m/s. The distance between the plane of injection and nostril entrance was approximately 1cm. For the purposes of this study, a sedentary breathing rate of 20 lpm and particle sizes of 10nm, 50nm and 2 μm were considered.

6.2. Results and Discussion

Figures 6.4.1, 6.5.1 and 6.6.1 show the particle release maps for 2 μm , 10nm and 50nm spheres at the cannula-exit plane. Comparing these figures to that of the particle release maps of the nostrils, it can be inferred that the positioning of the cannula outlet does not measurably affect the airflow fields and hence particle deposition in the olfactory region. The optimal position of the injection is still the narrower section of the plane. The PRMs of Chapter 5 were created for a zero injection velocity of particles while the cannula injection was at 10 m/s. Despite the difference in the velocity of injection, there is not much difference in the PRMs. This indicates that the angle of injection and velocity of injection does not affect the trajectory of nanoparticles as long as they are embedded in the correct streamlines. It can also be observed that the region of olfactory deposition is small and hence the diameter of the cannula outlet is set to be 0.5mm. Figures 6.4.2, 6.5.2 and 6.6.2 show the deposition pattern due to cannula injection of 2 μm , 10 nm and 50 nm particles respectively for the flowrate of 20 lpm. As mentioned in the previous chapter, the concept of targeted injection works better for nanoparticles. The deposition pattern for the 2 μm particles shows that the particles are depositing before the olfactory region. This is because the injection velocity enables the micron particles to counteract the inertia of the airflow which is not the case with nanoparticles. However, this streamline crossing inhibits the transport of the particles further into the olfactory region. This phenomenon is visible by the distribution pattern in Figure 6.4.2.

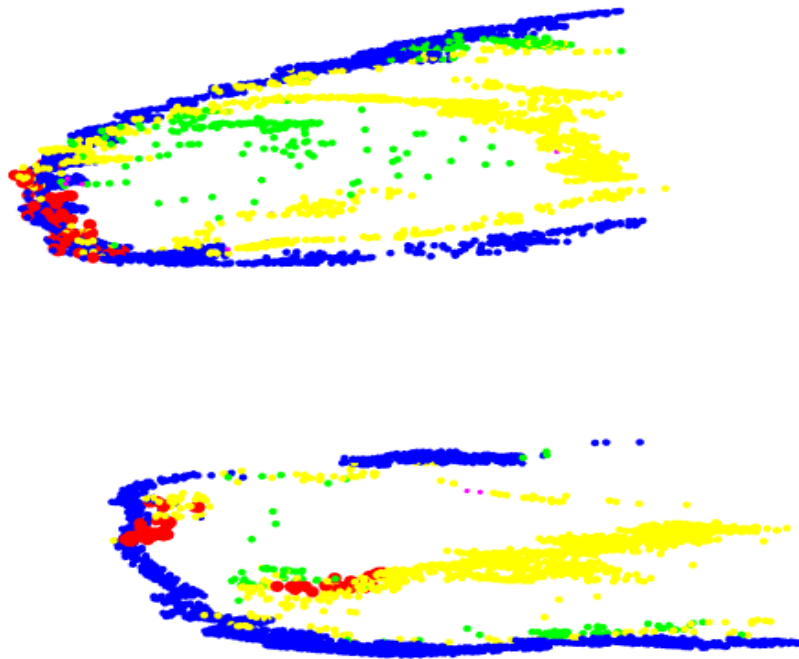


Figure 6. 4.1. PRM of 2 μm particles for the flowrate of 20 lpm (Cannula plane).

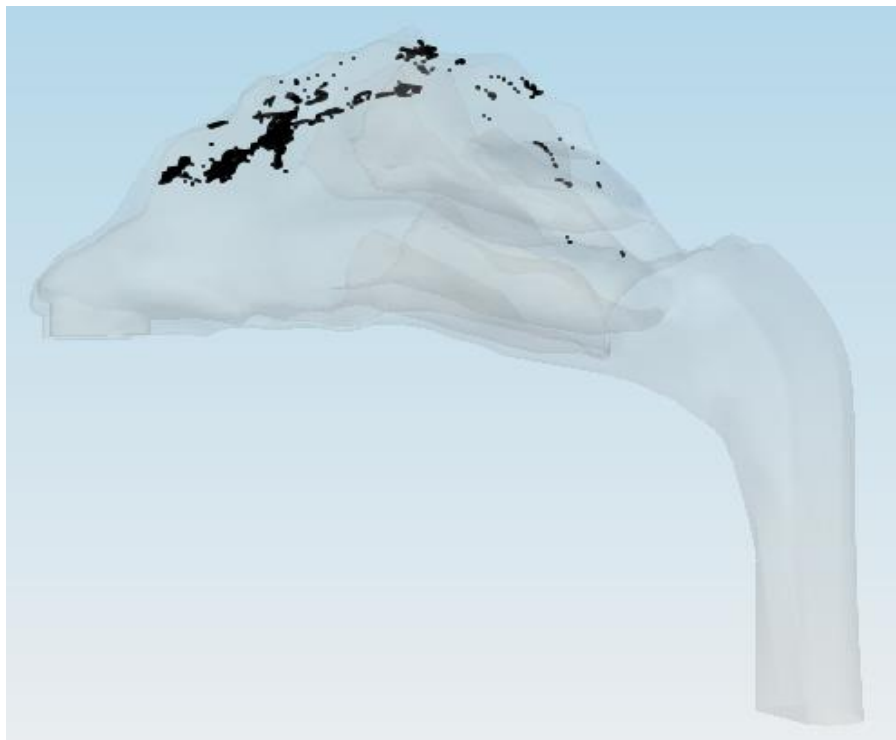


Figure 6.4.2. Deposition pattern as a result of cannula injection.

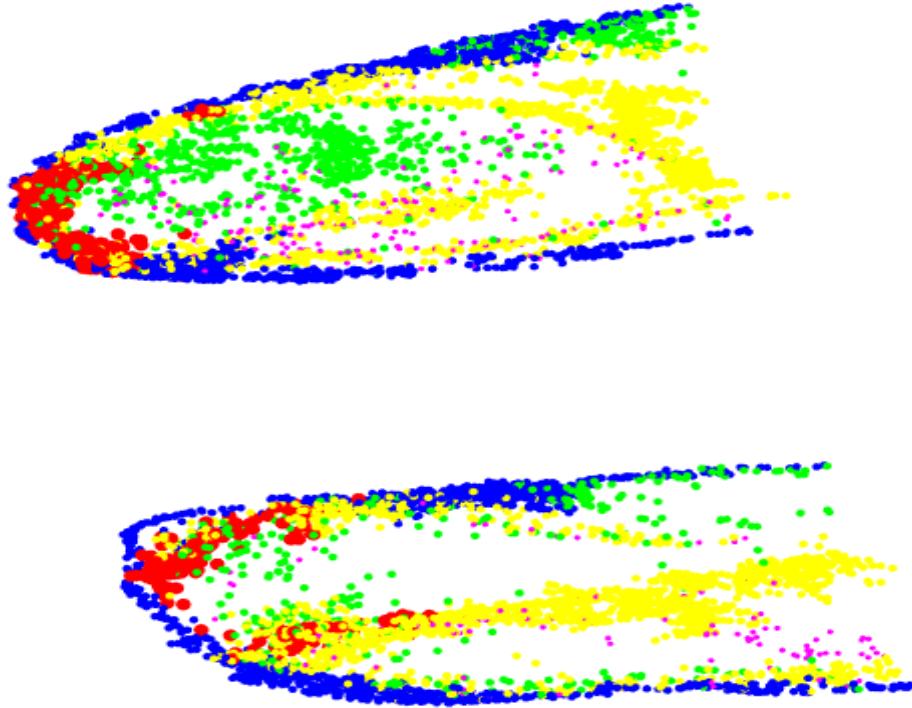


Figure 6. 5.1. PRM of 10 nm particles for the flowrate of 20 lpm
(Cannula plane).

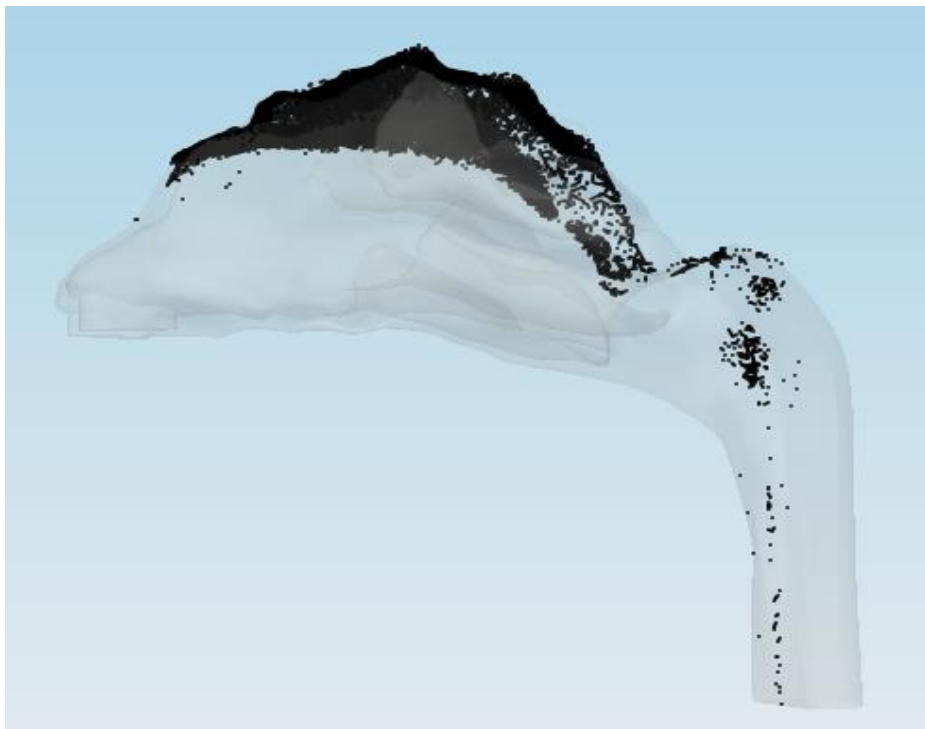


Figure 6.5.2. Deposition pattern as a result of cannula injection.

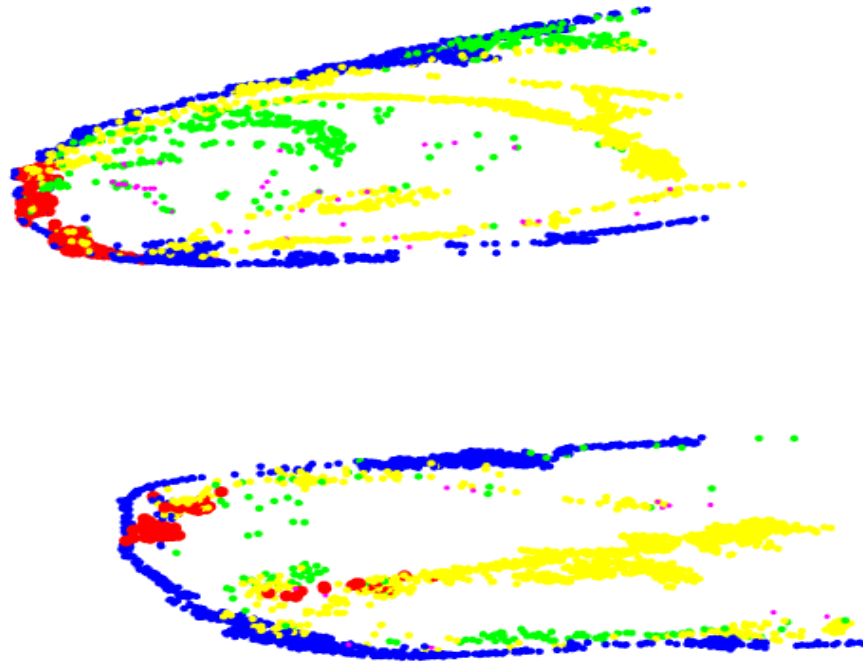


Figure 6. 6.1. PRM of 50 nm particles for the flowrate of 20 lpm
(Cannula plane).



Figure 6.6.2. Deposition pattern as a result of cannula injection.

Nanoparticle distributions on the other hand (see Figures 6.5.2 and 6.6.2) show significant olfactory depositions, as anticipated. Table 6.1 lists the olfactory deposition efficiencies for the three aforementioned cases. Nanoparticles show considerably more olfactory deposition than micron particles. Furthermore, a steep decline in olfactory deposition occurs for larger nanoparticles. To investigate further a second set of simulations are conducted where the speed

Table 6. 1. Olfactory deposition efficiencies for Cannula Injection (SOI = 10 m/s)

Particle Diameter	Olfactory Deposition Efficiency
2e-6 μm	1.638
10 nm	41.3
50 nm	11.25
100 nm	10.45

of injection is 3.5 m/s which is approximately equal to the velocity of the surrounding fluid. This is done. This is done so as to remove the dependence of the inertia of the particles and embed the particles in the flowstream. The results are shown in Table 6.2. Comparing the two tables, it can be inferred that the velocity of injection certainly impacts the olfactory deposition efficiencies. Higher olfactory deposition is observed for higher SOI because more particles reach the streamlines travelling to the olfactory region.

Table 6. 2. Olfactory deposition efficiencies for Cannula injection (SOI = 3.5 m/s)

Particle Diameter	Olfactory deposition efficiency
10 nm	29.93
50 nm	4.87
100 nm	3.47

CHAPTER 7. CONCLUSION AND FUTURE WORK

The olfactory region in the nasal cavity is an important gateway for transporting drug particles into the brain for the treatment of various central nervous system disorders. Drug injection via the nasal route serves as a promising non-invasive technique for drug delivery. However the complex structure of the human nasal cavity inhibits the transport of the particles to the olfactory region. Particle sizes ranging from 1-50nm are optimal for actively crossing the Blood Brain Barrier via active or passive (ie, diffusional) processes. This study aims at increasing the deposition of nanoparticles in the olfactory region.

Chapter 4 deals with validating the simulation approach of micron particles vs. nanoparticles by comparing the deposition from previous studies. Through these studies it has been found that micron particles show almost no olfactory deposition while nanoparticles show a maximum deposition of 3-4% for particles of sizes between 1 and 2 nm. Particles above the size of 10 nm show negligible deposition on the olfactory epithelium. Extremely small nanodrugs are not possible to manufacture and/or generate with the current atomization technologies.

Chapter 5 employs the particle release map (PRM) approach to determine the optimal position of injection for elevated olfactory deposition. The PMRs further illustrated the behavior of particles in a sedentary flowrate of 20 lpm which corresponds to a normal breathing rate. The optimal injection point for targeting the olfactory region lies in the narrower section of the nostrils. Using the particle release maps, simulations were conducted to target the olfactory region and the results are very promising. Targeted injection achieves an olfactory deposition of 52 % (Figure 5.14.2) for 1 nm particles, 20% (Figure 5.15.2) for 10 nm particles and 1.15 % (Figure 5.16.2) for 100 nm particles at a breathing rate of 20lpm. For micron particles, a relatively less prominent effect of targeted injection has been observed. Normal injection resulted in a 2 % deposition for

2 μm , 11 % for 5 μm and 6 % for 10 μm particles for the same breathing rate. Through the targeted injection approach, a substantial increase in olfactory deposition was observed. This approach can be utilized for devices like nebulizers that inject drug particles through the nostrils.

A preliminary study to test the use of a cannula-type device was done in Chapter 6. The cannula-exit plane was placed at approximately 1cm from the nostrils and the particles were injected with a test velocity of 3.5 m/s (velocity of the flow) and 10 m/s. The idea behind this is that the further the injection point from the nostril, the less the nanoparticles will diffuse before the olfactory region. Table 7.1 shows the comparison between the various injection methods used in this study. It can be seen that the cannula injection and targeted injection from the nostrils successfully increase the olfactory deposition. A consistent increase in the olfactory deposition is observed from normal injection to targeted injection and from targeted injection and cannula injection. Hence the preliminary study for cannula injection along with the particle release map approach should be further studied by incorporating realistic conditions for olfactory drug targeting.

Table 7. 1. Olfactory deposition comparison between the injection methods.

Olfactory Deposition Efficiency				
Particle Diameter	Normal Injection	Targeted Injection	Cannula Injection (SOI = 3.5 m/s)	Cannula Injection (SOI = 10 m/s)
10 nm	0.24	20.49	29.93	41.31
50 nm	0.04	4.93	4.87	11.25
100 nm	0.03	1.16	3.47	10.43

Although this study has shown promising results in increasing nanoparticle deposition in the olfactory bulb, it is subject to many assumptions. To implement this approach of targeted injection more realistically, subsequent CF-PD studies have to be performed.

- All the simulations have been conducted under the assumption of pseudo-steady state. This was done so as to conduct a parametric study for the deposition of particles in the olfactory region. However, for simulating realistic breathing cycles, this approach of targeted injection has to be employed by conducting transient studies for normal breathing rates and sniffing breathing rate profiles.
- One-way coupling has been employed for the cannula study with micron particles. However a more accurate depiction of the flow physics can be captured via two-way coupling. The particle injection velocity from the cannula is approximately 10 m/s, which disturbs the air around the particles and subsequently affects the drag computations. One – way coupling over-predicts the drag value because it does not account for the change of velocity around the particles. Hence two-way coupling is a more accurate option for Lagrangian tracking of high inertia particles.
- In this study the mucus layers of the nasal cavity is not considered. The presence of the mucus dynamics quantitatively affects particle deposition.
- The particles in this study were treated primarily as a solid. For liquid formulations additional considerations have to be incorporated to model the physics completely. For high inertia droplets, usually a breakup is observed when the drag force dominates over the surface tension force. This breakup reduces the size of the droplets which may be beneficial as injected micron particles turn into nanoparticles as they move through the nasal cavity which might aid the transport to the olfactory region

The outcomes of this study reveal that targeted injection using the cannula significantly increases the olfactory deposition efficiency and thereby this methodology can be utilized for effective olfactory drug targeting. This study will be submitted in the form of following manuscripts.

- “Computer Simulation and Analysis of Nanoparticle Delivery to the Olfactory Bulb for Direct Drug Migration to the Brain” in the Journal of Drug Delivery.
- “Computational study of the behavior of micron and nano particles in a representative human cavity model” in the Journal of Aerosol Science.
- “The use of a nasal cannula in conjunction with a nebulizer for efficient olfactory drug targeting” in the Journal of Drug Delivery Science and Technology.

REFERENCES

1. Lalatsa A, Leite DM, Figueiredo MF, O'Connor M. Nanotechnology in Brain Tumor Targeting: Efficacy and Safety of Nanoenabled Carriers Undergoing Clinical Testing. In: Nanotechnology-Based Targeted Drug Delivery Systems for Brain Tumors. Elsevier; 2018. p. 111-45.
2. Dolecek TA, Propp JM, Stroup NE, Kruchko C. CBTRUS statistical report: primary brain and central nervous system tumors diagnosed in the United States in 2005–2009. *Neuro-oncology*. 2012;14(suppl_5):v1-v49.
3. Burgess A, Hynynen K. Noninvasive and targeted drug delivery to the brain using focused ultrasound. *ACS chemical neuroscience*. 2013;4(4):519-26.
4. Azad TD, Pan J, Connolly ID, Remington A, Wilson CM, Grant GA. Therapeutic strategies to improve drug delivery across the blood-brain barrier. *Neurosurgical focus*. 2015;38(3):E9.
5. Lesniak MS, Brem H. Targeted therapy for brain tumours. *Nature reviews Drug discovery*. 2004;3(6):499.
6. Pajouhesh H, Lenz GR. Medicinal chemical properties of successful central nervous system drugs. *NeuroRx*. 2005;2(4):541-53.
7. Agrawal M, Saraf S, Saraf S, Antimisiaris SG, Chougule MB, Shoyele SA, et al. Nose-to-brain drug delivery: An update on clinical challenges and progress towards approval of anti-Alzheimer drugs. *J Controlled Release*. 2018;281:139-77.

8. Khan AR, Liu M, Khan MW, Zhai G. Progress in brain targeting drug delivery system by nasal route. *J Controlled Release*. 2017;268:364-89.
9. Parrish KE, Sarkaria JN, Elmquist WF. Improving drug delivery to primary and metastatic brain tumors: strategies to overcome the blood–brain barrier. *Clinical Pharmacology & Therapeutics*. 2015;97(4):336-46.
10. Liu H, Hua M, Chen P, Chu P, Pan C, Yang H, et al. Blood-brain barrier disruption with focused ultrasound enhances delivery of chemotherapeutic drugs for glioblastoma treatment. *Radiology*. 2010;255(2):415-25.
11. Nicholson C, Syková E. Extracellular space structure revealed by diffusion analysis. *Trends Neurosci*. 1998;21(5):207-15.
12. Nagpal S. The role of BCNU polymer wafers (Gliadel) in the treatment of malignant glioma. *Neurosurgery Clinics*. 2012;23(2):289-95.
13. Brem H, Gabikian P. Biodegradable polymer implants to treat brain tumors. *J Controlled Release*. 2001;74(1-3):63-7.
14. Lin SH, Kleinberg LR. Carmustine wafers: localized delivery of chemotherapeutic agents in CNS malignancies. *Expert review of anticancer therapy*. 2008;8(3):343-59.
15. Scott AW, Tyler BM, Masi BC, Upadhyay UM, Patta YR, Grossman R, et al. Intracranial microcapsule drug delivery device for the treatment of an experimental gliosarcoma model. *Biomaterials*. 2011;32(10):2532-9.

16. Eltorai AE, Fox H, McGurrin E, Guang S. Microchips in medicine: current and future applications. *BioMed research international*. 2016;2016.
17. Kim GY, Tyler BM, Tupper MM, Karp JM, Langer RS, Brem H, et al. Resorbable polymer microchips releasing BCNU inhibit tumor growth in the rat 9L flank model. *J Controlled Release*. 2007;123(2):172-8.
18. Malakoutikhah M, Teixidó M, Giralt E. Shuttle-mediated drug delivery to the brain. *Angewandte Chemie International Edition*. 2011;50(35):7998-8014.
19. Vieira DB, Gamarra LF. Multifunctional Nanoparticles for Successful Targeted Drug Delivery across the Blood-Brain Barrier. In: *Molecular Insight of Drug Design*. IntechOpen; 2018.
20. Etame AB, Smith CA, Chan WC, Rutka JT. Design and potential application of PEGylated gold nanoparticles with size-dependent permeation through brain microvasculature. *Nanomedicine: Nanotechnology, Biology and Medicine*. 2011;7(6):992-1000.
21. Hanada S, Fujioka K, Inoue Y, Kanaya F, Manome Y, Yamamoto K. Cell-based in vitro blood-brain barrier model can rapidly evaluate nanoparticles' brain permeability in association with particle size and surface modification. *International journal of molecular sciences*. 2014;15(2):1812-25.
22. Sonavane G, Tomoda K, Makino K. Biodistribution of colloidal gold nanoparticles after intravenous administration: effect of particle size. *Colloids and Surfaces B: Biointerfaces*. 2008;66(2):274-80.

23. Kolhar P, Anselmo AC, Gupta V, Pant K, Prabhakar Pandian B, Ruoslahti E, et al. Using shape effects to target antibody-coated nanoparticles to lung and brain endothelium. *Proceedings of the National Academy of Sciences*. 2013;110(26):10753-8.
24. Decuzzi P, Godin B, Tanaka T, Lee S, Chiappini C, Liu X, et al. Size and shape effects in the biodistribution of intravascularly injected particles. *J Controlled Release*. 2010;141(3):320-7.
25. Georgieva JV, Hoekstra D, Zuhorn IS. Smuggling drugs into the brain: an overview of ligands targeting transcytosis for drug delivery across the blood–brain barrier. *Pharmaceutics*. 2014;6(4):557-83.
26. Moinuddin S, Razvi SH, Uddin MS, Fazil M, Shahidulla SM, Akmal MM. Nasal drug delivery system: A innovative approach. *Perception*. 2019;15:16.
27. Hasan MM, Rahman MM, Kabir AK, Ghosh AK, Hasan M, Karim MS, et al. Contemporary investigation on nasal spray drug delivery system. . 2016.
28. Rakesh N, Khan AB. Targeted drug delivery systems mediated through nasal delivery for improved absorption: an update. *RGUHS J Pharm Sci*. 2015;5:4-20.
29. Gänger S, Schindowski K. Tailoring formulations for intranasal nose-to-brain delivery: A review on architecture, physico-chemical characteristics and mucociliary clearance of the nasal olfactory mucosa. *Pharmaceutics*. 2018;10(3):116.
30. Kublik H, Vidgren MT. Nasal delivery systems and their effect on deposition and absorption. *Adv Drug Deliv Rev*. 1998;29(1-2):157-77.

31. Marple B, Roland P, Benninger M. Safety review of benzalkonium chloride used as a preservative in intranasal solutions: an overview of conflicting data and opinions. *Otolaryngology-Head and Neck Surgery*. 2004;130(1):131-41.
32. Chauhan H, Liu-Cordero SN, Liao L, Werbeck J. IMPACT OF ACTUATOR DESIGN ON MULTI-DOSE NASAL SPRAY CHARACTERISTICS.
33. Djupesland PG, Messina JC, Mahmoud RA. The nasal approach to delivering treatment for brain diseases: an anatomic, physiologic, and delivery technology overview. *Therapeutic delivery*. 2014;5(6):709-33.
34. O'Callaghan C, Barry PW. The science of nebulised drug delivery. *Thorax*. 1997;52(Suppl 2):S31.
35. Knoch M, Finlay W. Nebulizer technologies. *Drugs Pharm Sci*. 2003;126:849-56.
36. Ruzycki CA, Javaheri E, Finlay WH. The use of computational fluid dynamics in inhaler design. *Expert opinion on drug delivery*. 2013;10(3):307-23.
37. Djupesland PG. Nasal drug delivery devices: characteristics and performance in a clinical perspective—a review. *Drug delivery and translational research*. 2013;3(1):42-62.
38. Xi J, Si XA. Numerical simulation and experimental testing to improve olfactory drug delivery with electric field guidance of charged particles. *Advanced Technology for Delivering Therapeutics*. 2017:89.

39. Katial RK, Reisner C, Buchmeier A, Bartelson BB, Nelson HS. Comparison of three commercial ultrasonic nebulizers. *Annals of Allergy, Asthma & Immunology*. 2000;84(2):255-61.
40. Bauer A, McGlynn P, Bovet LL, Mims PL, Curry LA, Hanrahan JP. Output and aerosol properties of 5 nebulizer/compressor systems with arformoterol inhalation solution. *Respir Care*. 2009;54(10):1342-7.
41. Loffert DT, Ikle D, Nelson HS. A comparison of commercial jet nebulizers. *Chest*. 1994;106(6):1788-92.
42. Longest PW, Golshahi L, Hindle M. Improving pharmaceutical aerosol delivery during noninvasive ventilation: effects of streamlined components. *Ann Biomed Eng*. 2013;41(6):1217-32.
43. Tian G, Hindle M, Longest PW. Targeted lung delivery of nasally administered aerosols. *Aerosol Science and Technology*. 2014;48(4):434-49.
44. Wallin M, Tang P, Chang RYK, Yang M, Finlay WH, Chan H. Aerosol drug delivery to the lungs during nasal high flow therapy: an in vitro study. *BMC pulmonary medicine*. 2019;19(1):42.
45. Alcoforado L, Ari A, Barcelar JdM, Brandão SCS, Fink JB, de Andrade AD. Impact of Gas Flow and Humidity on Trans-Nasal Aerosol Deposition via Nasal Cannula in Adults: A Randomized Cross-Over Study. *Pharmaceutics*. 2019;11(7):320.

46. Longest W, Spence B, Hindle M. Devices for Improved Delivery of Nebulized Pharmaceutical Aerosols to the Lungs. *Journal of aerosol medicine and pulmonary drug delivery*. 2019.
47. Spence BM, Longest W, Wei X, Dhapare S, Hindle M. Development of a High-Flow Nasal Cannula and Pharmaceutical Aerosol Combination Device. *Journal of aerosol medicine and pulmonary drug delivery*. 2019.
48. Haruta S, Tsutsui T. Meeting the needs for nasal delivery devices for powder formulations. *Drug Dev Deliv*. 2012;12(5):22-7.
49. Kaye RS, Purewal TS, Alpar OH. Development and testing of particulate formulations for the nasal delivery of antibodies. *J Controlled Release*. 2009;135(2):127-35.
50. Pringels E, Callens C, Vervaet C, Dumont F, Slegers G, Foreman P, et al. Influence of deposition and spray pattern of nasal powders on insulin bioavailability. *Int J Pharm*. 2006;310(1-2):1-7.
51. Huang J, Garmise RJ, Crowder TM, Mar K, Hwang CR, Hickey AJ, et al. A novel dry powder influenza vaccine and intranasal delivery technology: induction of systemic and mucosal immune responses in rats. *Vaccine*. 2004;23(6):794-801.
52. Cheng K, Cheng Y, Yeh H, Guilmette RA, Simpson SQ, Yang Y, et al. In vivo measurements of nasal airway dimensions and ultrafine aerosol deposition in the human nasal and oral airways. *J Aerosol Sci*. 1996;27(5):785-801.

53. Cheng YS, Yeh HC, Guilmette RA, Simpson SQ, Cheng KH, Swift DL. Nasal deposition of ultrafine particles in human volunteers and its relationship to airway geometry. *Aerosol Science and Technology*. 1996;25(3):274-91.
54. Cheng Y, Smith SM, Yeh H, Kim D, Cheng K, Swift DL. Deposition of ultrafine aerosols and thoron progeny in replicas of nasal airways of young children. *Aerosol Science and Technology*. 1995;23(4):541-52.
55. Oberdörster G, Sharp Z, Atudorei V, Elder A, Gelein R, Kreyling W, et al. Translocation of inhaled ultrafine particles to the brain. *Inhal Toxicol*. 2004;16(6-7):437-45.
56. Hopkins LE, Patchin ES, Chiu P, Brandenberger C, Smiley-Jewell S, Pinkerton KE. Nose-to-brain transport of aerosolised quantum dots following acute exposure. *Nanotoxicology*. 2014;8(8):885-93.
57. Wang SM, Inthavong K, Wen J, Tu JY, Xue CL. Comparison of micron-and nanoparticle deposition patterns in a realistic human nasal cavity. *Respiratory physiology & neurobiology*. 2009;166(3):142-51.
58. Shang Y, Dong J, Inthavong K, Tu J. Comparative numerical modeling of inhaled micron-sized particle deposition in human and rat nasal cavities. *Inhal Toxicol*. 2015;27(13):694-705.
59. Shang YD, Inthavong K, Tu JY. Detailed micro-particle deposition patterns in the human nasal cavity influenced by the breathing zone. *Comput Fluids*. 2015;114:141-50.

60. Calmet H, Kleinstreuer C, Houzeaux G, Kolanjiyil AV, Lehmkuhl O, Olivares E, et al. Subject-variability effects on micron particle deposition in human nasal cavities. *J Aerosol Sci.* 2018;115:12-28.
61. Shi H, Kleinstreuer C, Zhang Z. Laminar airflow and nanoparticle or vapor deposition in a human nasal cavity model. *J Biomech Eng.* 2006;128(5):697-706.
62. Garcia GJ, Kimbell JS. Deposition of inhaled nanoparticles in the rat nasal passages: dose to the olfactory region. *Inhal Toxicol.* 2009;21(14):1165-75.
63. Kimbell JS, Gross EA, Joyner DR, Godo MN, Morgan KT. Application of computational fluid dynamics to regional dosimetry of inhaled chemicals in the upper respiratory tract of the rat. *Toxicol Appl Pharmacol.* 1993;121(2):253-63.
64. Kimbell JS, Godo MN, Gross EA, Joyner DR, Richardson RB, Morgan KT. Computer simulation of inspiratory airflow in all regions of the F344 rat nasal passages. *Toxicol Appl Pharmacol.* 1997;145(2):388-98.
65. Gerde P, Cheng YS, Medinsky MA. In vivo deposition of ultrafine aerosols in the nasal airway of the rat. *Toxicological Sciences.* 1991;16(2):330-6.
66. Cheng YS, Hansen GK, Su YF, Yeh HC, Morgan KT. Deposition of ultrafine aerosols in rat nasal molds. *Toxicol Appl Pharmacol.* 1990;106(2):222-33.
67. Wong BA, Tewksbury EW, Asgharian B. Nanoparticle deposition efficiency in rat and human nasal replicas. *Toxicologist.* 2008;62:310.

68. Tian L, Shang Y, Dong J, Inthavong K, Tu J. Human nasal olfactory deposition of inhaled nanoparticles at low to moderate breathing rate. *J Aerosol Sci.* 2017;113:189-200.
69. Tian L, Shang Y, Chen R, Bai R, Chen C, Inthavong K, et al. Correlation of regional deposition dosage for inhaled nanoparticles in human and rat olfactory. *Particle and fibre toxicology.* 2019;16(1):6.
70. Garcia GJ, Schroeter JD, Kimbell JS. Olfactory deposition of inhaled nanoparticles in humans. *Inhal Toxicol.* 2015;27(8):394-403.
71. Bahmanzadeh H, Abouali O, Ahmadi G. Unsteady particle tracking of micro-particle deposition in the human nasal cavity under cyclic inspiratory flow. *J Aerosol Sci.* 2016;101:86-103.
72. Jiang J, Zhao K. Airflow and nanoparticle deposition in rat nose under various breathing and sniffing conditions—a computational evaluation of the unsteady and turbulent effect. *J Aerosol Sci.* 2010;41(11):1030-43.
73. Calmet H, Houzeaux G, Vázquez M, Eguzkitza B, Gambaruto AM, Bates AJ, et al. Flow features and micro-particle deposition in a human respiratory system during sniffing. *J Aerosol Sci.* 2018;123:171-84.
74. Ganser GH. A rational approach to drag prediction of spherical and nonspherical particles. *Powder Technol.* 1993;77(2):143-52.
75. Kleinstreuer C, Zhang Z. Laminar-to-turbulent fluid-particle flows in a human airway model. *Int J Multiphase Flow.* 2003;29(2):271-89.

76. Ingham DB. Diffusion of aerosols from a stream flowing through a cylindrical tube. *J Aerosol Sci.* 1975;6(2):125-32.
77. Kelly JT, Asgharian B, Kimbell JS, Wong BA. Particle deposition in human nasal airway replicas manufactured by different methods. Part I: Inertial regime particles. *Aerosol Science and Technology.* 2004;38(11):1063-71.
78. Shi H, Kleinstreuer C, Zhang Z. Dilute suspension flow with nanoparticle deposition in a representative nasal airway model. *Phys Fluids.* 2008;20(1):013301.
79. Shi H, Kleinstreuer C, Zhang Z. Modeling of inertial particle transport and deposition in human nasal cavities with wall roughness. *J Aerosol Sci.* 2007;38(4):398-419.
80. Baehmann PL, Wittchen SL, Shephard MS, Grice KR, Yerry MA. Robust, geometrically based, automatic two-dimensional mesh generation. *Int J Numer Methods Eng.* 1987;24(6):1043-78.
81. Field DA. Laplacian smoothing and Delaunay triangulations. *Communications in applied numerical methods.* 1988;4(6):709-12.
82. Shewchuk JR. Engineering a 2D quality mesh generator and Delaunay triangulator., *Applied Computational Geometry: Towards Geometric Engineering.* . 1996.
83. Inthavong K, Tian L, Tu J. Lagrangian particle modelling of spherical nanoparticle dispersion and deposition in confined flows. *J Aerosol Sci.* 2016;96:56-68.

84. Shang Y, Tian L, Fan Y, Dong J, Inthavong K, Tu J. Effect of morphology on nanoparticle transport and deposition in human upper tracheobronchial airways. *The Journal of Computational Multiphase Flows*. 2018;10(2):83-96.
85. Sheehan MJ, Peters TM, Cena L, O'Shaughnessy PT, Gussman RA. Generation of nanoparticles with a nebulizer-cyclone system. *Aerosol Science and Technology*. 2009;43(11):1091-8.
86. Dailey LA, Schmehl T, Gessler T, Wittmar M, Grimminger F, Seeger W, et al. Nebulization of biodegradable nanoparticles: impact of nebulizer technology and nanoparticle characteristics on aerosol features. *J Controlled Release*. 2003;86(1):131-44.
87. Ohata S, Moteki N, Schwarz J, Fahey D, Kondo Y. Evaluation of a method to measure black carbon particles suspended in rainwater and snow samples. *Aerosol Science and Technology*. 2013;47(10):1073-82.
88. Xu Z, Kleinstreuer C. Direct nanodrug delivery for tumor targeting subject to shear-augmented diffusion in blood flow. *Med Biol Eng Comput*. 2018;56(11):1949-58.
89. Childress EM, Kleinstreuer C. Computationally efficient particle release map determination for direct tumor-targeting in a representative hepatic artery system. *J Biomech Eng*. 2014;136(1):011012.